DNA-TR-84-388

AN ANALYSIS OF ARMY THERMAL TRANSMISSIVITY CALCULATIONS

Kaman Sciences Corporation Systems Directorate
1911 Jefferson Davis Highway
Arlington, VA 22202-3508

1 November 1984

Technical Report

CONTRACT No. DNA 001-83-C-0232

THIS WORK WAS SPONSORED BY THE DEFENSE NUCLEAR AGENCY
UNDER RDT&E RMSS CODE B342083466 N99QAXAT00001 H2590D.

Prepared for
Director
DEFENSE NUCLEAR AGENCY
Washington, DC 20305-1000

Destroy this report when it is no longer needed. Do not return to sender.

PLEASE NOTIFY THE DEFENSE NUCLEAR AGENCY, ATTN: STTI, WASHINGTON, DC 20305-1000, IF YOUR ADDRESS IS INCORRECT, IF YOU WISH IT DELETED FROM THE DISTRIBUTION LIST, OR IF THE ADDRESSEE IS NO LONGER EMPLOYED BY YOUR ORGANIZATION.

DNA PRINTING PLANT

DISTRIBUTION LIST UPDATE

This mailer is provided to enable DNA to maintain current distribution lists for reports. We would appreciate your providing the requested information.

☐ Add the individual listed to your distribution list.

☐ Delete the cited organization/individual.

☐ Change of address.

NAME: _____

ORGANIZATION: _____

OLD ADDRESS	CURRENT ADDRESS
_____	_____
_____	_____
_____	_____

TELEPHONE NUMBER: ( ) _____

SUBJECT AREA(s) OF INTEREST:

_____	_____
_____	_____
_____	_____

DNA OR OTHER GOVERNMENT CONTRACT NUMBER: _____

CERTIFICATION OF NEED-TO-KNOW BY GOVERNMENT SPONSOR (if other than DNA):

SPONSORING ORGANIZATION: _____

CONTRACTING OFFICER OR REPRESENTATIVE: _____

SIGNATURE: _____

Director
Defense Nuclear Agency
ATTN: STTI
Washington, DC 20305-1000

Director
Defense Nuclear Agency
ATTN: STTI
Washington, DC 20305-1000

UNCLASSIFIED

SECURITY CLASSIFICATION OF THIS PAGE

AD-A176 959

REPORT DOCUMENTATION PAGE

Form Approved
OMB No. 0704-0188
Exp. Date: Jun 30, 1986

1a. REPORT SECURITY CLASSIFICATION UNCLASSIFIED	1b. RESTRICTIVE MARKINGS
2a. SECURITY CLASSIFICATION AUTHORITY N/A since Unclassified	3. DISTRIBUTION/AVAILABILITY OF REPORT Approved for public release; distribution is unlimited.
2b. DECLASSIFICATION/DOWNGRADING SCHEDULE N/A since Unclassified	
4. PERFORMING ORGANIZATION REPORT NUMBER(S) K-84-147U (R)	5. MONITORING ORGANIZATION REPORT NUMBER(S) DNA-TR-84-388
6a. NAME OF PERFORMING ORGANIZATION Kaman Sciences Corporation System Directorate 6b. OFFICE SYMBOL (If applicable)	7a. NAME OF MONITORING ORGANIZATION Director Defense Nuclear Agency
6c. ADDRESS (City, State, and ZIP Code) 1911 Jefferson Davis Highway Arlington, VA 22202-3508	7b. ADDRESS (City, State, and ZIP Code) Washington, DC 20305-1000
8a. NAME OF FUNDING/SPONSORING ORGANIZATION 8b. OFFICE SYMBOL (If applicable)	9. PROCUREMENT INSTRUMENT IDENTIFICATION NUMBER DNA 001-83-C-0232
8c. ADDRESS (City, State, and ZIP Code)	10. SOURCE OF FUNDING NUMBERS PROGRAM ELEMENT NO: 62715H; PROJECT NO: N99QAXA; TASK NO: T; WORK UNIT ACCESSION NO: DH007014

11. TITLE (Include Security Classification)

AN ANALYSIS OF ARMY THERMAL TRANSMISSIVITY CALCULATIONS

12. PERSONAL AUTHOR(S)

Keith, John R.; Portare, Anthony F.

13a. TYPE OF REPORT	13b. TIME COVERED	14. DATE OF REPORT (Year, Month, Day)	15. PAGE COUNT
Technical	FROM 830615 TO 841101	841101	150

16. SUPPLEMENTARY NOTATION

This work was sponsored by the Defense Nuclear Agency under RDT&E RMSS Code B342083466 N99QAXAT00001 H2590D.

17 COSATI CODES			18. SUBJECT TERMS (Continue on reverse if necessary and identify by block number)
FIELD	GROUP	SUB-GROUP	Thermal Radiation; TRAX Thermal Transmissivity, TAXV RECIPE
20	13		

19. ABSTRACT (Continue on reverse if necessary and identify by block number)

This report covers a review of the present procedures employed by the Army in calculating thermal transmissivity. As a result of the analysis it was determined that the present approach does not accurately predict the transmissivity. The report discusses a comparison between the present methodology and that employed in the revised DNA EM-1 handbook. A procedure is recommended which will correct existing deficiencies.

Keywords:

20. DISTRIBUTION/AVAILABILITY OF ABSTRACT	21. ABSTRACT SECURITY CLASSIFICATION
☐ UNCLASSIFIED/UNLIMITED ☒ SAME AS RPT ☐ DTIC USERS	UNCLASSIFIED
22a. NAME OF RESPONSIBLE INDIVIDUAL Betty L. Fox	22b. TELEPHONE (Include Area Code) (202) 325-7042
	22c. OFFICE SYMBOL DNA/STTI

DD FORM 1473, 84 MAR

83 APR edition may be used until exhausted
All other editions are obsolete

SECURITY CLASSIFICATION OF THIS PAGE
UNCLASSIFIED

CONVERSION TABLE

Base Units

Quantity	Unit	Symbol
Length	meter	m
Mass	kilogram	kg
Time	second	s

Derived Units

Quantity	Unit	Symbol	Formula
Force	Newton	N	$kg\ m/s^2$
Energy	joule	J	N m
Power	watt	W	J/s
Frequency	hertz	Hz	1 (cycle)/s

Conversion Factors

To convert from:	To:	Multiply by:
foot	meter(m)	0.3048
mile	kilometer(KM)	1.609
nanometer(nm)	meter(m)	10^{-9}
micrometer(m)	meter(m)	10^{-6}
kilometer(km)	meter(m)	10^{3}
calorie	joule(J)	4.187
ton(TNT equivalent)	joule(J)	4.2×10^{9}
density(lb/ft^3)	g/m^3	1.602×10^{3}
radiant exposure(cal/cm^2)	J/m^2	4.187×10^{4}

TABLE OF CONTENTS

Section		Page
	Conversion Table	iii
	List of Illustrations	v
	List of Tables	viii
1	INTRODUCTION	1
	1.1 Outline of Remaining Chapters	1
2	THE UK APPROACH	2
	2.1 The Riley Equation	2
	2.2 The Meteorological Data	5
	2.3 Geographical Variations	7
	2.4 Data Interpolation and Extrapolation	12
	2.5 Thermal Transmission Factors	22
	2.6 Critique of Riley's Equation	24
3	KSC THERMAL PREDICTION METHOD	26
	3.1 RECIPE Source Module	29
	3.2 KSC Monte Carlo Data Base	55
	3.3 Weather Analysis Requirements	66
	3.4 KSC Transmission Techniques	85
	3.5 KSC probabilistic Transmission Method	90
4	COMPARISONS OF KSC AND UK RESULTS	100
5	MONTE CARLO DATA BASE DEVELOPMENT	118
	5.1 QRT Data Base and Predictive Approach	118
	5.2 Limitations in The QRT Calculational Approach and Data Base	125
6	RECOMMENDED APPROACH FOR QRT DATA BASE REVISIONS	128
	6.1 Extension of the Wavelength Data Base	129
	6.2 Convert Scattered Flux Data Base to Buildup Factors	130
	6.3 Smoothing and Curve Fitting Buildup Factors	132
	6.4 Broad Band IR Absorption	134
7	LIST OF REFERENCES	135

LIST OF ILLUSTRATIONS

Figure		Page
1	MEASURED CLOUD BASE HEIGHT VISIBILITY AND MEAN VISIBILITY DISTRIBUTIONS, ANNUAL.....	13
2	VISIBILITY DISTRIBUTION - CLOUD BASE HEIGHT GROUP 1 - NW GERMANY - ANNUAL.....	16
3	VISIBILITY DISTRIBUTION - CLOUD BASE HEIGHT GROUP 2 - NW GERMANY - ANNUAL.....	17
4	VISIBILITY DISTRIBUTION - CLOUD BASE HEIGHT GROUP 3 - NW GERMANY - ANNUAL.....	18
5	VISIBILITY DISTRIBUTION - CLOUD BASE HEIGHT GROUP 1 - NW GERMANY - JANUARY.....	19
6	VISIBILITY DISTRIBUTION - CLOUD BASE HEIGHT GROUP 2 - NW GERMANY - JANUARY.....	20
7	VISIBILITY DISTRIBUTION - CLOUD BASE HEIGHT GROUP 3 - NW GERMANY - JANUARY.....	21
8	RANGE OF PROBABILITIES - ANNUAL.....	23
9	KSC CALCULATIONAL PROCEDURE.....	27
10	SURFACE BURST MODEL.....	34
11	INTERACTING AIR BURST MODEL.....	36
12	THERMAL YIELD FRACTION AS A FUNCTION OF BURST ALTITUDE AND YIELD.....	40
13	THERMAL YIELD FRACTION AS A FUNCTION OF BURST ALTITUDE AND YIELD.....	41
14	EFFECT OF ALTITUDE ON TOTAL THERMAL POWER, 100-KILOTON BURST.....	44
15	EFFECT OF ALTITUDE ON THERMAL POWER PULSE SHAPE, 100 KILOTONS.....	47
16	IRRADIANCE PREDICTED WITH THE STANDARD TIME FACTOR MESH FOR BURSTS AT 1 KFT ALTITUDE COALTITUDE AT THE 20 CAL/CM^2 EXPOSURE LEVEL.....	50
17	EFFECT OF ALTITUDE ON SPECTRAL DISTRIBUTION, 100 KILOTONS.....	51
18	SOURCE DISTRIBUTION FOR TRAX AND QRT CODES.....	52
19	SPECTRAL DISTRIBUTION RECEIVED A DISTANCE OF 21 KFT COALTITUDE FROM A 100 KT BURST.....	53
20	SPECTRAL DISTRIBUTION RECEIVED A DISTANCE OF 31 KFT COALTITUDE FROM A 1 MT BURST.....	54
21	COMPARISON OF TAX RESULTS WITH TRAX DATA NEVADA ATMOSPHERE WITH GROUND LEVEL AT 1.28 KM SOURCE 1 KM ABOVE GROUND. RECEIVER 3 M ABOVE GROUND....	63
22	COMPARISON OF BUILDUP FACTORS VS. THE SCATTERING OPTICAL DEPTH FOR VARIOUS WAVELENGTHS. PACIFIC ATMOSPHERE WITH BOTH SOURCE & SAMPLING AT 1 KM ALTITUDE.....	64

LIST OF ILLUSTRATIONS (Continued)

Figure		Page
23	COMPARISON OF BUILDUP FACTORS FOR SURFACE BURST..	65
24	COMPARISON OF BUILDUP FACTORS FOR SURFACE BURST..	67
25	COMPARISON OF BUILDUP FACTORS FOR SURFACE BURST..	68
26	COMPARISON OF RAYLEIGHT CROSS SECTION FOR TWO MODEL ATMOSPHERES.....	70
27	COMPARISON OF AEROSOL CROSS SECTION FOR TWO MODEL ATMOSPHERES.....	71
28	COMPARISON OF OZONE CROSS SECTION FOR TWO MODEL ATMOSPHERES.....	72
29	COMPARISON OF CARBON DIOXIDE DENSITY FOR THE TWO MODEL ATMOSPHERES.....	83
30	COMPARISON OF WATER VAPOR DENSITY FOR THE TWO MODEL ATMOSPHERES.....	84
31	COMPARISON OF SCATTERING BUILDUP FACTORS FOR VARIOUS WAVELENGTHS.....	88
32	KSC PROBABILISTIC TRANSMISSION METHOD.....	92
33	SAMPLE CASE. DATA IDENTIFIED BY WEATHER CONDITIONS.....	96
34	SAMPLE CASE. TRANSMISSION CURVES FOR WEATHER CONDITIONS.....	97
35	SAMPLE CASE. DATA IDENTIFIED BY CUMULATIVE OCCURRENCE PROBABILITY.....	98
36	SAMPLE CASE. TRANSMISSION CURVES FOR CUMULATIVE OCCURRENCE PROBABILITY.....	99
37	EFFECT OF YIELD ON TRANSMISSION PREDICTIONS.....	102
38	EFFECT OF SPECTRUM DIFFERENCES CAUSED BY SURFACE INTERACTIONS ON TRANSMISSION.....	103
39	EFFECT OF SOURCE ALTITUDE ON TRANSMISSION PREDICTIONS.....	105
40	EFFECT OF CLOUD CEILING ALTITUDE ON THE TRANSMISSION FOR ZERO GROUND ALBEDO.....	106
41	EFFECT OF CLOUD CEILING ALTITUDE ON THE TRANSMISSION FOR DIRT GROUND SURFACE.....	107
42	EFFECT OF GROUND ALBEDO ON THE TRANSMISSION.....	108
43	EFFECT OF BURST ALTITUDE ON TRANSMISSION WITH ALBEDO SURFACES.....	109
44	EFFECT OF SURFACE ALBEDO FOR 6.5 KM VISIBILITY...	110
45	COMPARISON OF KSC AND UK TRANSMISSION FACTORS....	112
46	COMPARISON OF KSC AND COOKE RESULTS 100 KT SURFACE BURST: 95% CASE.....	113
47	COMPARISON OF KSC AND COOKE RESULTS 100 KT SURFACE BURST: 50% CASE.....	115
48	COMPARISON OF KSC AND COOKE RESULTS 1 MT SURFACE BURST: 95% CASE.....	116

LIST OF ILLUSTRATIONS(Concluded)

Figure		Page
49	COMPARISON OF KSC AND COOKE RESULTS 1 MT SURFACE BURST: 50% CASE.....	117
50	DIRECT AND INTEGRATED SCATTERED INTENSITY VERSUS WAVELENGTH.....	124
51	PLOT OF BUILDUP FACTOR WITH SOURCE ALTITUDE .01 KFT.....	131
52	PLOT OF BUILDUP FACTORS WITH SOURCE ALTITUDE 2 KFT.....	133

LIST OF TABLES

Table		Page
1	DATA COLLECTION FORMAT FOR VISIBILITY/ CLOUD BASE HEIGHT DATA	6
2	DATA FORMAT FOR CHI-SQUARED TEST	8
3	ANNUAL STATISTICS (j-1)	10
4	ANNUAL STATISTICS (j-2)	10
5	RESULTS OF THE TESTS OF GEOGRAPHICAL ASSOCIATION	11
6	THERMAL PARTITION FOR NEAR-SURFACE BURSTS	42
7	TRAX BAND STRUCTURE	57
8	CARBON DIOXIDE ABSORPTION PARAMETERS	59
9	WATER VAPOR ABSORPTION PARAMETERS	60
10	SCATTERING PARAMETERS FOR THE SPRING-SUMMER MODEL ATMOSPHERE	73
11	SCATTERING PARAMETERS FOR THE FALL-WINTER MODEL ATMOSPHERE	74
12	WAVELENGTH DEPENDENT CROSS SECTION FACTORS	75
13	CARBON DIOXIDE ABSORPTION PARAMETERS FOR THE SPRING-SUMMER MODEL ATMOSPHERE	79
14	CARBON DIOXIDE ABSORPTION PARAMETERS FOR THE FALL-WINTER MODEL ATMOSPHERE	80
15	WATER VAPOR ABSORPTION PARAMETERS FOR THE SPRING-SUMMER MODEL ATMOSPHERE	81
16	WATER VAPOR ABSORPTION PARAMETERS FOR THE FALL-WINTER MODEL ATMOSPHERE	82
17	EQUIPROBABLE SETS OF METEOROLOGICAL DATA	94
18	TRANSMISSION VS. RANGE AND CASE COOKES WEATHER DATA KSC TRANSMISSION CLOUDS AT 3.0KM (GROUP III)	95
19	TRANSMISSION RUN PARAMETERS	101
20	QRT DATA BASE	119
21	QRT BAND STRUCTURE	127

SECTION 1

INTRODUCTION

Kaman Sciences Corporation (KSC), under contract to the Defense Nuclear Agency (DNA), has reviewed the methodology developed by United Kingdom (UK) Ministry of Defence and used by the U.S. Army for determining the thermal transmissivities in Northwest Europe for tactical nuclear weapons. Kaman then compared the UK methodology with the present KSC methodology which is being employed in the new EM-I (Capabilities of Nuclear Weapons) for Northwest Europe. Based on this comparison, Kaman Sciences Corporation recommended changing to a methodology which would update the present data base for determining the thermal transmissivities for tactical nuclear weapons employed in Northwest Europe.

1.1 OUTLINE OF REMAINING CHAPTERS.

Chapter 2 presents a discussion of the procedures employed by Maj. B.M. Cooke in generating thermal transmissivity data for the UK Ministry of Defence. The chapter includes a discussion of the basic transmission equation, the meteorological data, geographical data, and data interpolation and extrapolation used in the UK methodology. Chapter 3 offers a presentation of the KSC methodology employed for this effort. This section includes a description of the RECIPE code, the transmission data base, weather analysis requirements, transmission techniques, and probabilistic transmission employed by KSC. Chapter 4 presents a comparison of the results using the UK versus the KSC methodology. Chapter 5 describes the QRT data base. This section also discusses the limitations in the QRT calculational approach and data base. Chapter 6 offers a recommended approach for revisions in the QRT data base for use in the KSC methodology.

SECTION 2

THE UK APPROACH

The energy flux of thermal radiation from a nuclear fireball decreases rapidly with increasing distance from the burst. This is due not only to inverse-distance-squared geometric attenuation, but also to the absorption and scattering of the radiation during its passage through large distances in air. This latter effect is termed atmospheric transmission. In the wavelength region of interest, 0.3 to 4.0 μ, atmospheric transmission depends on such factors as the absorption of infrared radiation by water vapor and carbon dioxide, the absorption of ultraviolet and visible radiation by ozone, multiple scattering at all wavelengths from solid particles suspended in air and air molecules, reflections from the ground and clouds, etc. All of these factors vary with altitude and with prevailing weather conditions. Interactions such as scattering, which is produced by the reflection and refraction of light rays by certain atmospheric constituents such as dust, smoke, and fog, divert the rays from their original paths and result in diffuse, rather than direct transmission of the radiation. Therefore, a receiver with a large field of view (that is, most military targets) receives radiation that has been scattered toward it from many directions in addition to the directly transmitted radiation. Because the mechanisms of absorption and scattering depend on the wavelength, the atmospheric transmittance depends not only upon the atmospheric conditions, but also upon the spectral distribution of the radiation emitted by the fireball.

2.1 THE RILEY EQUATION.

The approach employed by the UK was based on an empirical equation for thermal transmission in the atmosphere developed by George Riley (Reference 1). In 1970, Maj. C.B. Pritchett

continued work originally started by B. Rankin on the prediction of thermal transmissivity factors for Northwest Europe, using meteorological data compiled over a period of some 10 years at airfields in Northwest Germany. Riley's formula was used to calculate transmissivity values which would not be exceeded at least 95, 50, and 5 percent of the time. Maj. Cooke (Reference 2) extended this work and offers the following rationale for the selection of this methodology.

"Several relationships are available for the prediction of thermal transmission factors from known visibility conditions. Eldridge (Reference 3) presented some of these, one of which was Riley's formula. Riley has derived functional relationships between thermal transmissivity and the distance between the source and the receiver for various meteorological conditions. This method was selected because:

a. It is applicable to the climate of Northwest Germany as it includes the effects of cloud cover.

b. The ranges (0.2 to 25 km) over which the relationship can be used are suitable for military applications.

c. The visibility range acceptable to the relationships (1.3 to 186 Km) is sufficiently wide to encompass the highest and lowest probabilities likely to be used.

d. They are derived for surfaces normal to the thermal fluence, which is assumed to be relevant to military operations."

Riley's relationship allows transmissivity to be predicted from cloud base height, visibility, and snow cover data. Unfortunately, Cooke was unable to obtain data which interrelates these three variables. It was only possible to obtain data

relating the frequency of cloud base height to visibility. Therefore, the effects of snow cover were ignored.

Riley at the Air Force Cambridge Research Laboratory has developed an empirical transmission prediction technique by representing the transmission of visible radiation as:

$$T = e^{-\beta D} + D^2(Ae^{-3.1D} + Be^{-1.12D} + Ce^{-\alpha D}) \qquad (1)$$

where T is the transmission over the path length D (km), β is an attenuation coefficient, and A, B, C and α are parameters depending on the meteorological conditions. The parameter values presented are based on data taken over path lengths from 0.2 to 25 km with values of βD between 0.02 and 40. The experimental data were obtained from References 5, 6, 7, 8, and 9. Riley suggested determining the value of β wherever possible by measuring the direct radiation. The alternative used by Cooke is:

$$\beta = 3.91/\nu \qquad (2)$$

where ν is the visual range defined as the range where the transmission decreases to 0.02. The correct terminology for ν is the meteorological range.

The values of the variables as applied by Maj. Cooke in equation 2.1 are:

$$A = 2\beta^{1/3},$$

$$B = \begin{cases} 1.29 & \text{- for an overcast sky less than 1500 meters cloud base height,} \\ 0.151 & \text{- clear sky,} \end{cases}$$

$$C = \begin{cases} 0.0102 & \text{- for an overcast sky below 300 meters cloud base height,} \\ 0.033 & \text{- for an overcast sky with a cloud base height between 300 and 1500 meters,} \\ 0.0033 & \text{- clear sky,} \end{cases}$$

$$\alpha = \begin{cases} 0.145\beta^{0.045} & \text{- clear sky,} \\ 0.22\beta^{0.12} & \text{- for an overcast sky,} \end{cases}$$

where an overcast sky has greater than five-eighths cloud cover.

This expression applies to horizontal paths near sea level and for a 2β detector aimed at the source.

The first terms in this expression represent the direct radiation while the other terms account for scattered and reflected radiation.

2.2 THE METEOROLOGICAL DATA.

Cooke was supplied visibility and cloud base height data taken at intervals of three hours over a period of approximately ten years at Gutersloh, Fassberg, Hannover, Hamburg, and Dusseldorf. Annual and monthly means were also provided and formed the basis of the UK analysis. Annual and monthly statistics were assembled which related the frequency of the three categories of cloud base height and thirteen categories of visibility. The three categories of cloud base heights are: Group 1, less than 300 meters; Group 2, 300 to 1,500 meters; and Group 3, above 1,500 meters. Cooke combined the case of no clouds into Group 3. The thirteen categories of visibility were selected ranges from 0 to 200 meters up to 8,000 to 16,000 meters as shown in Table 1. Tables were then drawn up of the number

Table 1. Data Collection Format for Visibility/Cloud Base Height Data.

METEOROLOGICAL DATA FOR DUSSELFORF (1950-59)
FASSBURG (1950-59), GUTERSLOH (1950-58)
HAMBURG (1949-58), HANNOVER (1949-59)

1. Data is listed by locations, each location being listed with annual means followed by monthly means.

2. Columns and rows are coded as follows:

Column Code Letter	A	B	C	D	E	F	G	H	I	J	K	L	M	N	O
Visibility (Meters)	200	200 - 400	400 - 600	600 - 800	800 - 1000	1000 - 1200	1200 - 1600	1600 - 2000	2000 - 2400	2400 - 3200	3200 - 4800	4800 - 8000	8000 - 16000	16000	Total

Row Code No	Cloud Base Height (Meters)
1	50
2	50-100
3	100-200
4	200-300
5	300-600
6	600-1000
7	1000-1500
8	1500-2000
9	2000-2500
10	2500
11	No 5/8+ layer
12	Totals

of occurrences of various weather conditions for the set of annual means and for each set of monthly means. From these, the cloud-base height/visibility distributions were derived.

2.3 GEOGRAPHICAL VARIATIONS.

It was not known how dependent the weather statistics were on the geographical variations of the recording stations. It would be simpler if a single set of statistics could be used to represent the cloud base/visibility relationships of all five locations. However, if there were significant differences between the weather statistics of the five locations, then reservations would need to be placed on the use of a single set of weather statistics to represent Northwest Germany.

A chi-squared value was used by Cooke as a measure of association for the data containing the variables location and visibility. The larger the chi-squared value, the greater is the independence, and conversely, the smaller the chi-squared value, the greater the degree of association.

In order to determine the number of occurrences of various weather conditions at the various geographical locations from the meteorological data over the period of ten years, tables were drawn up for each set of annual mean and monthly mean weather data and for each cloud base height group, as shown in Table 2.

Table 2. Data Format for Chi-Squared Test.

LOCATION CATEGORY "S"		VISIBILITY CATEGORY "d"			
Dusseldorf	1	n_{11ij}	n_{12ij}	n_{13ij}	n_{1dij}
Fossberg	2	n_{21ij}	n_{22ij}		n_{2dij}
Guterslok	3	n_{31ij}			n_{3dij}
Hamburg	4	n_{41ij}			n_{4dij}
Hannover	5	n_{51ij}			n_{5dij}

Where n_{Sdij} is the total number of occurrences of the given weather conditions over the ten year period, the suffixes have the following significance: "S" is the visibility category coded into groups 1 to 13, where 1 is the visibility of column A of the meteorological data (Table 1), i.e., less than 200 meters; 2 is the visibility of column B (200 to 400 meters), etc., up to 13, corresponding to column M of the weather data (8,000 to 16,000 meters).

"i" is the cloud base height group coded into the three categories:

1, less than 300 meters
2, between 300 and 1,500 meters, and
3, above 1,500 meters.

"j" refers to the particular set of weather data of which there are 13 groups:

1, the annual means
2, the means for January,
3, the means for February, etc., up to
13, the means for December.

Two specimen tables are reproduced. Table 3 gives the number of occurrences n_{Sdij} for the annual means and Table 4 gives the number of occurrences for the January means. For a table of "S" rows and "d" columns, the number of degrees of freedom for chi-squared is (S-1)(d-1). For each set of weather statistics, ij chi-squared is calculated. The results for the annual means and the January means are also shown in Tables 3 and 4. The complete set of chi-squared values for all the months is given in Table 5. For the means annual weather statistics, the chi-squared values show a high degree of association between the five locations. Because of this homogeneity, it is further assumed that the means statistics can represent the annual weather data for these five locations. Moreover, as the locations are widely spread, it is considered that one set of weather statistics can reasonably describe the annual weather conditions in Northwest Germany in areas which are similar to the geophysical conditions of those five locations, i.e., fairly low lying and flat.

For the analysis of the monthly statistics, for cloud base heights Groups 2 (between 300 and 1,500 meters) and 3 (above 1,500 meters), there was again a high degree of association for the five locations. For cloud base height Group 1 (less than 300 meters), there was, however, a diminution of the evidence for association, particularly for the months April to October. Indeed, the value of chi-squared for August indicates some positive degree of independence between the data provided by the various weather stations.

Table 3. Annual Statistics (j-1) Number of Occurrences n_{sdij}.

Period of Statistics	Cloud-Base Height Group	Location Category	Visibility Category d												Computed Chi-Squared Values X^2_{ij}	Degrees of Freedom D_{ij}
j	i	s	1	2	3	4	5	6	7	8	9	10	11	12	13	
1	1	1	2889	1460	1212	1244	1335	1460	2425	2393	1709	3954	4292	3480	1335	18.8	48
		2	2007	1157	1005	1054	1615	1414	3436	2995	1227	2466	4423	4084	2077		
		3	2334	1238	850	1192	1311	1484	3182	3038	2334	2770	3892	3158	2138		
		4	1694	1040	829	987	864	847	1905	2206	1411	4499	5011	4745	2770		
		5	1592	1487	797	771	897	949	2568	1823	1899	3696	4058	4622	3465		
1	2	1	11	23	46	81	93	198	417	654	604	2249	3848	6670	8675	9.0	48
		2	23	26	0	73	84	99	601	786	502	981	3021	5940	9674		
		3	0	20	32	29	175	166	677	1060	917	1423	3296	5563	9809		
		4	0	0	11	67	75	90	271	438	452	1759	2729	6180	9490		
		5	0	0	32	20	67	73	300	376	549	1539	2463	4678	10770		
1	3	1	61	73	75	105	143	222	482	593	540	2203	4082	7009	8368	9.0	48
		2	143	108	111	108	172	169	607	683	365	639	2168	4794	9540		
		3	49	78	67	116	172	195	587	835	797	1323	2585	4736	10428		
		4	67	67	81	125	137	169	344	639	455	1671	2606	5212	7997		
		5	84	105	70	96	175	128	452	441	467	1396	2463	4710	9636		

Table 4. January Statistics (j-2) Number of Occurrences n_{sdij}.

Period of Statistics	Cloud-Base Height Group	Location Category	Visibility Category d												Computed Chi-Squared Values X^2_{ij}	Degrees of Freedom D_{ij}
j	i	s	1	2	3	4	5	6	7	8	9	10	11	12	13	
2	1	1	180	175	117	110	134	159	319	218	131	292	287	180	122	31.5	48
		2	112	91	94	118	154	127	298	337	103	228	303	276	151		
		3	181	129	121	157	109	133	282	274	222	234	295	173	113		
		4	125	112	55	133	64	91	156	208	125	420	404	370	153		
		5	52	127	79	88	74	84	236	175	189	368	354	326	250		
2	2	1	3	6	3	19	16	22	62	95	80	230	412	617	637	43.7	48
		2	6	6	0	0	0	6	19	132	74	103	362	735	776		
		3	0	0	0	0	6	18	76	140	76	147	374	547	843		
		4	0	0	0	14	3	14	25	29	66	234	332	659	746		
		5	0	0	0	0	2	5	41	47	74	179	245	461	999		
2	3	1	5	7	13	13	24	22	61	70	87	248	876	656	608	13.9	48
		2	15	0	5	15	12	10	68	68	68	102	286	551	728		
		3	4	2	0	11	11	22	54	112	107	220	287	460	919		
		4	6	10	4	28	39	35	48	85	74	238	256	495	683		
		5	4	2	6	13	19	13	51	38	83	199	311	473	792		

Table 5. Results of the Tests of Geographical Association.

Period (j)	Cloud-Base Height Group (i)	Chi-Squared Value	Number of Degrees of Freedom	Serial
Annual	1	18.8	48	1
	2	9.0		2
	3	9.0		3
January	1	31.5	48	4
	2	23.7		5
	3	13.9		6
February	1	34.6	48	7
	2	19.0		8
	3	20.5		9
March	1	40.2	48	10
	2	23.0		11
	3	17.0		12
April	1	75.4	48	13
	2	26.4		14
	3	16.9		15
May	1	58.8	48	16
	2	17.2		17
	3	13.7		18
June	1	77.7	48	19
	2	10.3		20
	3	11.6		21
July	1	54.3	48	22
	2	13.0		23
	3	14.8		24
August	1	87.0	48	25
	2	10.7		26
	3	13.0		27
September	1	57.6	48	28
	2	19.4		29
	3	17.2		30
October	1	58.0	48	31
	2	21.5		32
	3	19.5		33
November	1	29.0	48	34
	2	24.1		35
	3	19.4		36
December	1	35.8	48	37
	2	26.3		38
	3	20.6		39

NOTES:

1. The values of chi-squared for the mean annual statistics are all within the 99.5% level.
2. The values of chi-squared for the monthly statistics for cloud-base height Groups 2 & 3 are all within the 99% level.
3. The values of chi-squared for the months April to October for cloud-base height Group 1 were not significant at the 75% level.
4. The value of chi-squared for the month of August for cloud-base height Group 1 was not significant at the 0.5% level.

Some nil reports occurred in a number of the monthly weather statistics. Further tests were conducted to investigate the possibility of these causing errors in the statistical analysis of association. The weather data were rearranged into a different set of visibility categories to eliminate nil reports and the chi-squared values were recomputed. The results obtained by Cooke did not differ appreciably from the original results present previously.

2.4 DATA INTERPOLATION AND EXTRAPOLATION.

The monthly and annual weather data available to describe cloud base height and visibility were far from complete. In Figure 2.1 the known mean annual distributions of the three cloud base heights chosen and the overall mean are shown. It can be seen that little long range visibility data were available for cloud base heights Groups 2 and 3. This information was needed to predict the various probability levels of transmissivity.

The annual visibility curves in Figure 1 appear to be of cumulative Gaussian form. For each curve there is suggested a relationship of the standardized form

$$P = \frac{1}{2\pi} \int_{-\infty}^{(X - \mu_{ij}) / \sigma_{ij}} \exp(-\tfrac{1}{2}t^2)\,dt \qquad (3)$$

where P = cumulative occurrence,
X = visibility measured on a logarithmic scale,
μ_{ij} = mean visibility measured on a logarithmic scale,
σ_{ij} = standard deviation,

and, as before,

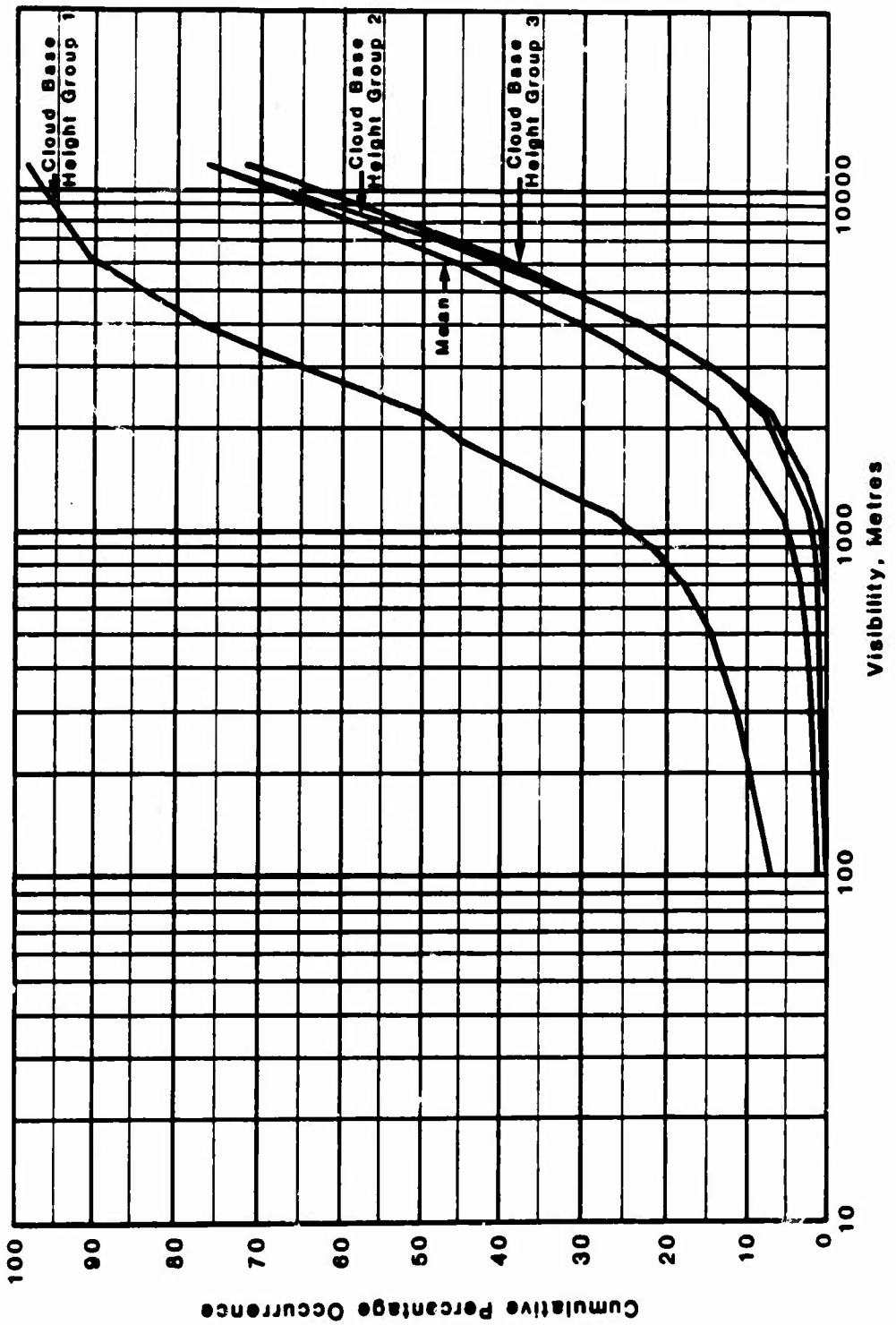

Figure 1. Measured Cloud Base Height Visibility and Mean Visibility Distributions, Annual

i = 1 for cloud base height Group 1, etc.,

j = 1 for the annual mean weather data,

j = 2 for January mean weather data, etc.

The cumulative Gaussian curve would normally be expected to operate from 0 to 100 percent of recorded data. However, it can be seen from Figure 1 that cloud base height Group 1 appears to flatten out at around 7 percent. Furthermore, an analysis of all the annual and monthly statistics showed that the minimum probability levels for cloud base Group 1 tailed off between 5 and 2) percent, and for cloud base Group 2 and 3, between 0 and 2 percent.

It was assumed by Cooke that this early flattening out is produced by factors which solely affect the low visibility levels. One such factor for the cloud base height Group 1 could arise when the cloud base height reaches ground level. For the higher cloud base height Groups 2 and 3, industrial haze may introduce factors affecting low visibility readings. Moreover, the general practice of recording the worst visibility in any direction is likely to increase the incidence of recorded low visibility readings and it suggests that there is a marked probability of these being nil visibility. In such circumstances, it becomes unrealistic to establish a Gaussian fit from 0 to 100 percent incidence of visibility reading and the above equation is rewritten to establish a model of the form

$$\frac{P-M_{ij}}{1-M_{ij}} = \frac{1}{2\pi} \int_{-\infty}^{(X-\mu_{ij})/\sigma_{ij}} \exp(-\tfrac{1}{2}t^2)\,dt \qquad (4)$$

where M_{ij} = optimum probability level of recorded visibilities.

By using probit analysis, the equation can be further re-written

$$Y = G_{ij} X + A_{ij}. \tag{5}$$

where Y is the probit corresponding to $\frac{P-M_{ij}}{1-M_{ij}}$

with $G_{ij} = 1/\sigma_{ij}$ and, in order to avoid the necessary computing with negative numbers, the customary step is taken

$$A_{ij} = K - \frac{\mu_{ij}}{\sigma_{ij}} \tag{6}$$

where K = 5.

Computer programs where used to obtain the values of G_{ij} and A_{ij} for the annual and monthly cloud base height/visibility distributions.

(1) An iterative method was used to obtain the maximum likelihood estimates for the parameters A_{ij} and G_{ij} in equation (2.5) for each set of statistics.

(2) The iteration was repeated with $M_{ij} = M_{ij} \pm \delta M$ until there is the maximum agreement between observed data and data predicted by equation (4). A chi-squared test was used as an indicator for the goodness of fit of the cumulative Gaussian curve model.

Samples of the pictorial comparisons between predicted and observed data for annual and monthly cloud base height/visibility distributions are given in Figures 2 to 7 for the annual data (for all three cloud base height groups). A reasonable level of agreement between the cumulative Gaussian models and the observed data was indicated by the chi-squared tests.

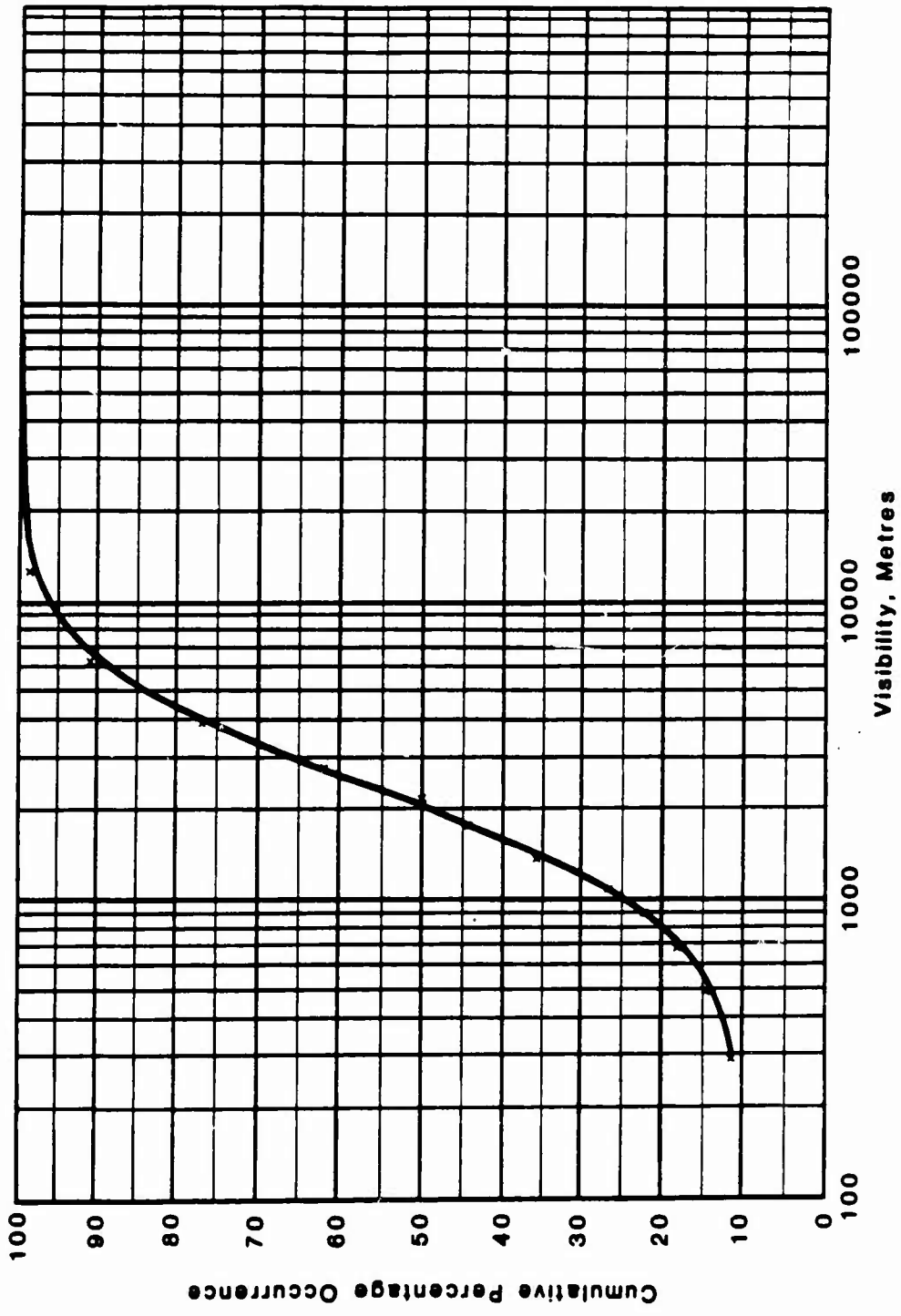

Figure 2. Visibility Distribution - Cloud Base Height Group 1.

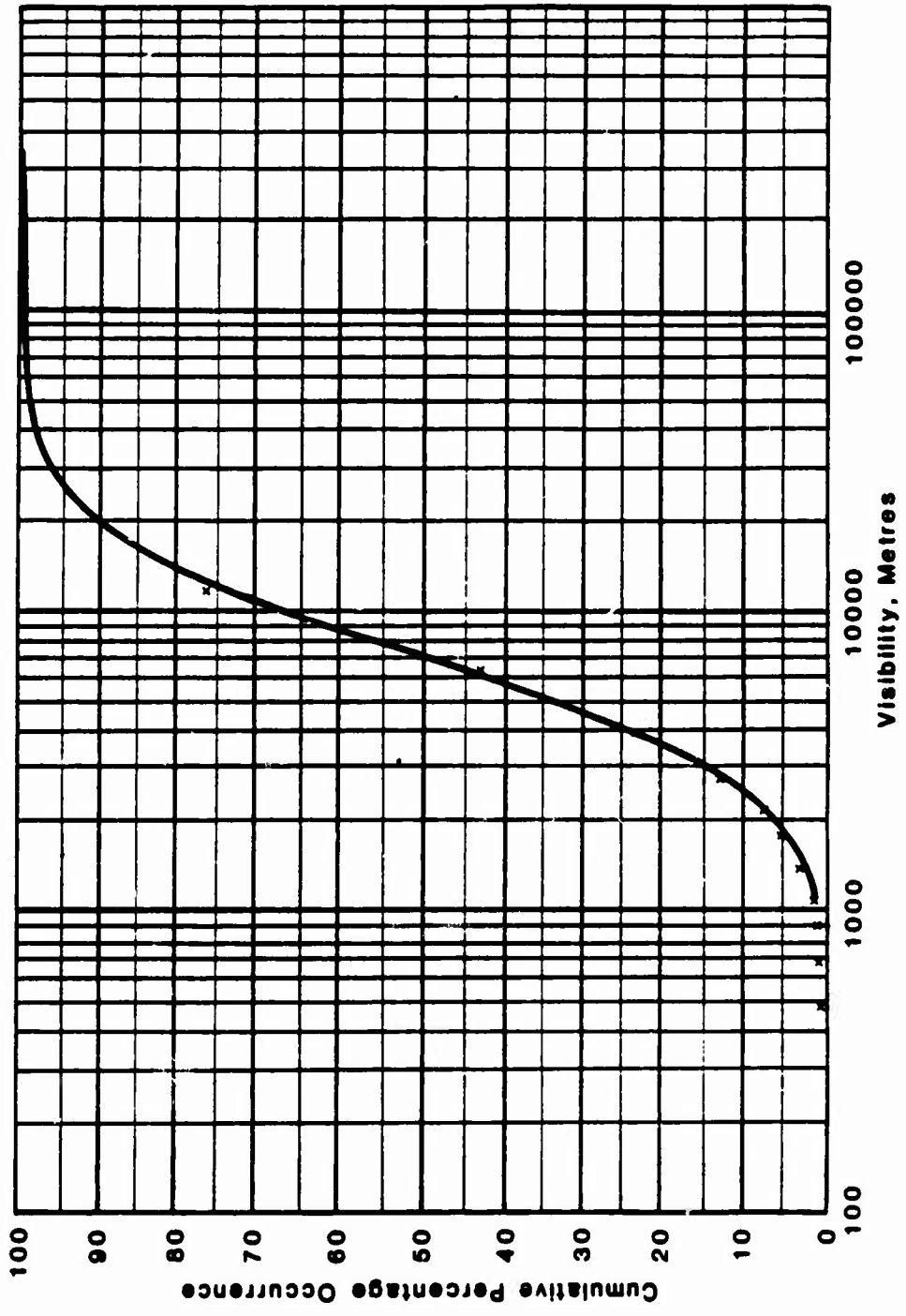

Figure 3. Visibility Distribution - Cloud Base Height Group 2 - NW Germany - Annual.

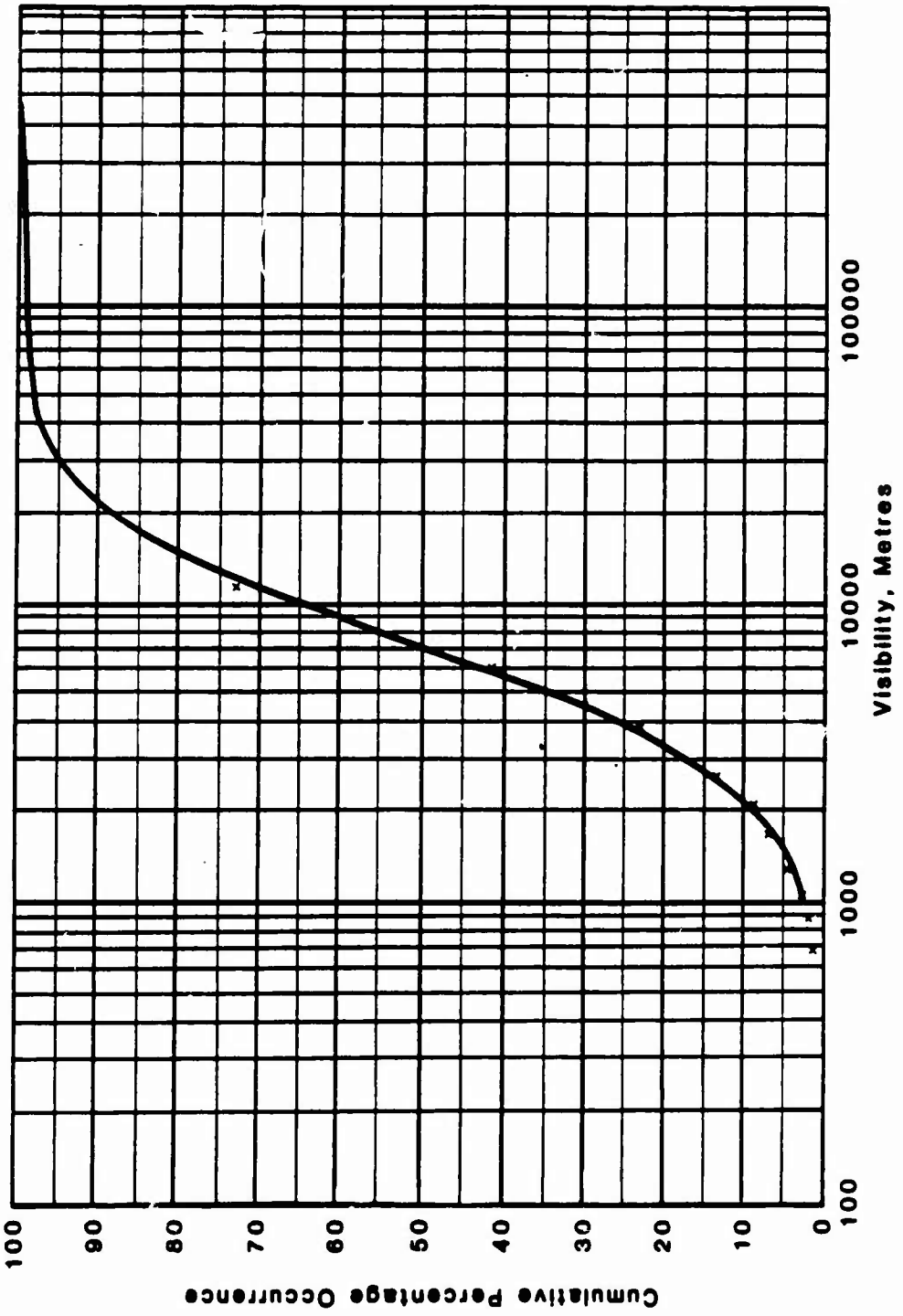

Figure 4. Visibility Distribution - Cloud Base Height Group 3 - NW Germany - Annual.

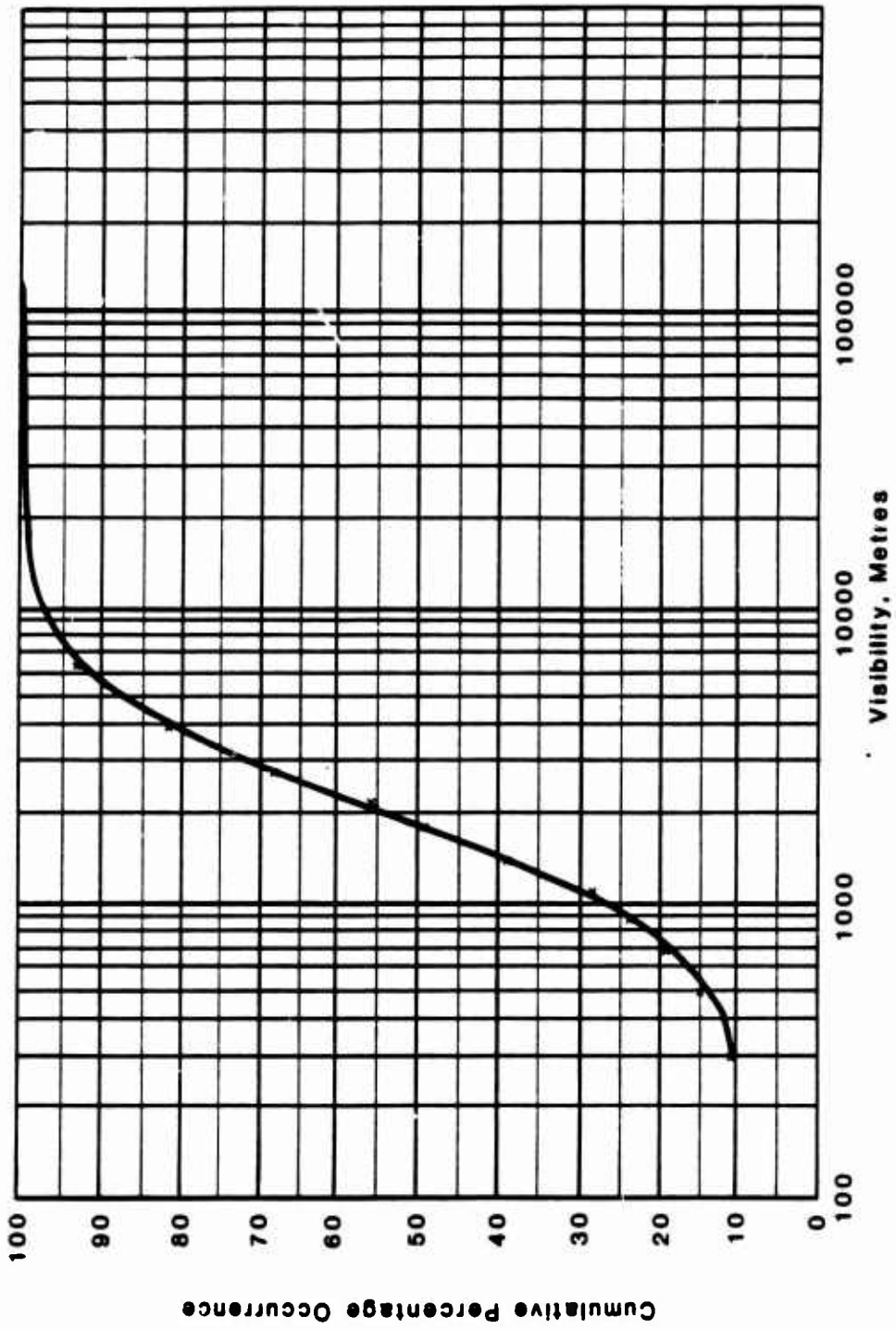

Figure 5. Visibility Distribution - Cloud Base Height Group 1 - NW Germany - January.

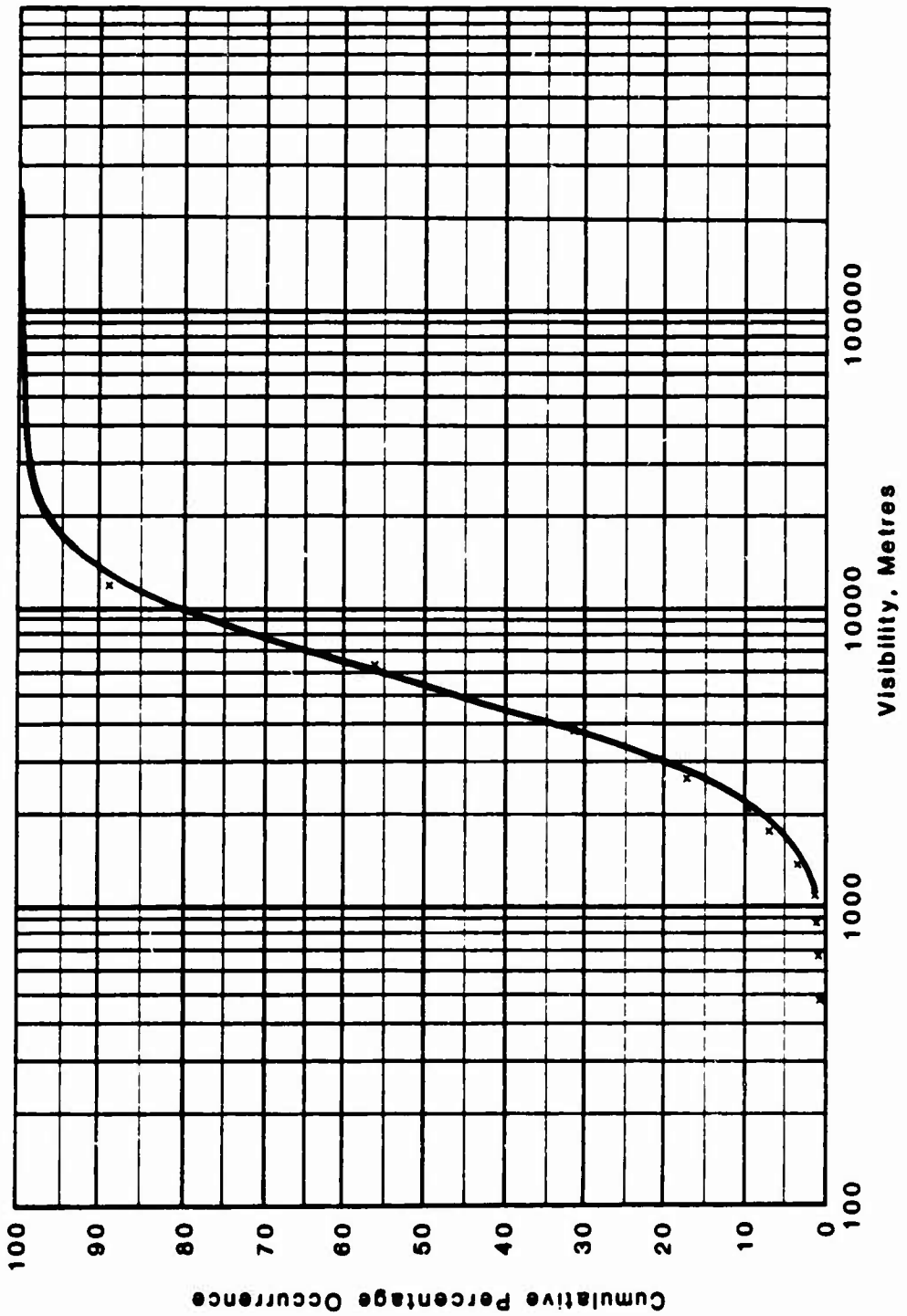

Figure 6. Visibility Distribution - Cloud Base Height Group 2 - NW Germany - January.

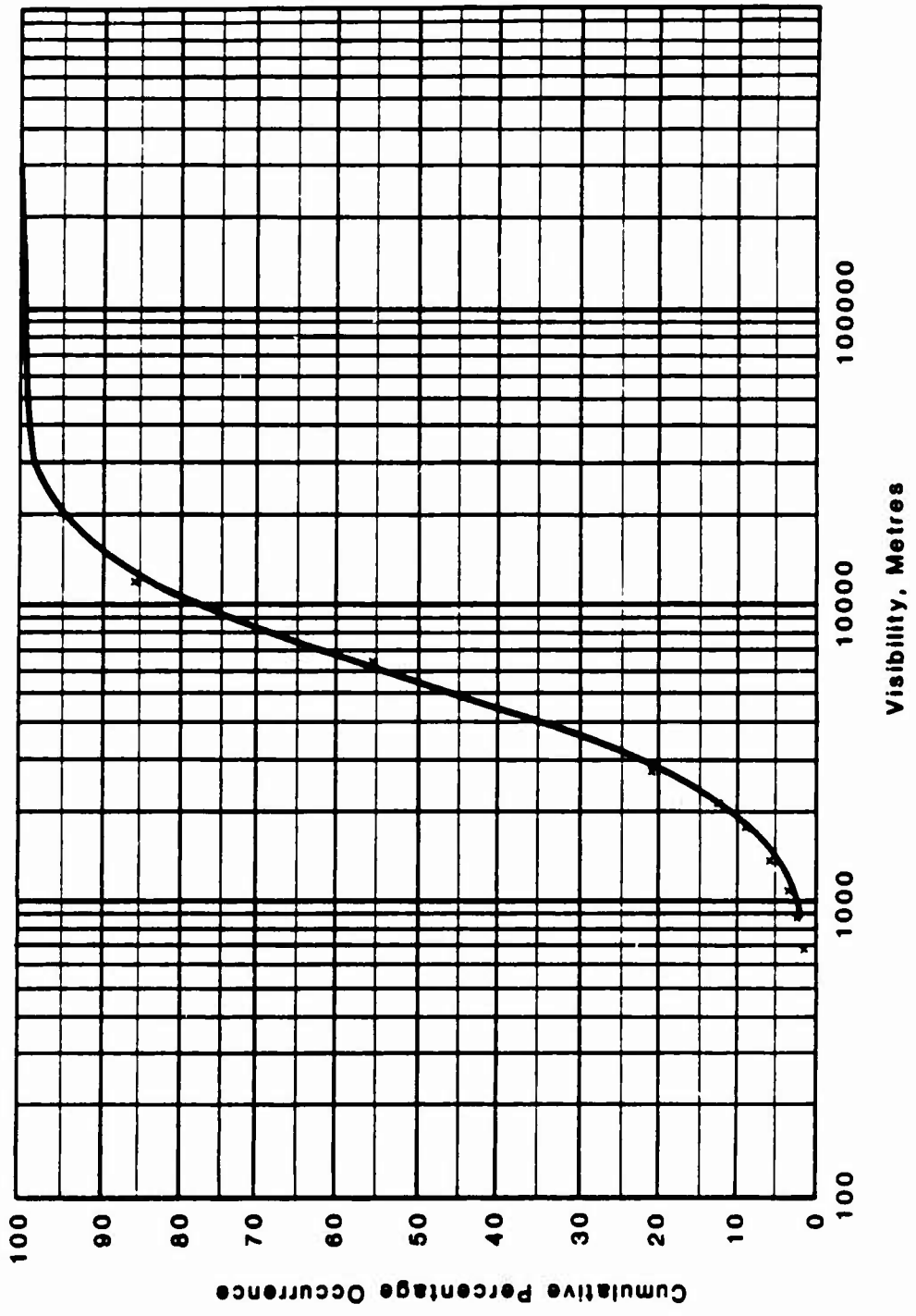

Figure 7. Visibility Distribution - Cloud Base Height Group 3 - NW Germany - January.

2.5 THERMAL TRANSMISSION FACTORS.

From each Gaussian model of the annual and monthly weather statistics, an entire range of weather data was predicted and applied to Riley's equation to obtain thermal transmissivities.

Thermal transmission factors were computed over a range of 0.25 to 23.75 km at 0.5 km intervals for various probability levels, and they are presented in graphical form as a relationship between transmission factors and distance from source for a series of probabilities. The mean annual transmission factors are given in Figure 8. Similar figures were computed for each of the monthly mean weather statistics.

The relationship with the lowest transmissivities represents the 5 percent (i.e., on 5 percent of occasions these will be the transmissivity described or less). The next highest relationship is 10 percent case and additional relationships are given in steps of 10 percent up to 90 percent case. They are completed at the 95 percent case (i.e., when there is a 95 percent probability that the given transmission factor will not be exceeded).

At present, thermal calculations for military equipment survivability and effects tables use the 95, 50, and 5 percent transmissivity levels. Comparing the mean monthly with the mean annual transmissivities for the three probabilities will show some seasonal variations. These seasonal variations are sufficiently small (10 percent) to be ignored in the 95 percent probability case, but the maximum variation of +75 percent for the 5 percent case may be sufficiently high for there to be a need to recognize seasonal variations in certain circumstances. However, in both equipment survivability and effects tables studies, for the poor transmissivity, it is the worst case that

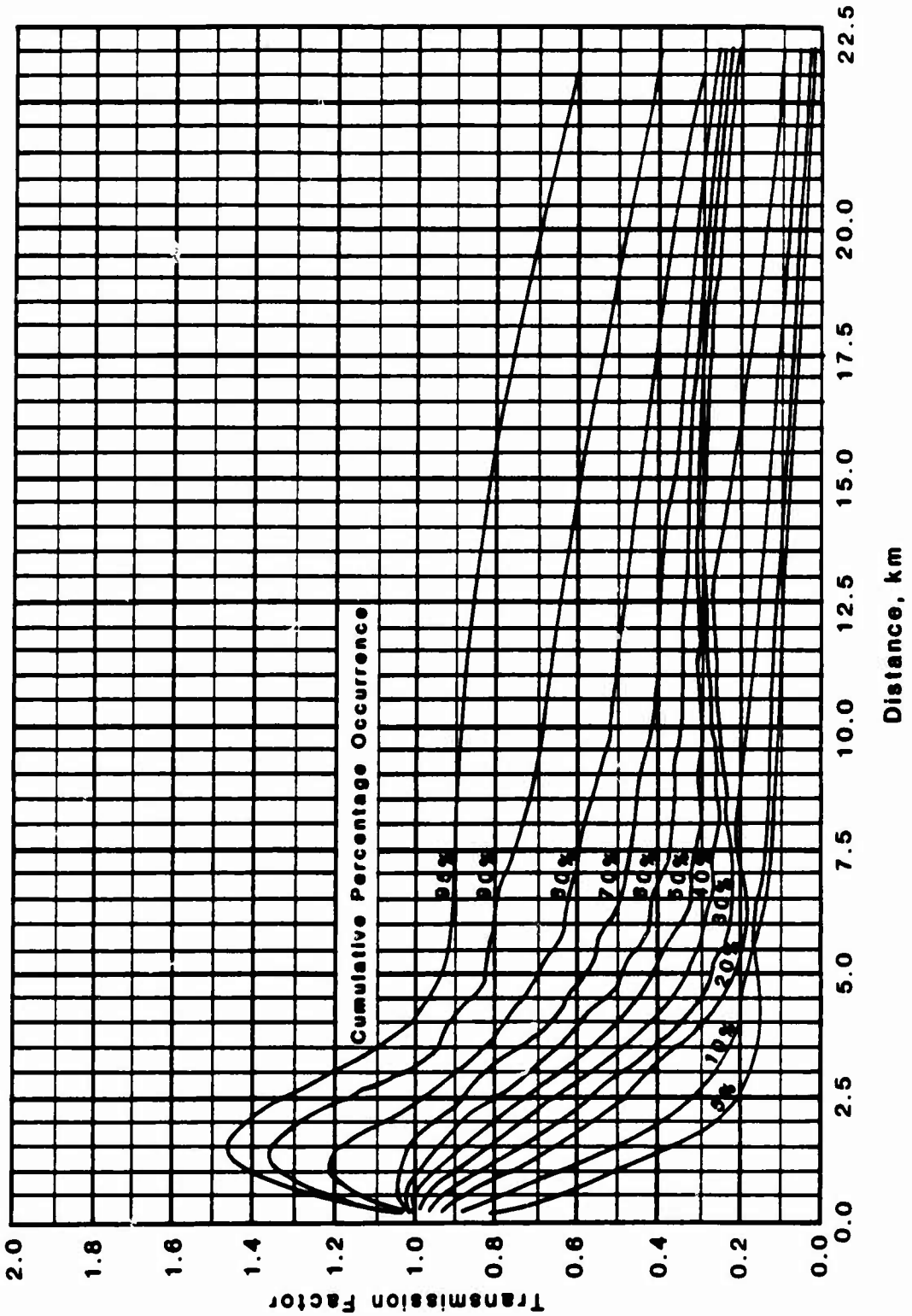

Figure 8. Range of Probabilities - Annual

is of interest. Here the variation is only 20 percent, which was viewed as insignificant when the low transmission factor (0.2) was considered.

2.6 CRITIQUE OF RILEY'S EQUATION.

In the analysis performed by Kaman Sciences Corporation, several concerns were raised on the use of the Riley equation for calculation of the thermal transmissivity.

The Riley equation is an empirical fit and as such is crude compared to presently available techniques. The relation is based in part on a series of experiments using a tungsten lamp. Therefore, the equation can not be affected by changes in the source spectrum which would result from the use of different yield weapons. In addition, Riley used a standard surface and does not account for various terrain features (e.g., desert, forest, or urban area) which may apply in different tactical scenarios. The relationship is valid for visible light and does not account for radiation outside the visible spectrum. The path radiation travels according to Riley's equation is assumed to be horizontal at sea level with a constant air density. This ignores the effect of varying air density as radiation travels from the fireball to the target at some other altitude, which could be of significance for both land and air targets. The relationship does not adequately model multiple scattering contributions.

There also exists some uncertainty in the definition in the visibility as defined by Riley and employed by Cooke. Riley defines visual range applicable to his relationship as the range at which the direct beam transmission is 2 percent. However, this was not the definition employed by the meteorological stations which used an "eyeball" method. Cooke estimated that

visibility, commonly observed by the "eyeball" method, is about one-half of the visual range. Cooke used an estimate of the relationship between visual range and visibility that required all visibility predictions be doubled before applying them to Riley's equation. This practice was selected because at worst, it errs on the side of safety in any thermal calculation. From an aspect of troop safety, this method would provide for more thermal energy at the receiver location due to an increase in visual range, thereby providing less attenuation by the atmosphere. However, it does introduce some uncertainty into the equation.

SECTION 3

KSC THERMAL PREDICTION METHOD

The KSC Thermal Prediction Method to generate the probabilistic exposure predictions is summarized in Figure 9. A crucial element is the prediction of the nuclear source output which is accomplished by the RECIPE code. The thermal radiation from a nuclear burst was not explicitly discussed in the UK documents. The RECIPE code was not modified on this contract, but is discussed for completeness in the following subsections. The main calculational chain is shown in the center of the chart and included: (1) a weather analysis for the particular area of interest; (2) identification of pertinent meteorological parameters to describe the broad range of weather conditions of interest primarily involving the visibility and albedo surface specifications; (3) computation of transmission prediction curves for these parameters; and (4) converting the results to transmission occurrence probabilities. These are then combined with the RECIPE source to obtain the probabilistic exposure predictions. An important ingredient in the TAXV predictions is a very large data base of build up factors generated by the KSC TRAX Monte Carlo Code. This data base is generated for a wide range of meteorological conditions and can be used for many diverse applications. If exposure predictions are desired for a specific set of weather conditions then the probabilistic routines are bypassed as shown. The irradiance at a receiver is given by:

$$H = \frac{q}{4\pi R^2 \lambda} \sum T(\lambda, H_s, H_r, R) * P(\lambda, t, H_s) * E_A(\lambda, H_s, H_r, R) \quad (7)$$

where

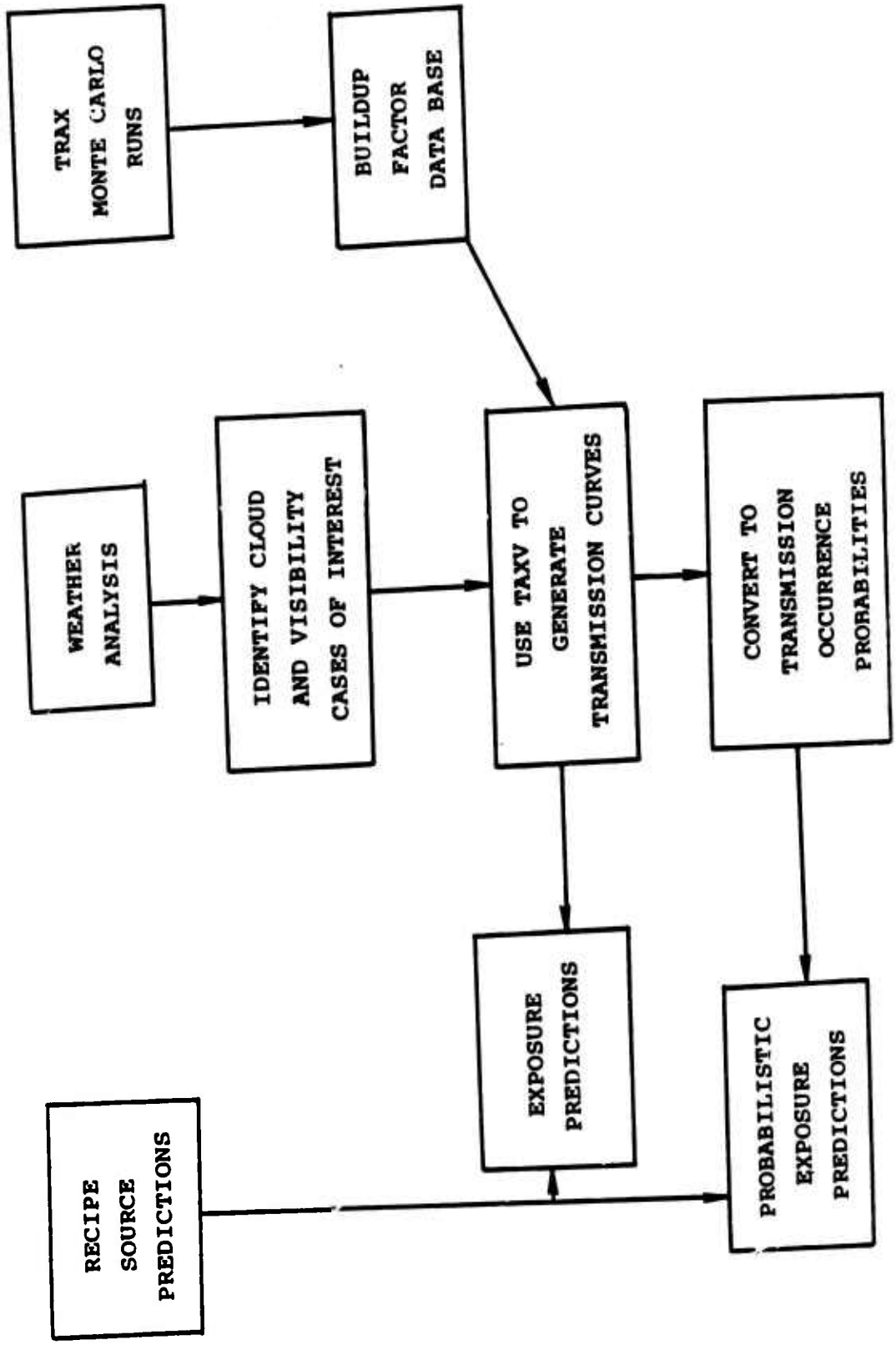

Figure 9. KSC Calculational Procedure.

P is the spectral power discussed in Section 3.1.1

T is the transmission factor discussed in Section 3.4

λ is the wavelength

H_s is the source altitude

H_r is the receiver altitude

R is the slant range

t is the time

E_A is the albedo surface enhancement factor

and g is a geometry factor

The exposure is obtained by integrating this expression over time in the TAXV code.

The transmission is given by the product of the direct transmission (T_D) and a scattering buildup factor (B_s).

$$T(\lambda, H_s, H_r, R) = T_D(\lambda, H_s, H_r, R) * B_s(\lambda, H_s, H_r, \tau_s) \quad (8)$$

where all the variables have been defined except for τ_s which is the scattering optical depth found by integrating the scattering cross section along the sight path from source to receiver. Implicit in these expressions is a model atmosphere containing a particular definition of atmospheric parameters as a function of altitude including the surface visibility, and water vapor, and albedo surface definition.

The geometry factor and the power are computed in the RECIPE module. The build-up factor and the albedo enhancement factor form the Monte Carlo data base and are computed by the TRAX Code. The other required factors and computations are contained in the TAXV modules. In the following sections the variation of the computational scheme are described in detail.

3.1 RECIPE SOURCE MODULE.

Only a minor effort on this contract involved the RECIPE code but for completeness the code will be briefly described since it forms a crucial element in our calculational scheme and will be used in future thermal predictions. The code was originally developed by SAI (References 9 and 10) over a period of many years. Reference 11 utilizes this code as the basis for the fireball output specifications. The code has undergone considerable revision and simplification at KSC (References 12 and 13) while retaining the full capability of predicting the detailed source output for a very wide range of burst yields and altitudes including surface interaction effects. The material given here is extracted primarily from the KSC portion of Reference 13 and is included here because the balance of Reference 13 will be of no interest to users of this document.

3.1.1 RECIPE Code Description.

RECIPE is a fast running Fortran computer code that calculates the power output of nuclear fireballs as a function of time and wavelength. The original version contained atmospheric transmission and instrumentation routines which were used to analyze the nuclear test data. The unclassified version of RECIPE was used for these studies. A classified version exists which accurately predicts the details of the first pulse signature for use in nuclear detection diagnostic purposes. The details of the first pulse are not important for typical damage response analyses since essentially all of the energy is contained in the second thermal pulse. For detailed analyses of the response of personnel to flashblindness or retinal burns and for evaluation of goggles or photochromic protective devices, a more detailed model of the first pulse might be necessary.

The original version developed the power at 56 wavelengths between 200 and 12500 nm. The grid of 56 wavelengths was chosen to give detailed representation of the atmospheric transmission and the response of the instrumentation used on the nuclear tests. The source module of RECIPE actually uses only 26 wavelengths to describe the spectral output of the fireball. To save running time without sacrificing any output details, the spectral grid of the retained routines was reduced to the basic 26 groups.

The input parameters required by the source routines of RECIPE and their intervals of validity are:

Yield	1.E-4 to 3.E4	(kt)
Altitude	<30	(km)
Bomb Mass	<2.E6	(lb/kt)

The power output is given as a function of:

Time	1.E-6 to 30*T2MAX	(sec)
Wavelength	200 to 12500	(nm)
Elevation Angle	-90 to 90	(degrees)

The evaluation angle dependence arises only for those cases involving surface interactions where the fireball is nonspherical. T2MAX is used throughout this section to refer to the time of the peak of the main or second thermal pulse.

The RECIPE source module contains a free air burst model, a surface burst model, an interacting burst model, and a high altitude burst model. These models parallel the historical development of the code. A short description of these models will be given including the routines that are used in each model. Additional details are contained in References 9 and 10.

3.1.1.1 Free Air Burst Model.

The basic data used in the free air burst model are based upon a set of four detailed theoretical radiation-hydrodynamic code calculations run with the RHGEN code at yields of 4, 14, 110, and 6600 kt. The first three correspond to three U.S. nuclear atmospheric bursts which have been measured and analyzed in great detail. The RHGEN code contains the latest air opacity data, a realistic debris mixing model and an improved technique for shock front location which is necessary to provide good definition of the early time pulse characteristics. The debris mixing model was found to be necessary to provide good comparisons with measured second maxima times and powers.

The mixing of the bomb debris in the fireball results in changes in the radiative properties of the fireball, but affects the thermodynamic properties very little. The increased opacity due to the debris contribution seems to slow the radial heat flow near the time of minimum, increases the pressure in the fireball, causing a continued expansion with a resulting delay in the time of second maximum. The increased opacity causes an increase in the effective fireball radius, a decrease in the effective temperature, and a lower power.

Two different procedures are used in the RECIPE model to represent the RHGEN results. Prior to the time of breakaway, which corresponds to the time at which the shock becomes transparent, the spectral power of the fireball is calculated by combining the geometrical properties of the shock with the spectral brightness of the shock. The time of breakaway is about one-third that of minimum so that a very small amount of energy is released prior to this time. The details of the handling of this portion of the output are of little significance in response calculations especially at low altitudes.

After the time of breakaway the radius and brightness temperature are different for each wavelength. The RECIPE code uses a curve-fitting procedure to reproduce the spectral power curves of RHGEN. The eight parameters needed are the time of breakaway, time of minimum, time of second maximum, ten times the time of second maximum and the spectral powers at these times. These parameters are used in the code to generate the spectral power at an arbitrary time.

The routines used in the free air burst model are:

SPFLUX: principal routine which calculates the spectral power at the fireball surface at a given time utilizing the following subroutines.

FRONT: provides shock front properties as a function of yield, burst altitude, and bomb mass.

RHSF: provides the spectral brightness of the shock front as a function of the shock velocity and altitude.

PARLOW: provides parameters for low altitude bursts for utilization by the formulas in SPFLUX.

For many USANCA applications the burst is low enough that significant interaction of the fireball with the ground surface occurs resulting in a significant change in the radiating characteristics of the fireball. These effects have been incorporated into surface interaction modules which have been thoroughly check with available atmospheric test data (Reference 10).

3.1.1.2 Surface Burst Model.

The surface burst model is based to a large extent on analysis of nuclear test results because of the difficulty in representing the experimental results entirely from theoretical results (Reference 10). For times through minimum the fireball development is the same as that for a free air burst but with a different effective yield. The parameters needed to obtain the spectral power at the later times were determined from experimental data.

3.1.1.3 Interacting Burst Model.

Photographic data were used extensively to model the fireball development that occurs when surface interactions occur. The fireball at early times does not touch the ground but during the growth phase does intersect the ground. Two different regimes are suggested: The interaction occurs early enough that a transition to a surface burst occurs, and an interaction occurs late enough that the fireball shape is perturbed but remains above the ground.

3.1.1.4 Surface Burst Transition.

If the fireball contacts the surface prior to shock formation, the low altitude air burst is transformed into a surface burst. The spectral power computed in the code always refers to that radiated from a sphere. For the surface burst an effective yield factor of 1.96 is used and a shape factor (SAF) is applied to represent the dependence of the fluence on the elevation angle to the receiver.

Figure 10 shows how this is modeled as a function of time. In the top illustration for the air burst at altitude H(O) the ratio (WFAC) of the effective yield (W) to the device yield (WKT)

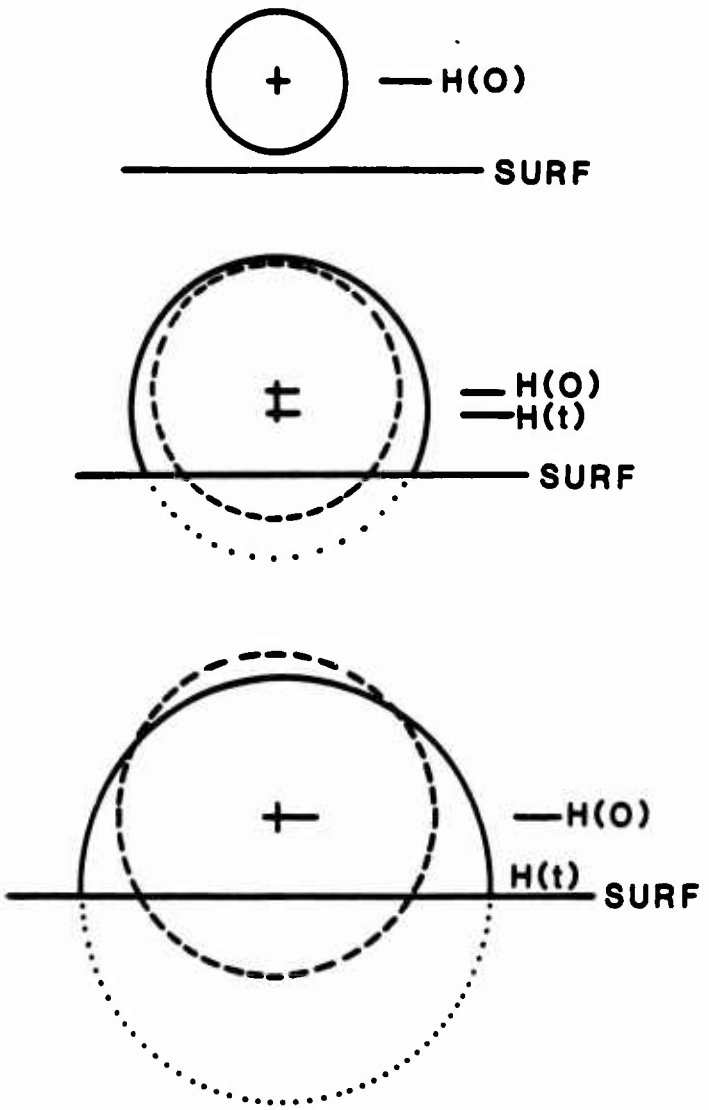

Figure 10. Surface Burst Model.

is equal to one at the early times. WFAC is computed in the following manner for the transition positions as represented by the middle illustration. If the surface were not there, the fireball would develop as shown by the dashed lines. Represent the volume above the surface by V_a and the volume below the surface by V_b. If the assumption is made that a fraction R of the volume below the surface is returned to the above ground perturbed fireball V_a', that the centers of the volumes are the same, and that the effective yield is proportional to the total volume, then

$$V_a' = V_a + R*V_b \tag{9}$$

$$WFAC = V'/V = V_a'/V_a = 1 - R + R/f \tag{10}$$

where $$f = V_a/(V_a + V_b) \tag{11}$$

is the fractional volume above the surface.

The model reduces the effective burst altitude linearly in time so that the burst altitude is zero at twice the time of first contact causing the sphere to transform smoothly into a hemisphere. The assumed value of R is .96 and, therefore, the limiting value for WFAC is 1.96.

3.1.1.5 Interacting Air Burst.

For this case, contact with the surface is made after shock wave formation, and the assumption is that negligible energy is transmitted to the surface. Figure 11 illustrates the model used when the contact occurs prior to the time of breakaway as indicated by photographic analysis. The truncated sphere is defined in terms of the parameter b given by the expression:

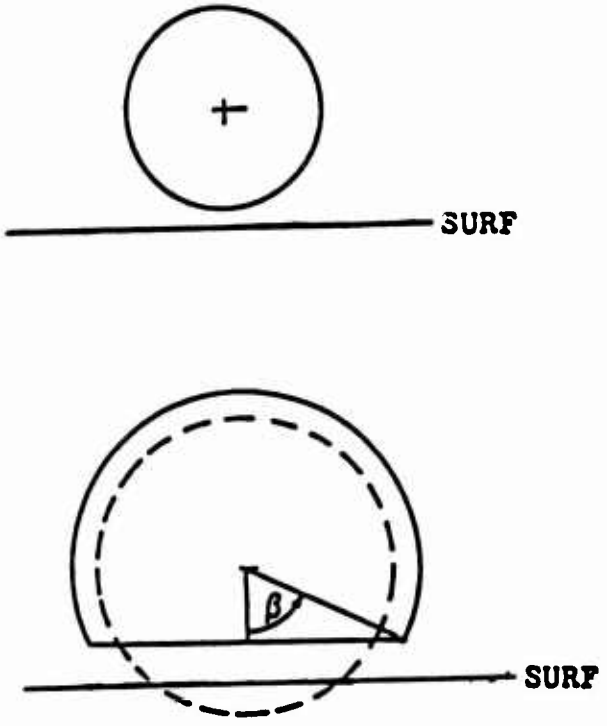

Figure 11. Interfacing Air Burst Model.

$$b(t) = 1.24\ (1 - \exp(-g)) \qquad \text{(radians)} \qquad (12)$$

where

$$g = 0.4\ (t/t_e)^{**2.4} \qquad (13)$$

t = time

t_e = time of contact

The maximum value of b allowed is 71 degrees. The volume of the truncated sphere is equated to the underformed sphere.

The algorithm for the case where the shock contacts the ground after breakaway is similar to the above except that the fireball radius and shock front radius are taken into account independently. The altitude of the reflected shock is computed, and the time of contact for use in the above formulas is taken as the time at which the reflected shock reaches the bottom of the fireball. A detailed discussion of these factors is contained in Reference 10. Since the fireballs are not in general spherical the shape factor depends upon the elevation angle between the fireball symmetry axis and the receiver.

The routines used to describe the interacting bursts are:

WEFF: main routine in the interacting burst model. Sets interaction times. Provides transition in properties.

SHAPE: provides shock radius, glowing radius, and shock temperature.

DARKR: accounts for dirt plume for surface sources

3.1.1.6 High Altitude Model.

The low altitude models were extended by altitude scaling techniques valid to altitudes of 30 km. The data for the altitude scaling of the shock properties needed for times less than breakaway were obtained from FIREBALL runs.

After breakaway the same type of parametric fits used in the free air model are used with altitude scaling using the ratio $D = 1.22E-3/\rho$ where ρ is the ambient density at a selected altitude. The power level for each wavelength is given by

$$P_w = P_o \exp(-\tau) \qquad (14)$$

where P_w is the power level at time of minimum with NO_2 absorption, P_o is the same quantity without NO_2 absorption, and τ represents the effective optical thickness of the NO_2 for a given yield.

Values of P_w and P_o are available at sea level (SL) and thus define τ. At a selected altitude the τ are given by

$$\tau(D) = \tau(SL)/D^{**}1.26 \qquad (15)$$

at each wavelength.

To summarize, the set of RECIPE routines when accessed at a certain time with a particular yield, altitude and bomb mass return the fireball output power for each of the 26 wavelengths at the time desired. The basic calculations give the output for a spherical fireball, and a shape factor is applied to obtain the power in a particular receiver direction when that information is supplied. The shape of the fireball is computed at each time, and any modifying factors are computed at each time step. For

incorporation into TAXV the possibility of a rising fireball was included in the routines, so that the shape factors computed by the code includes this effect which was neglected in the original RECIPE code.

Figure 12 shows the thermal fraction as a function of yield with the burst altitude as a parameter. This represents the fraction of the total device yield that has been radiated from the fireball up to 10*T2MAX.

A general downward trend is noted with increasing yield. The basis for these data are from rad-hydro runs at 4, 14, 110, and 6600 kt yields with the yields' dependence being determined by the interpolation scheme used in the code.

Figure 13 shows the same information plotted as function of burst altitude with the yield as a parameter. These curves do not include the reduction due to surface interaction effects. In Table 6 the thermal fractions for surface and free air bursts are shown along with the transition height. Note that for the higher yields the reduction in the partition for the surface burst is about a factor of two. For the lower yields the reduction in partition is much larger.

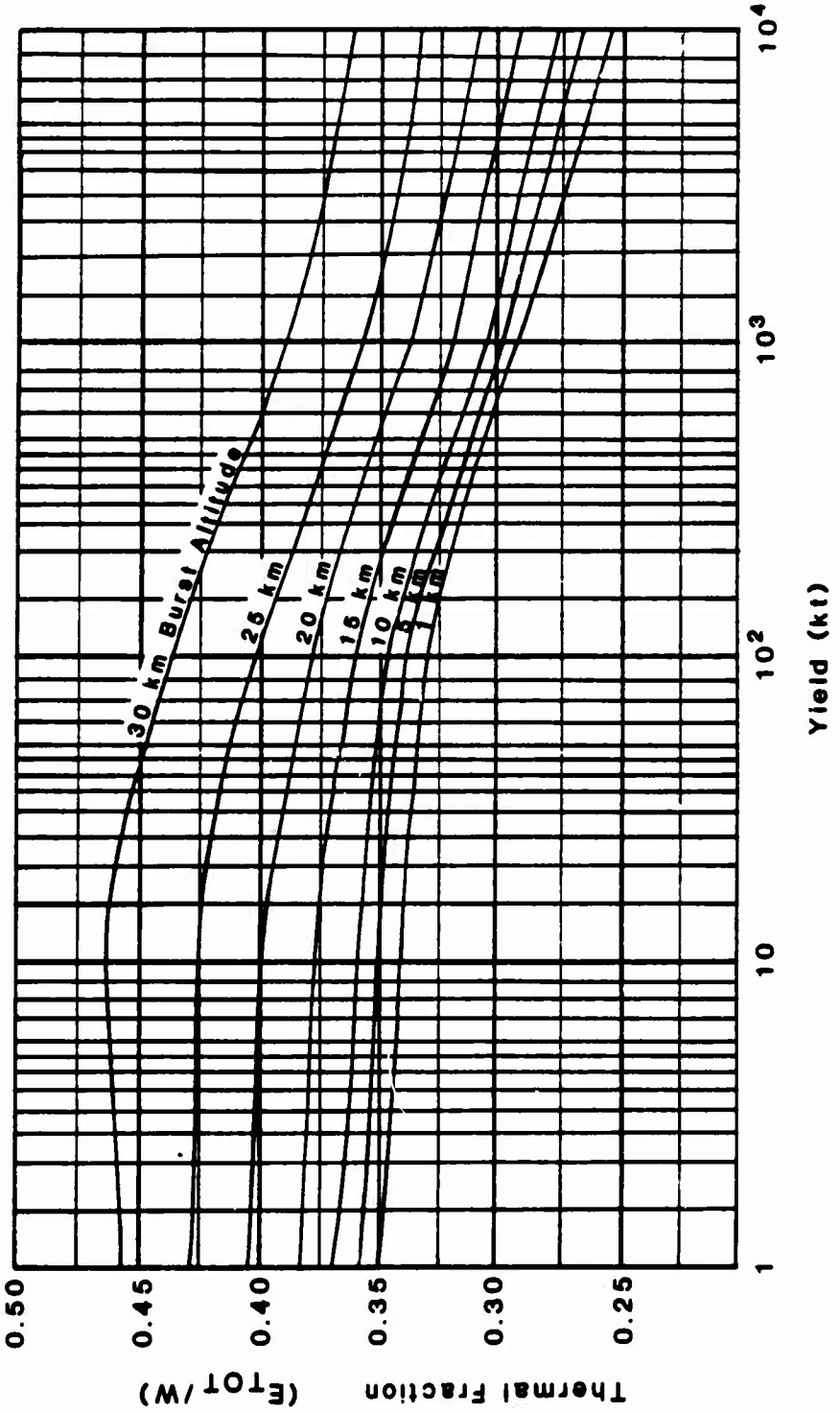

Figure 12. Thermal Yield Fraction as a Function of Burst Altitude and Yield (Yield Contours)
(Source: Hillendahl, 1980; EM-1 Date: February 1982)

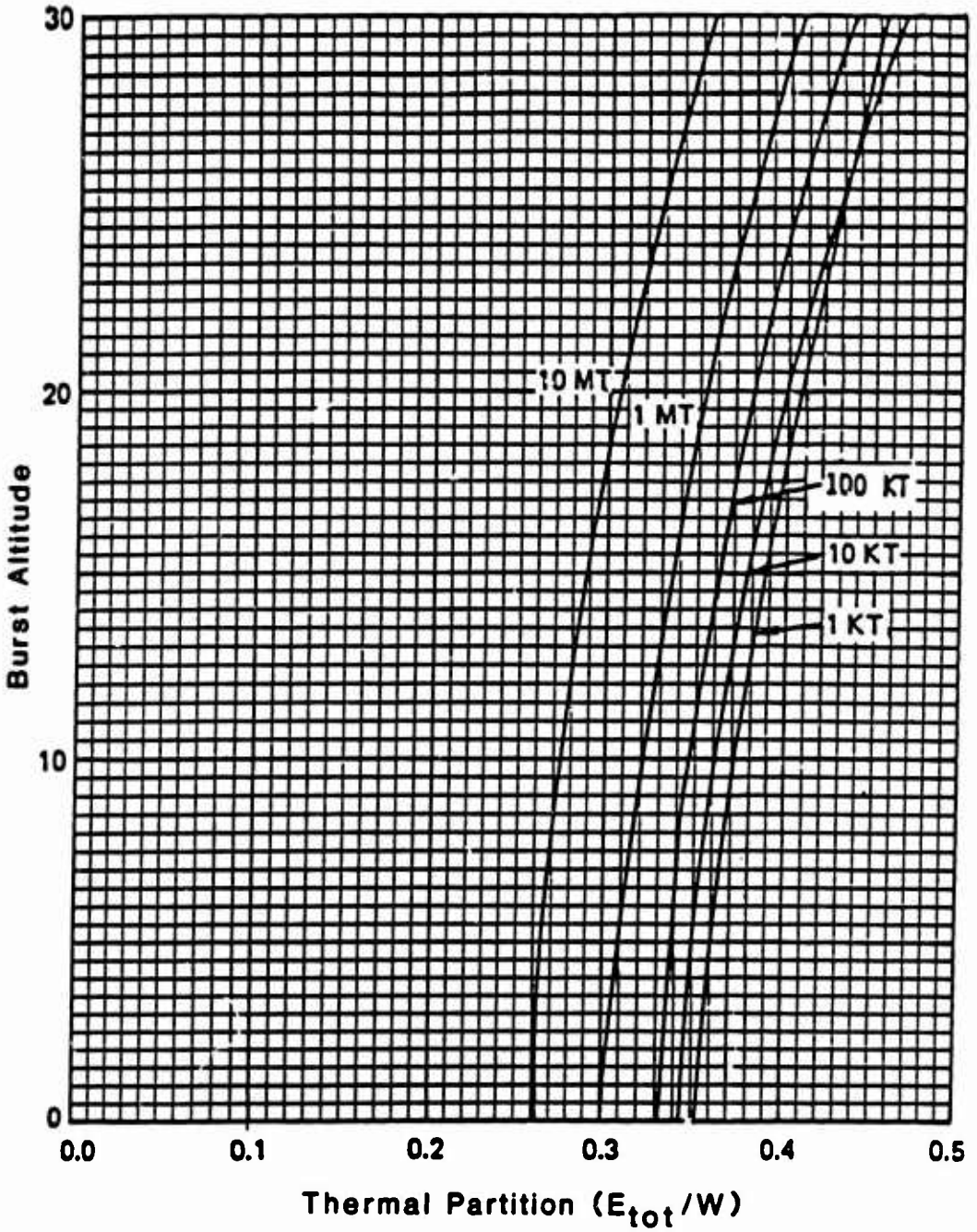

Figure 13. Thermal Yield Fraction as a Function of Burst Altitude and Yield (Altitude Contours)
(Source: Hillendahl, 1980: EM-1 Date: February 1982)

Table 6. Thermal Partition for Near-Surface Bursts.

Yield (KT)	Surface Burst Partition (Fraction)	Non-Surface Burst Partition (Fraction)	Transition Height (Meters)
1	0.045	0.350	4
10	0.066	0.341	8.6
100	0.13	0.330	18.5
1000	0.16	0.291	40
10000	0.17	0.254	86

The difference noted for the surface and non-surface bursts have major implications in predictions of the exposure from low altitude bursts especially for receivers near the ground surface. For lower yield tactical devices the thermal output of a surface burst is 1/3 that of a low altitude free air burst for a 100 kt yield. For a 1 kt yield the ratio is about 1/8. A shape factor must also be considered since the fireballs for the interacting bursts are strongly perturbed and are hemispherical in shape. Examples of the magnitude of these effects on the exposure predictions will be considered in the following sections.

3.1.2 Time Dependent Power.

Previous USANCA thermal prediction methods have ignored time dependent effects. For many applications and certainly for any detailed response calculations the time dependence of the thermal environment is very important. For eye damage effects and especially for evaluation of eye protective devices, the time dependence of the radiant level is very important. The RECIPE

code gives the time dependent fireball power output in detail including a general representation of the first pulse as discussed previously, a classified version is available giving the first pulse in detail.

The basic output of the SPFLUX routine is the spectral power FOLZ(H) (w/eV) as a function of photon energy at the time of interest. The shape factor (SAF) is then applied to obtain the power emitted in a particular receiver direction

$$FOLZH(h\nu) = FOLZ(h\nu) * SAF. \tag{16}$$

Two alternate time dependent modes are available. In one mode a time mesh is defined and the above spectral power is stored for each of the time steps for use in the predictive routines of TAXV. More detail about this mode will be given later. In the other mode, the calculation above is completed for each single time step defined by the TAXV control routine of interest.

The power is then obtained as a function of time by summation over the energy intervals

$$P(t) = \sum_{h\nu} FOLZH(h\nu) * \Delta h\nu \ . \tag{17}$$

As will be discussed in the following section the spectral power is actually converted to a wavelength dependence prior to regrouping into the wavelength mesh used in the transmission routines and further processed into the standard TAXV wavelength grid. In Figure 14 are shown the powertime curves for 100 kt burst for various source altitudes. As discussed previously the unclassified version of RECIPE has been used in this development so the first pulse represents only the continuum contribution from the heated shock. The details of the NO_2 absorption and its

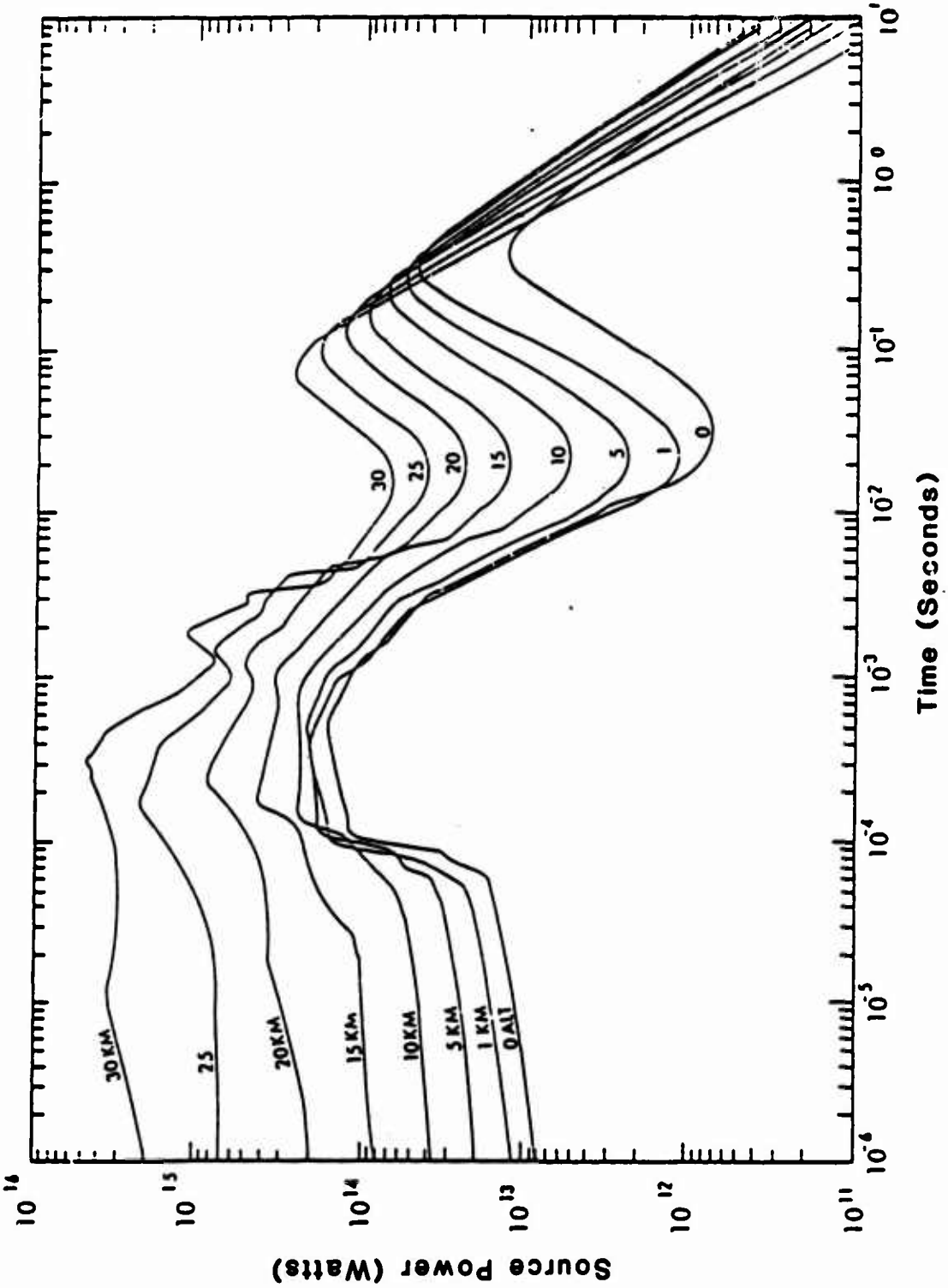

Figure 14. Effect of Altitude on Total Thermal Power, 100-Kiloton Burst.

effect on the early time signature are not included. This is not important for material response considerations since only a very small fraction of the energy is contained in the early pulse.

These curves show the expected trends with altitude. The power level of the first pulse increases with increasing altitude, the minimum is shallower as the altitude is increased, and the second pulse becomes narrower and higher as the altitude increases. Note, the relatively large difference between the free air burst at 1 km and the surface burst. The surface burst has a much smaller second thermal power maximum and a somewhat longer time to second maximum, T2MAX. The first pulse for the two cases is seen to be very similar. These curves represent the power leaving the fireball surface. In order to compute the irradiance at a receiver it is necessary to weight the FOLZS by the atmospheric transmission and the spectral dependent response function before summing over the wavelength bands. This will be discussed in later sections.

This option of computing the response involves accessing the RECIPE routines at each of the times required in the TAXV control routines which can become a relatively time consuming process. Another option mentioned earlier involves generating the matrix FOLZH ($h\nu$,t) for the 26 energy mesh points and a predetermined time grid. The total exposure is then found by integrating over the time grid.

The time mesh is determined in the following manner. A total of 95 time factors are defined with 60 factors increasing in increments from .05 to 3., then with 35 factors increasing in increments of .2 from 3.2 to 10. The actual times are then found by multiplying the time factors by the time of second maximum. In this manner fine time steps are defined from zero to 3 times

the time of second maximum where the power is a rapidly varying function of time. The log-log scales in Figure 14 do not give a good feel for the actual time dependence of the power curves for the second pulse. In Figure 15 the power-time curves in Figure 14 are replotted on normalized linear scales. The abscissa is the ratio of the time to T2MAX. The second thermal pulse when plotted in this normalized manner is seen to display a relatively small altitude dependence. The increase in the minimum power at higher altitudes is shown, and the relative unimportance of the first pulse in terms of total power is shown.

In Figure 16 the irradiance is shown for bursts at an altitude of 1 kft. The receiver is at an altitude of 1 kft and at a range of 31 kft for the 1Mt and at 21 kft for the 100 kt. The total exposure for both cases is 20 cal/cm^2. The data points are the times at which TAXV computes the power time mesh and are seen to represent the shape of the curves in fine detail.

The code does not contain an explicit formula for the total power integrated over the spectrum at T2MAX nor for T2MAX itself. Instead curve fits are used in the code for each of the 26 energy grid points. The expression is of the form:

$$T2MAX(h\nu) = 3.682E\text{-}2 * (W^{**}C(h\nu)) * (\rho/\rho_o)^{**}.315 \qquad (18)$$

where the parameter C is a function of $h\nu$, and the altitude dependence is given by the density ratio expression. The above formula is used if bomb mass is less than 2.5E3 lb/kt. For heavier bombs, a factor involving bomb mass is included which increases T2MAX. In the routines developed for this program T2MAX for the total integrated power is represented by T2MAX for 550 nm since the spectrum tends to be peaked in the visible portion of the spectrum.

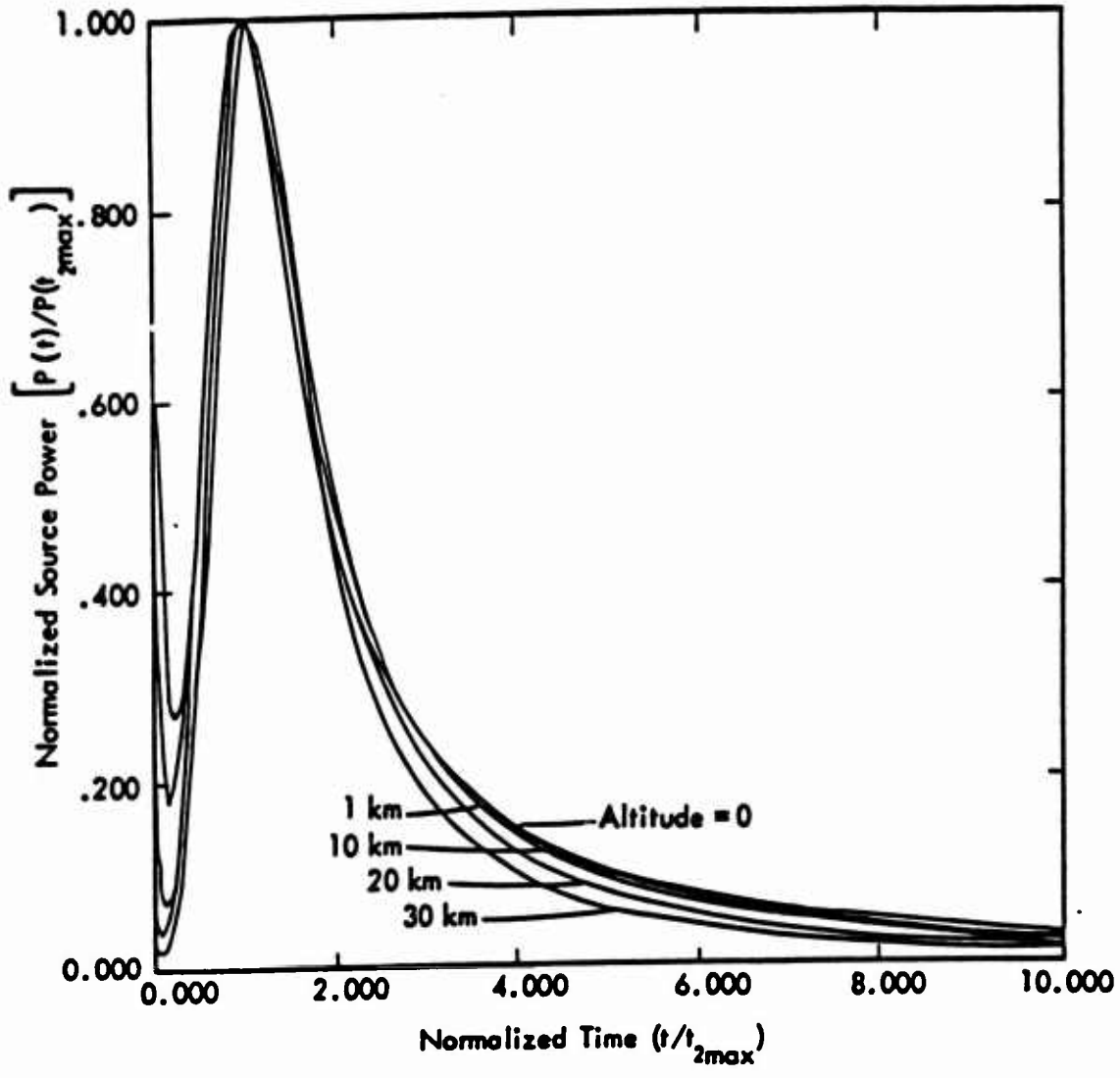

Figure 15. Effect of Altitude on Thermal Power Pulse Shape, 100 Kilotons.

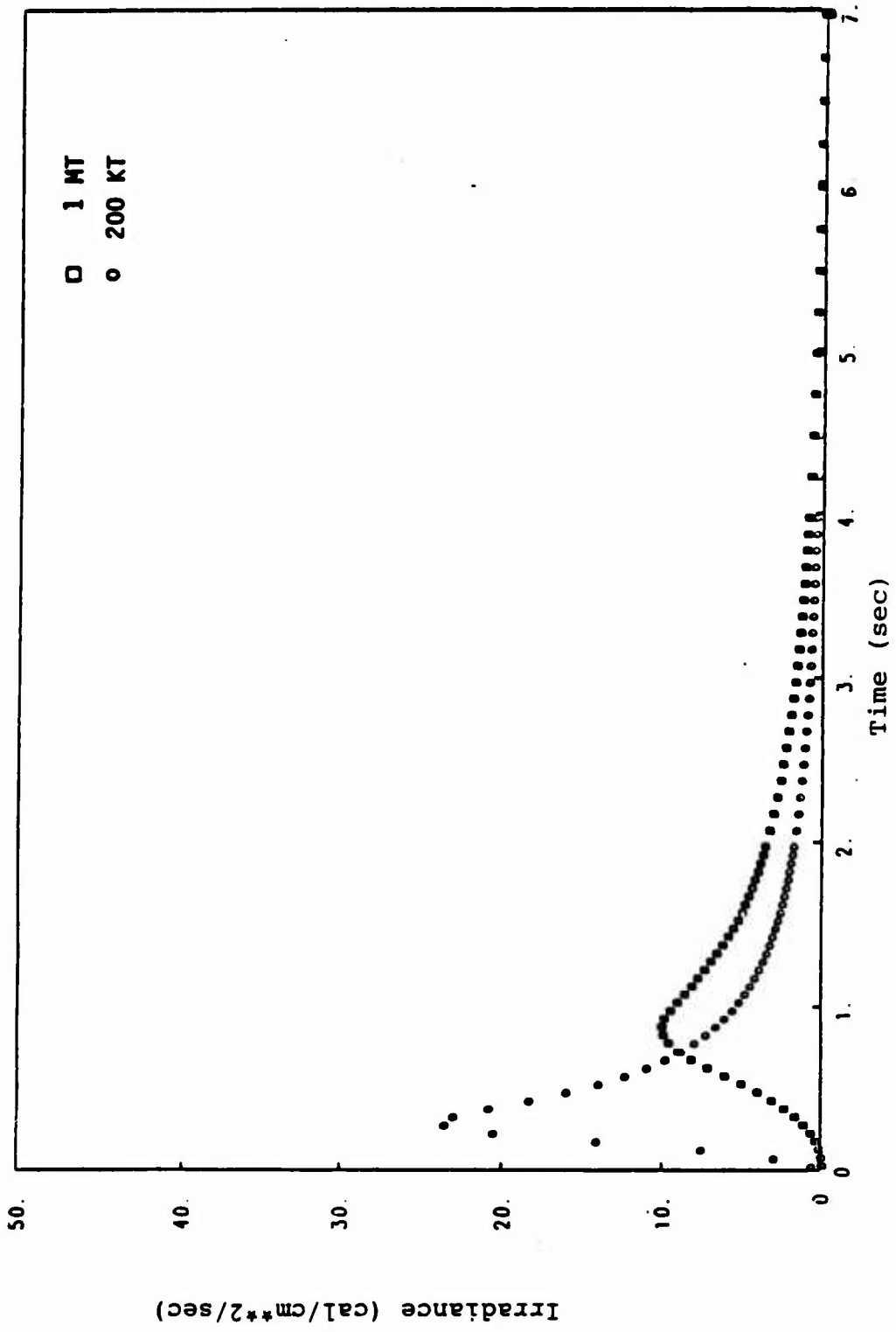

Figure 16. Irradiance Predicted with the Standard Time Factor Mesh for Bursts at 1 KFT Altitude Coaltitude at the 20 Cal/CM² Exposure Level.

3.1.3 Spectral Dependence.

Previous USANCA prediction techniques have not explicitly addressed the spectral dependence of the thermal energy. The spectral distribution of the power from the fireball is of importance primarily for determining the atmospheric transmission from the fireball to the receiver and also to a lesser extent in determining the absorptivity of the material.

As was discussed in the last section, the spectral dependence of the power in RECIPE is described by 26 energy groups which span the wavelength range from 200 to 12500 nm. All of the curve fitting in the code is done as a function of these energy groups and the basic power matrices are developed with the units of watts per eV. These spectral power matrices are used to compute the energy in calories per second in each wavelength band before being combined with the atmospheric transmission factor and the spectral response functions in order to calculate the total energy deposited in the material of interest.

In Figure 17 the spectral distribution is shown for 100 kt burst at several burst altitudes. These curves are obtained by integrating the power matrices over time and represent the distribution for the total energy radiated from the fireball. Each curve has been normalized to unity. The free air bursts all have essentially the same distribution except the bursts at higher altitudes tend to be more sharply peaked and contain more energy in the UV portion of the spectrum. The surface burst is seen to be definitely shifted to longer wavelengths indicating the effects of the ground surface on reducing the radiating temperature of the fireball and the increased absorption from the entrained material. Most of the energy is concentrated in the visible portion of the spectrum with a small fraction having a wavelength greater than one micron.

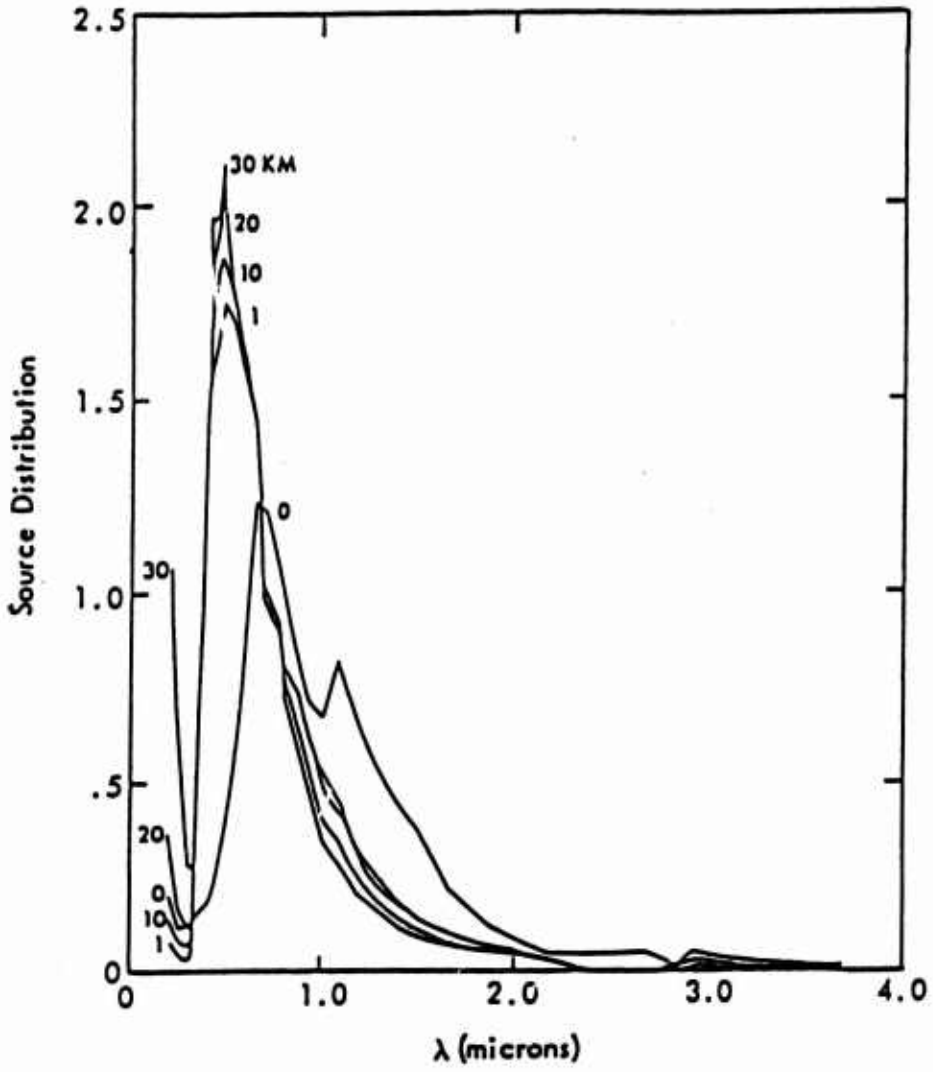

Figure 17. Effect of Altitude on Spectral Distribution, 100 Kilotons.

In Figure 18 the source distribution is displayed in a different manner for 100 kt bursts at a 1 km altitude and on the surface. The fraction of the energy in the TRAX (KSC Monte Carlo transmission code) wavelength intervals is shown for the two different altitudes. The surface burst definitely contains a larger fraction of the energy at the longer wavelengths. As shown, the QRT data base wavelengths grid is not sufficient to adequately describe the spectral output. This will be discussed in Section 5.

In Figure 19 the spectral distribution for times of .5T2MAX, T2MAX and 10T2MAX as well as the integration over time is shown for the 100 kt example considered in the previous section. There is not a strong time dependence in the spectrum, but the full detail is available in the RECIPE code and is utilized in the updated routines. Similar spectral distributions are shown in Figure 20 for the 1 Mt case. These types of variations will not change the time dependent energy absorptions by a large amount unless the absorptivity shows a very large wavelength dependence. Analyses involving windshields and specialized materials such as photochromic panels will require this type of detail.

3.1.4 Fireball Radius and Altitude Model.

Routines have been added to TAXV which were derived from RANCIV routines (Reference 15) which give the fireball center as a function of altitude. The original RANCIV routines give both the altitude and dimensions of the fireball as a function of time for particular burst altitudes and yields. The progression of the fireball from a sphere to an oblate spheroid to a torus is represented. The later time development into a torus as modeled by RANCIV is not of importance for thermal applications because the radiant output is much less than at earlier times. The

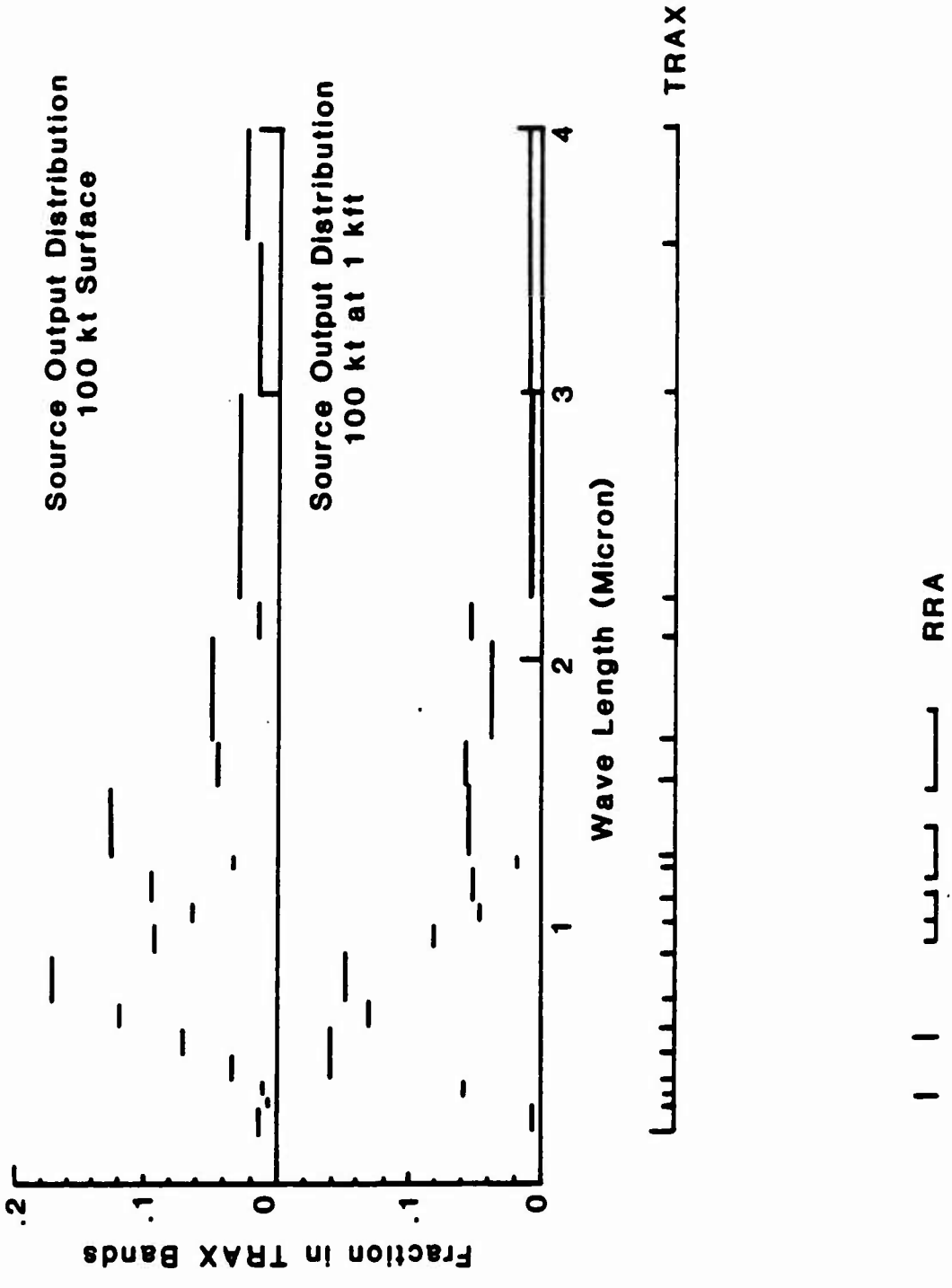

Figure 18. Source Distribution for TRAX and QRT Codes.

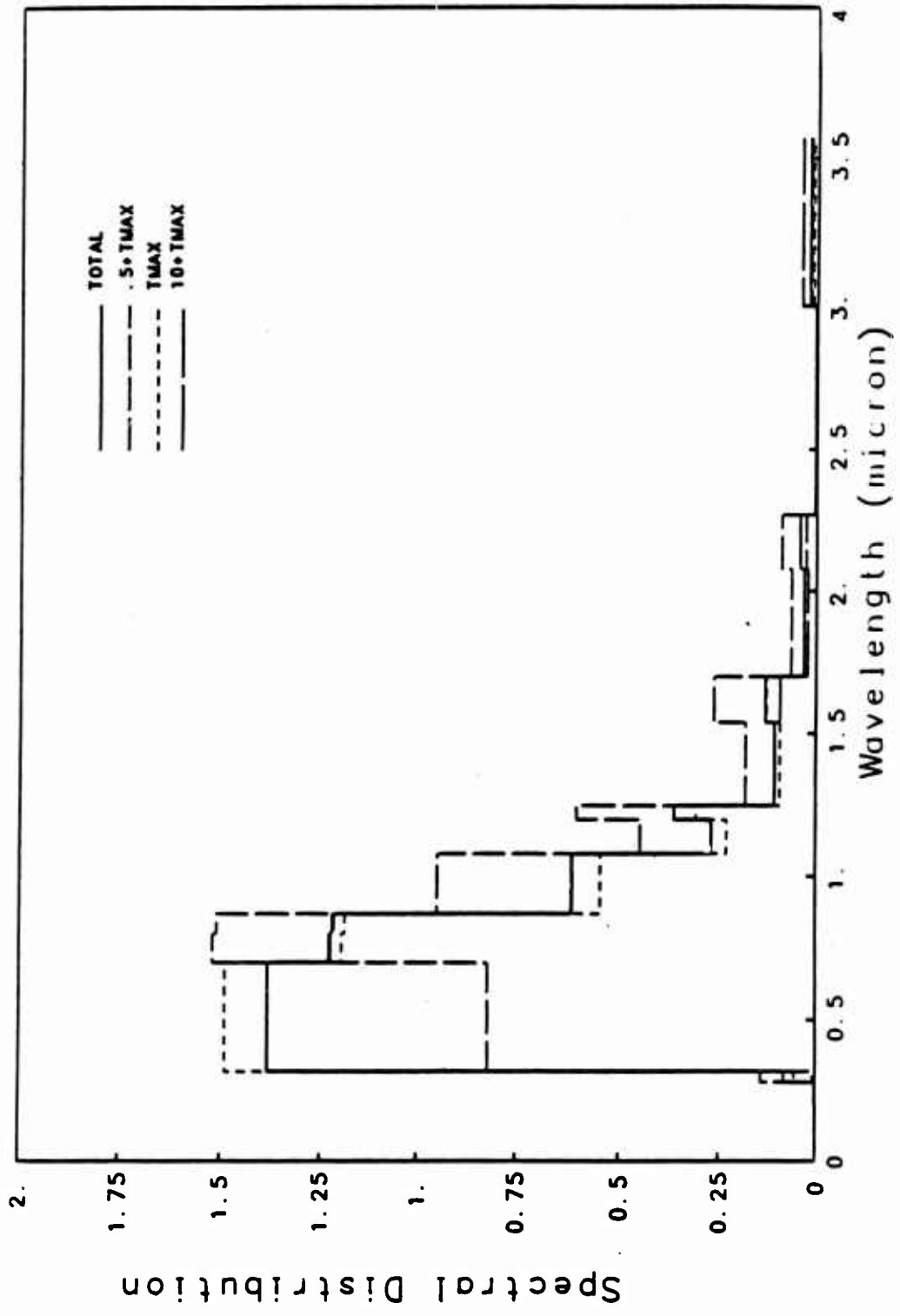

Figure 19. Spectral Distribution Received a Distance of 21 KFT Coaltitude From a 100 KT Burst.

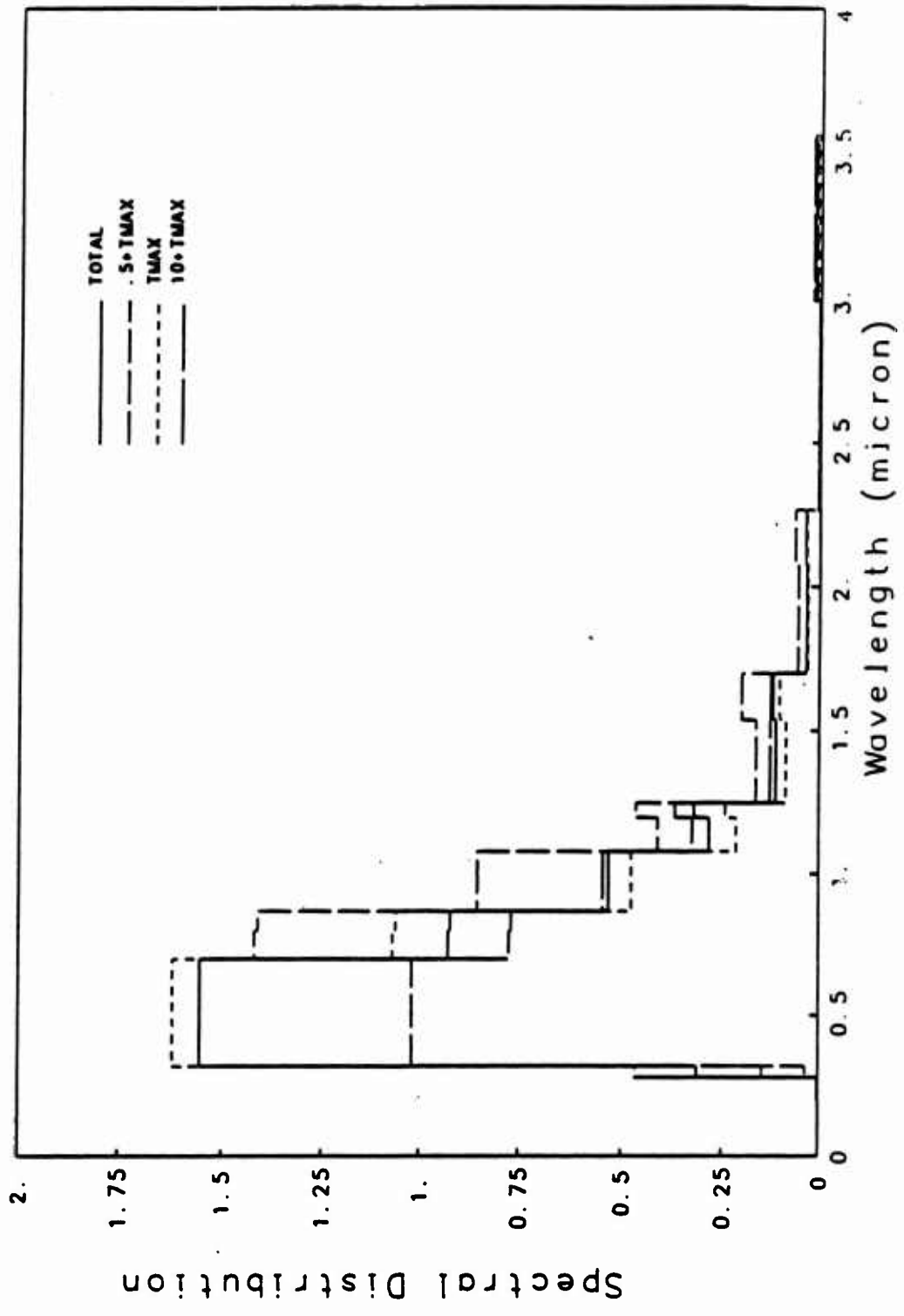

Figure 20. Spectral Distribution Received a Distance of 31 KFT Coaltitude From a 1 MT Burst.

combination of the RECIPE dimension modeling including the early time distortions due to surface effects and the simplified RANCIV fireball altitude modeling results in simple fast running algorithms adequate for thermal response calculations. Especially considering the fact that for USANCA applications, the receiver point is seldom close to the fireball. The NORSE/ROSCOE routines under current development were not used because versions are not available for distribution and because the complexity of these routines including multiburst effects is not warranted.

3.2 KSC MONTE CARLO DATA BASE.

The TRAX code was developed at KSC to generate a Monte Carlo data base of thermal transport results in the atmosphere, specifically aimed at nuclear weapons effects applications. The TAXV code was developed to utilize the TRAX data base in the most efficient and accurate manner and to easily couple to the RECIPE source output model for thermal exposure calculations. These codes have been exercised and improved by KSC as a result of several DNA, BMD, and USANCA contracts.

TRAX is a very general Monte Carlo transport code that was developed specifically for generating thermal exposure predictions from nuclear weapons in the atmosphere. The code was originally developed during the preparation of Reference 12 which contains a comprehensive discussion of all thermal data collected on the U.S. nuclear test series, a theoretical description of thermal output from fireballs, a detailed discussion of atmospheric transmission concentrating on applications to thermal exposure predictions, and an empirical derivation of the thermal partition as a function of yield and altitude. The TRAX code utilized previous work done by RAND in atmospheric transmission, but incorporated many features that corrected shortcomings in their approach which are still contained in the QRT code (Reference 14). The TRAX code was developed with very efficient path selection techniques, efficient broad band absorption techniques,

and a 2-D scoring technique. The scoring technique uses a path extension approach which increases scoring efficiency with minimal computing time increase. The RRA codes rely heavily on theoretical narrow band IR absorption techniques while the TRAX code uses broad band experimental results to most efficiently handle the energy in the IR portion of the nuclear output spectrum.

Eighteen wavelength bands are currently used in the calculations being done at KSC. These bands are indicated in Table 7 with the absorption type also shown as originally defined for the TRAX code. For each band in addition to the absorption reactions shown, the Rayleigh scattering from the molecular constituents and Mie scattering from the aerosol particles suspended in the atmosphere are considered. The cross sections and the angular phase functions for both scattering functions are calculated at the midpoint of the bands. As shown in section 3.1.3 this band structure provides good coverage of the nuclear output spectrum.

The transmission (T_λ) along a path is computed by the expression:

$$T_\lambda = e^{-\frac{\left|\tau_\varphi(\lambda,h_1) - \tau_\varphi(\lambda,h_2)\right|}{h_1 - h_2} \times R} \times T_{IR}(\lambda,h_1,h_2,R) \qquad (19)$$

where h_1, h_2 = altitudes at the extremes of the path segment

$\tau_\varphi(\lambda, h_1)$ = total extinction optical depth

R = slant path length

λ = wavelength

$T_{IR}(\lambda,h_1,h_2,R)$ = IR absorption factor.

If $h_1 = h_2$ then the argument of the exponential is replaced by the quantity $\sigma_e(\lambda, h_1)R$ where $\sigma_e(\lambda, h_1)$ is the total extinction cross section which is given as the sum of the Rayleigh and Mie scattering cross section and the ozone absorption cross section.

Table 7. Trax Band Structure.

BAND WAVELENGTH (μ)	BAND LIMITS (μ)	ABSORPTION TYPE
0.25	0.2 - 0.3	Ozone
0.32	0.3 - 0.34	Ozone
0.36	0.34 - 0.4	Ozone
0.45	0.4 - 0.5	Ozone
0.55	0.5 - 0.6	Ozone
0.65	0.6 - 0.7	Ozone
0.80	0.7 - 0.8696	Ozone
0.94	0.8696 - 0.9901	H_2O
1.03	0.9901 - 1.075	None
1.10	1.075 - 1.205	H_2O
1.23	1.205 - 1.253	None
1.38	1.253 - 1.538	$H_2O + CO_2$
1.60	1.538 - 1.695	CO_2
1.87	1.695 - 2.083	$H_2O + CO_2$
2.17	2.083 - 2.273	None
2.70	2.273 - 2.994	$H_2O + CO_2$
3.20	2.994 - 3.571	H_2O
3.80	3.571 - 4.00	None

The altitude mesh used was 1 km steps up to 50 km but this mesh is easily changed and extended. For Rayleigh and Mie scattering and ozone absorption. The cross section σ_R, σ_a, and σ_{03} the optical depth τ_R, τ_A and τ_{03} are given as a function of altitude and wavelength. The total extinction cross section σ_e and the total optical depth τ_e is also given. The

optical depths are defined from the top of the atmosphere downward instead of the other direction because less precision is required to accurately compute differences needed in the calculations. Defining the optical depths from the bottom may result in conditions where the inherent precision of a computer may be stressed in calculating the difference in the optical depths between two altitudes.

The IR transmission factor is calculated using experimentally derived parameters for the defined bands in the following manner. The basic data give the band absorption (A) as a function of the amount of absorber in the path segment and the average pressure along the path. For small amounts of absorber a weak fit is used:

$$A = CW^{\frac{1}{2}}p^{k} \tag{20}$$

and for larger amounts of absorber a strong fit is used:

$$A = C + D \log W + K \log P \tag{21}$$

where W is the integrated absorber and P is the pressure. A transition absorption is defined between the two fits. For CO_2 absorption then the transmission for the band is given by:

$$T_{CO2} = 1 - \frac{A_{CO_2}}{\Delta \nu} \tag{22}$$

where $\Delta \nu$ is the band width in wave numbers. The parameters used are given in Table 8.

Table 8. Carbon Dioxide Absorption Parameters*.

	Weak Fit		Transition	Strong Fit		
Band (μ)	C	K	A	C	D	K
1.38	.058	.41	80	-	-	-
1.60	.063	.38	80	-	-	-
1.87	.492	.39	80	-536	138	114
2.70	3.150	.43	50	-137	77	68

For water vapor absorption, it was found that at large amounts of absorber, the laboratory measurements did not agree with measurements performed in the atmosphere for these bands. A transition absorber was defined beyond which a power law fit to the transmission was used:

$$T_{H_2O} = AW^B \tag{23}$$

In Table 9 the parameters used for water vapor absorption are listed. For bands in which both water vapor and CO_2 absorption occur the expression:

$$A = A_{H_2O} + \frac{(1 - 2.36\, A_{H_2O})\, A_{CO_2}}{\Delta_\nu} \tag{24}$$

was used. Using these broad band expressions rather than narrow band values to represent a broad band provides a more accurate description of the IR absorption. The above absorption model has been compared with that obtained by integrating the Air Force Geophysical Laboratory (AFGL) narrow band absorption over the broad bands given above and a good agreement was found.

The TRAX code generates histories in a standard manner using the scattering cross sections to define path lengths, the

* From HBW, Reference 15.

Table 9. Water Vapor Absorption Parameters.

Band (μ)	Weak Fit* C	K	Transition Absorption	Strong Fit* C	D	K	Transition W_{H_2O}	Power Fit* B
.94	38	.27	200	-	-	-	1.0	-.0997
1.1	31	.26	200	-	-	-	1.0	-.1798
1.38	163	.30	350	202	460	198	0.1	-.1652
1.87	152	.30	275	127	232	144	1.0	-.1933
2.7	316	.32	200	337	246	150	1.0	-.31
3.2	40.2	.30	500	-	-	-	0.4	-.2425

* From HBW, Reference 7.

** Fits to Yates and Taylor data, Reference 8.

scattering phase functions to define particle directions, and at each collision adjusts the weight of the particle to allow for the possibility of being absorbed along the path. Because of the nonlinear characteristics of the broad band absorption, the cumulative absorber depth traversed is used to compute the particle weight. A form of extended path length scoring is used which reduces the variance of the Monte Carlo score. This is done by computing the probability that a path segment could have reached any scoring surface in the direction of propagation if the scattering had not taken place. This provides a safe method of increasing the efficiency of the code without introducing any bias in the answer as other variance reduction techniques do unless carefully used.

The scoring is performed in a defined altitude and horizontal range mesh and with sampling angles defined relative to the source to receiver vector. The scoring gives the scattered flux received on a flat plate detector at the location and with the direction defined. The scattered flux is itself never used directly for exposure predictions. Instead, the scattered flux is used to determine the buildup factor which is a ratio of the total flux received at the receiver point (direct flux plus the scattered flux) divided by the direct flux.

The buildup factor shows a much more predictable variation with geometry parameters and wavelength than does the scattered flux. In the IR region as shown in Table 7, the defined bands include bands with strong absorption and also bands where no absorption occurs representing windows in the spectrum. In Figure 18, typical results are shown for an atmosphere defined for Nevada atmospheric conditions for several wavelengths. In this case the total transmission is plotted as a function of horizontal range. The .32 and the .55 bands do not include absorption and the lower transmission for .32 is due to the much larger scattering cross sections at the lower wavelengths. In the IR region, note that .94 shows a relatively strong absorp-

tion, 1.23 shows essentially no absorption, and 1.87 shows strong absorption. The 1.23 band has no IR absorption and the reduction in the transmission is due only to the small scattering that occurs at this wavelength. A plot of the transmission or the total flux which is an equivalent quantity as a function of the wavelength would show no obvious trend with wavelength as will be shown in Section 5 in discussing the QRT approach.

However, when the buildup factors are plotted as a function of wavelength as is done in Figure 22, a very obvious trend is observed. There is seen to be a very well defined trend in the buildup factor versus scattering optical depth as one expects from elementary transport theory, but also a well defined variation with wavelength which might not have been predicted. The cross section decreases with increasing wavelength in a smooth manner and likewise the buildup factor also decreases with wavelength. The magnitude of the total flux at a point in space depends strongly on the wavelength, but the ratio of the total flux to the direct flux does not. This forms the basis for all of the predictive codes used at KSC and allows for much more accurate scaling of the Monte Carlo results than is obtained by using the scattered flux as is done in the QRT code.

A problem with the current KSC data base is that the data were developed prior to a redefinition of model atmospheric parameters at AFGL. The newer models have been incorporated into newer TAXV routines as described in Section 3.4.

Sample buildup factor results have been generated with the TRAX results to define the applicability of the current results. The buildup factors for the data base aerosol distribution and the rural and maritime aerosol distributions are shown in Figure 23 as a function of scattering optical depth for a wavelength of .55 microns for a meteorological range of 23 km. The 1 sigma bounds for the data base points are shown. Minor differences are noted for scattering optical depths of about 1.3 corresponding to

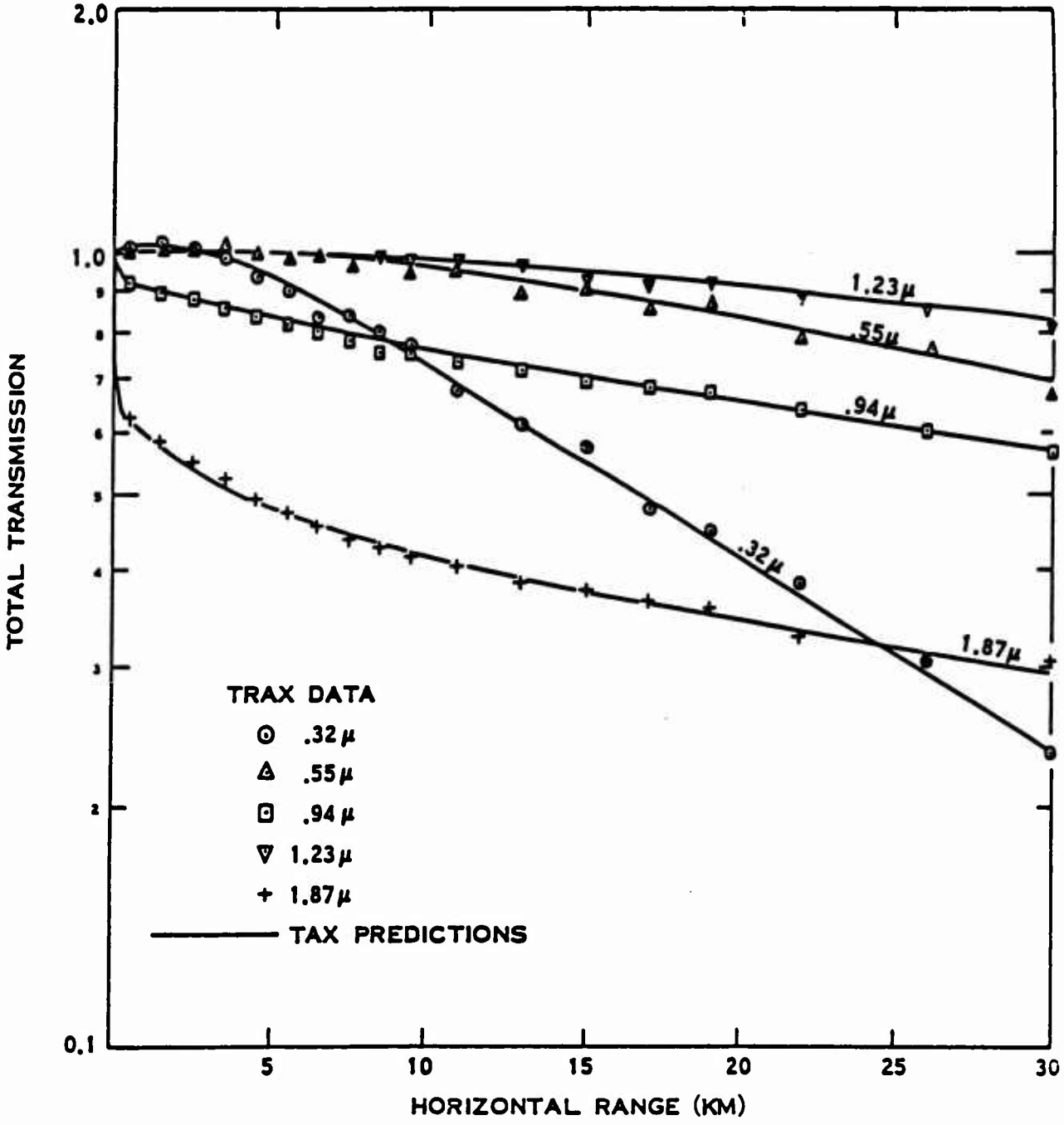

Figure 21. Comparison of Tax Results with TRAX Data Nevada Atmosphere with Ground Level at 1.28 KM Source 1 KM Above Ground. Receiver 3 M Above Ground.

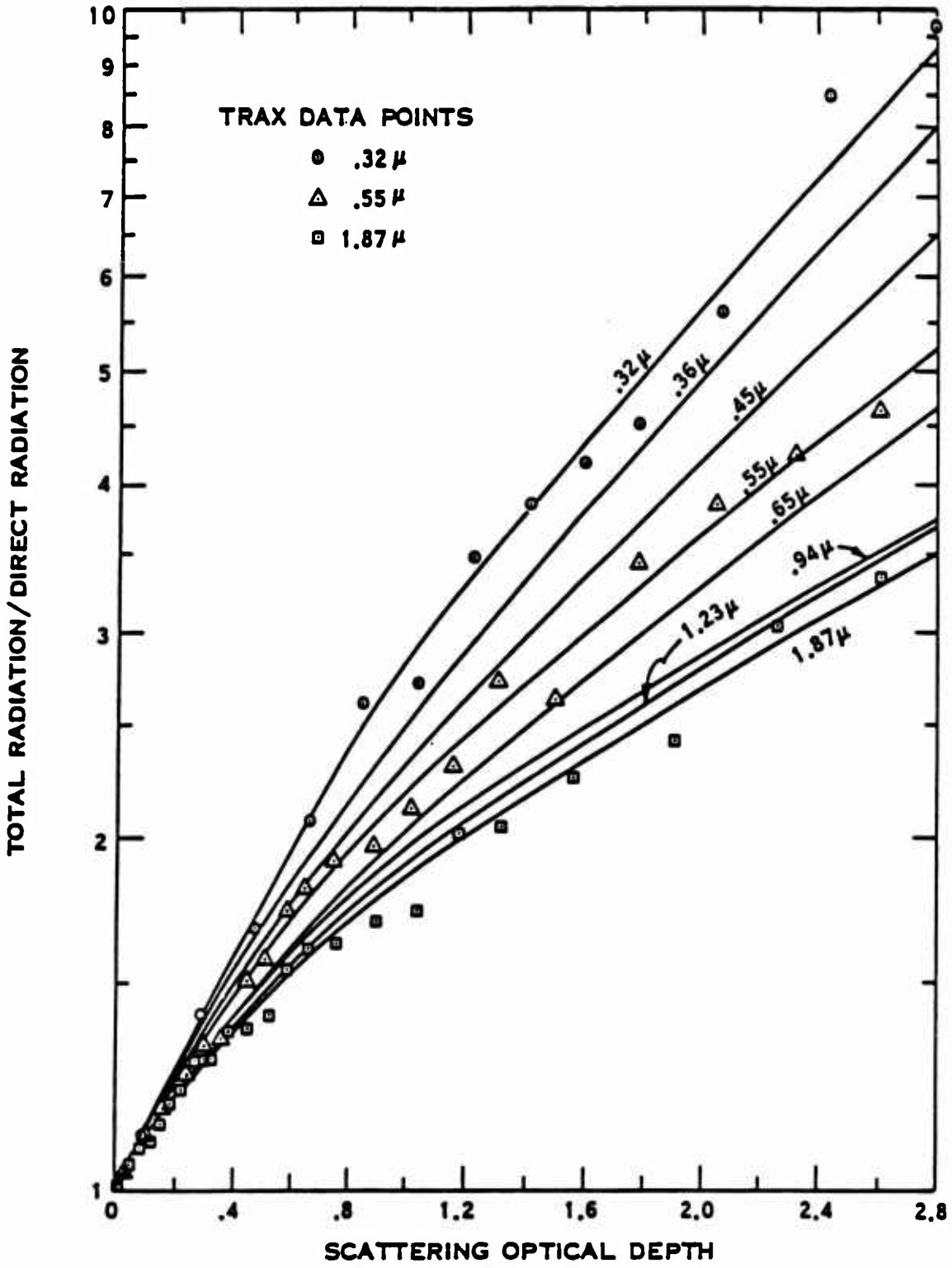

Figure 22. Comparison of Build-up Factors vs the Scattering Optical Depth for Various Wavelengths. Pacific Atmosphere with Both Source and Sampling at 1 km Altitude.

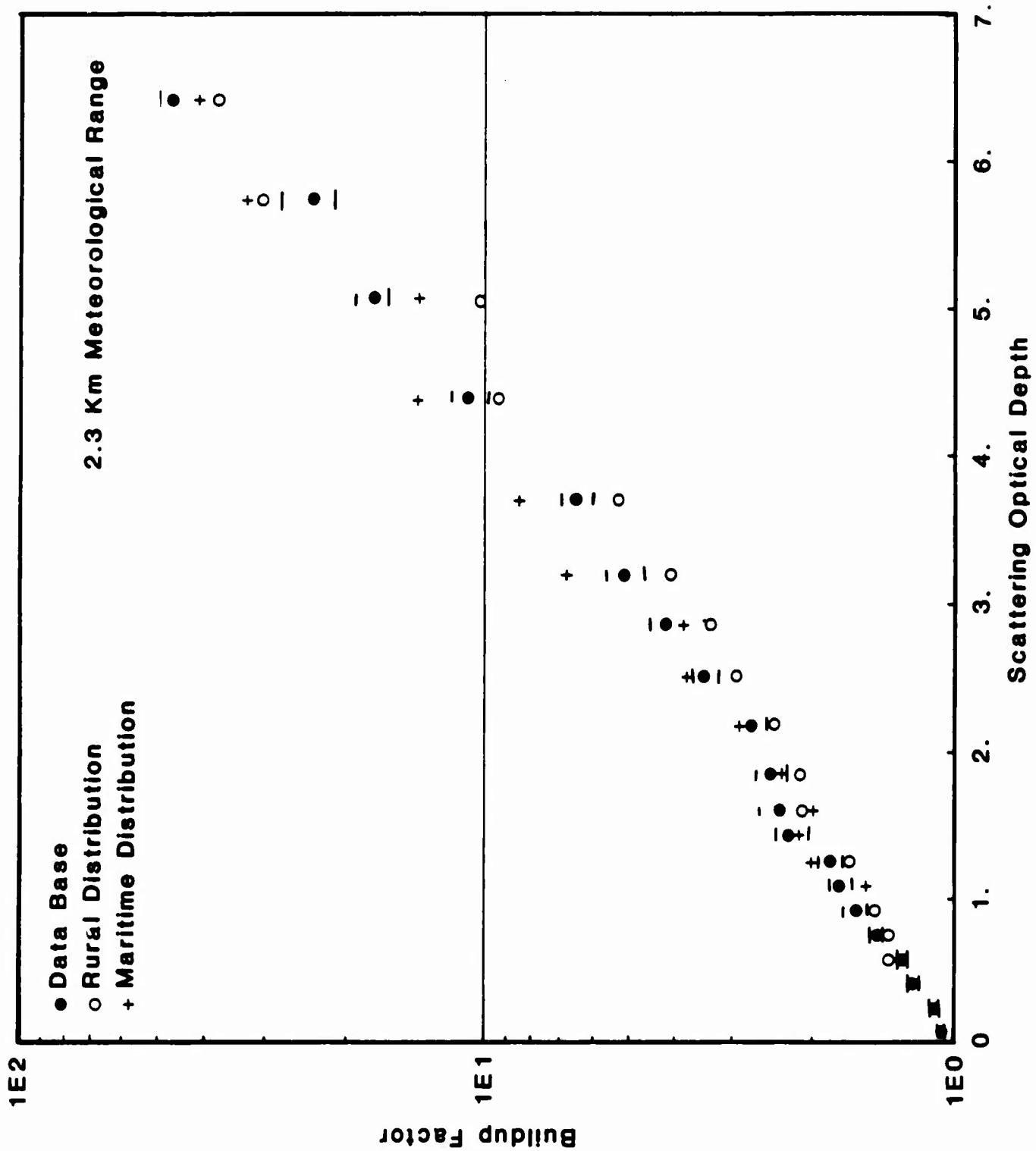

Figure 23. Comparison of Build-up Factors for Surface Burst.

ranges of 7.5 km. Figure 24 and 25 show corresponding results for meteorological ranges of 10 and 2 km. The corresponding ranges 9.5 and 1.5 km for 10 and 2 km meteorological ranges respectively show which data base results are acceptable.

For 100 kt yields the predictions are acceptable down to 2 cal/cm² for meteorological ranges greater than 10 km. For lower meteorological ranges the predictions are valid for exposures greater than about 40 cal/cm². For 1 Mt yields the exposure predictions curves are good for exposures greater than 20 cal/cm². For low meteorological ranges the prediction are valid only for exposures over about 400 cal/cm².

These boundary conditions indicate that data base revisions are necessary to adequately define the probabilistic transmissions for USANCA applications. As discussed above the transmissions are valid only for large meteorological ranges. The probabilistic transmissions are accurate only for the higher probabilities.

3.3 WEATHER ANALYSIS REQUIREMENTS.

In the previous section the UK weather analysis was discussed. The main factors considered in their analysis was the visibility and the cloud ceiling. Other factors need to be considered in order to perform accurate thermal predictions.

A set of weather parameters is needed for developing the basic Monte Carlo data base. As discussed in the previous subsection a very detailed set of atmospheric parameters are needed for these calculations. These include the aerosol and Rayleigh cross section, water vapor, carbon dioxide, density ozone, temperature and pressure as a function of altitude. Also needed, are the Rayleigh and aerosol scattering phase function. The latter of which depends upon the specific aerosol size dis-

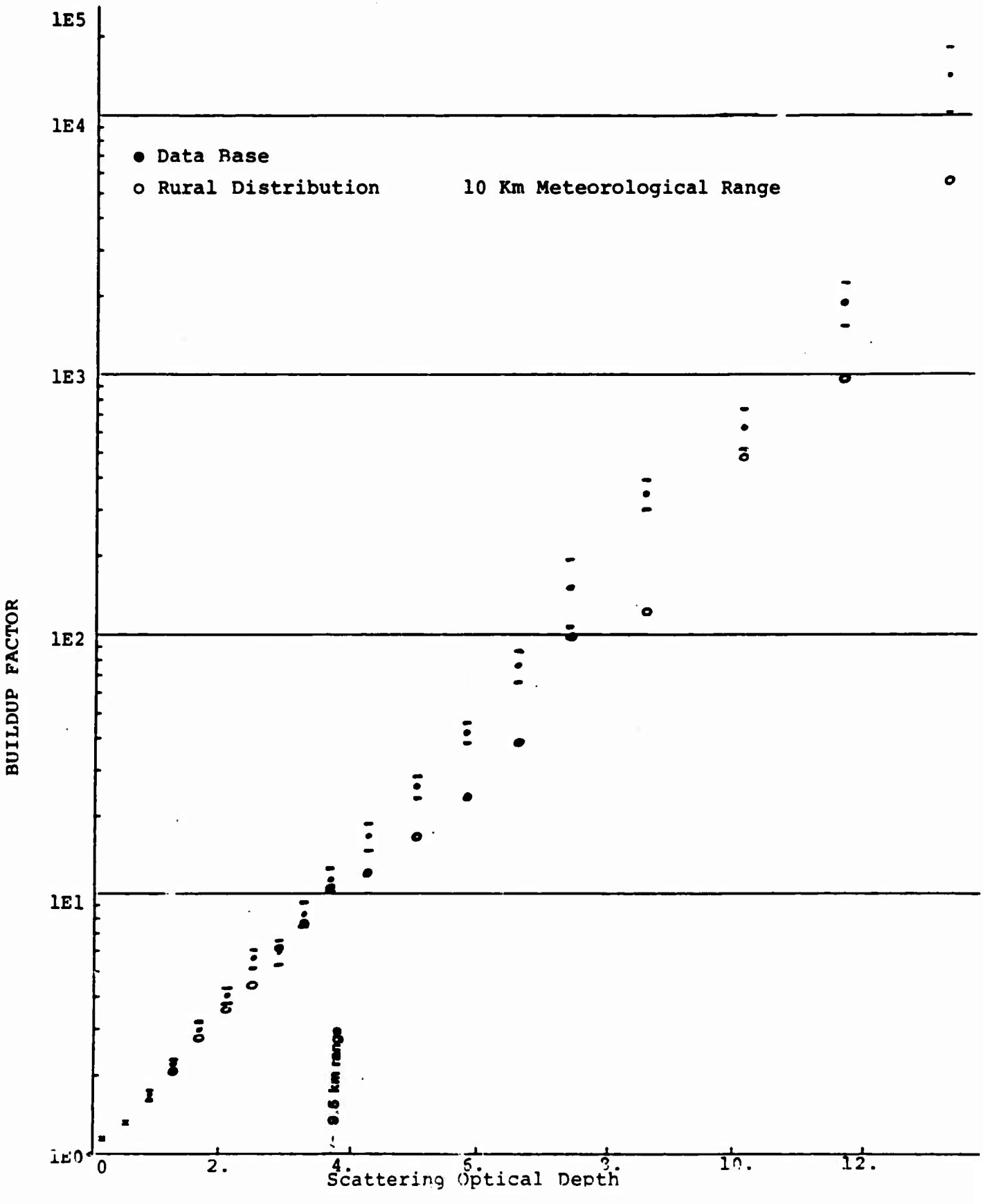

Figure 24. Comparison of Build-up Factors for Surface Burst.

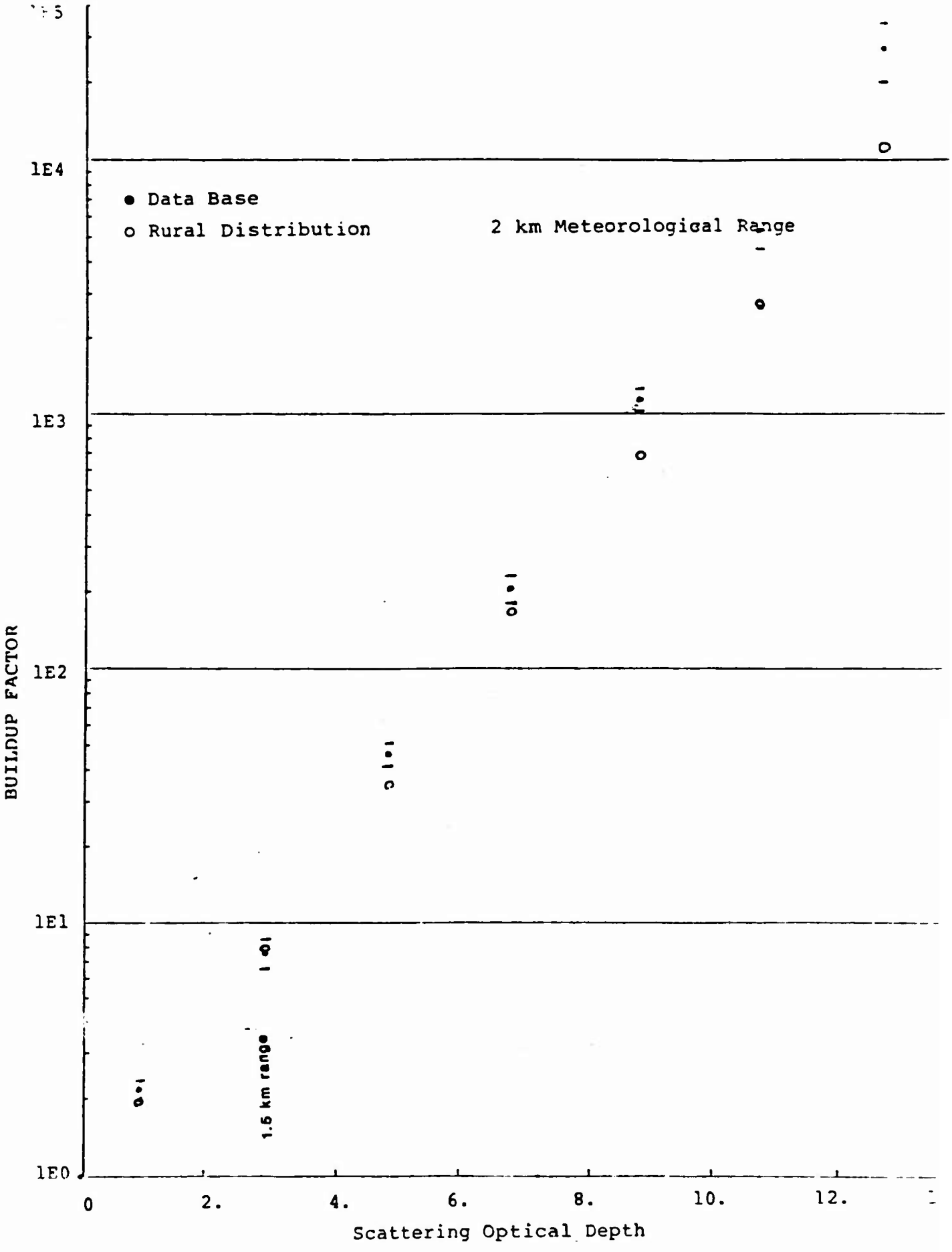

Figure 25. Comparison of Build-up Factors for Surface Burst

tribution chosen. The ground surface and cloud cover altitudes and reflecting characteristics are also needed.

The basic atmospheric constituents chosen for future work correspond to the mid-latitude fall-winter and the mid-latitude spring-summer conditions (Reference 17). The spring-summer model has a higher water vapor concentration than the fall-winter model and represents the constituent having the widest variation.

The aerosol model chosen (Reference 14) corresponds to a rural aerosol distribution with a ground surface meteorological range of 23 km. The basic parameter is the aerosol cross section (km^{-1}) for the .55 micron band as a function of altitude. This parameter is the same for both model atmospheres at the lower altitudes. The code permits a different meteorological range at the surface to be chosen, and the aerosol cross section is adjusted at the lower altitudes in the boundary layer to obtain the required meteorological range. A similar procedure is used to alter the water vapor distribution at the lower altitudes.

In Table 10 the aerosol, Rayleigh and ozone parameters are given for the spring-summer model for the .55 micron band. For each constituent both the cross section σ(km^{-1}) and the optical depth τ are given. The total extinction cross section and optical depth are obtained by summing the three components. Corresponding values for the fall-winter model are given in Table 14.

Figures 26, 27 and 28 show the Rayleigh, aerosol and ozone cross sections as a function of altitude. The solid line refers to the fall-winter atmosphere and the dashed line refers to the spring-summer atmosphere.

These parameters are stored in the code, and whenever values of σ_e or T_e are needed to compute the transmission, interpola-

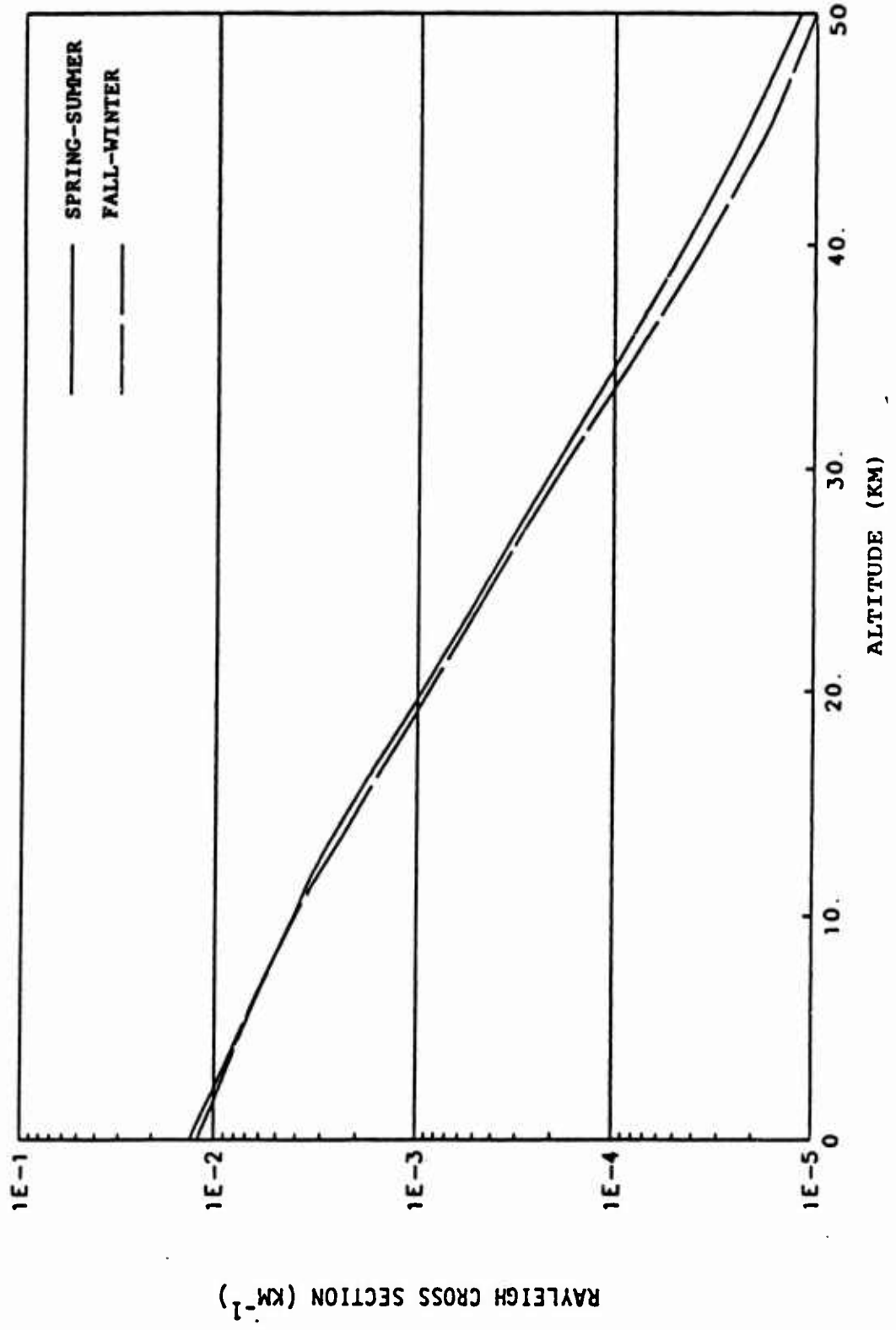

Figure 26. Comparison of Rayleigh Cross Section for Two Model Atmosphere.

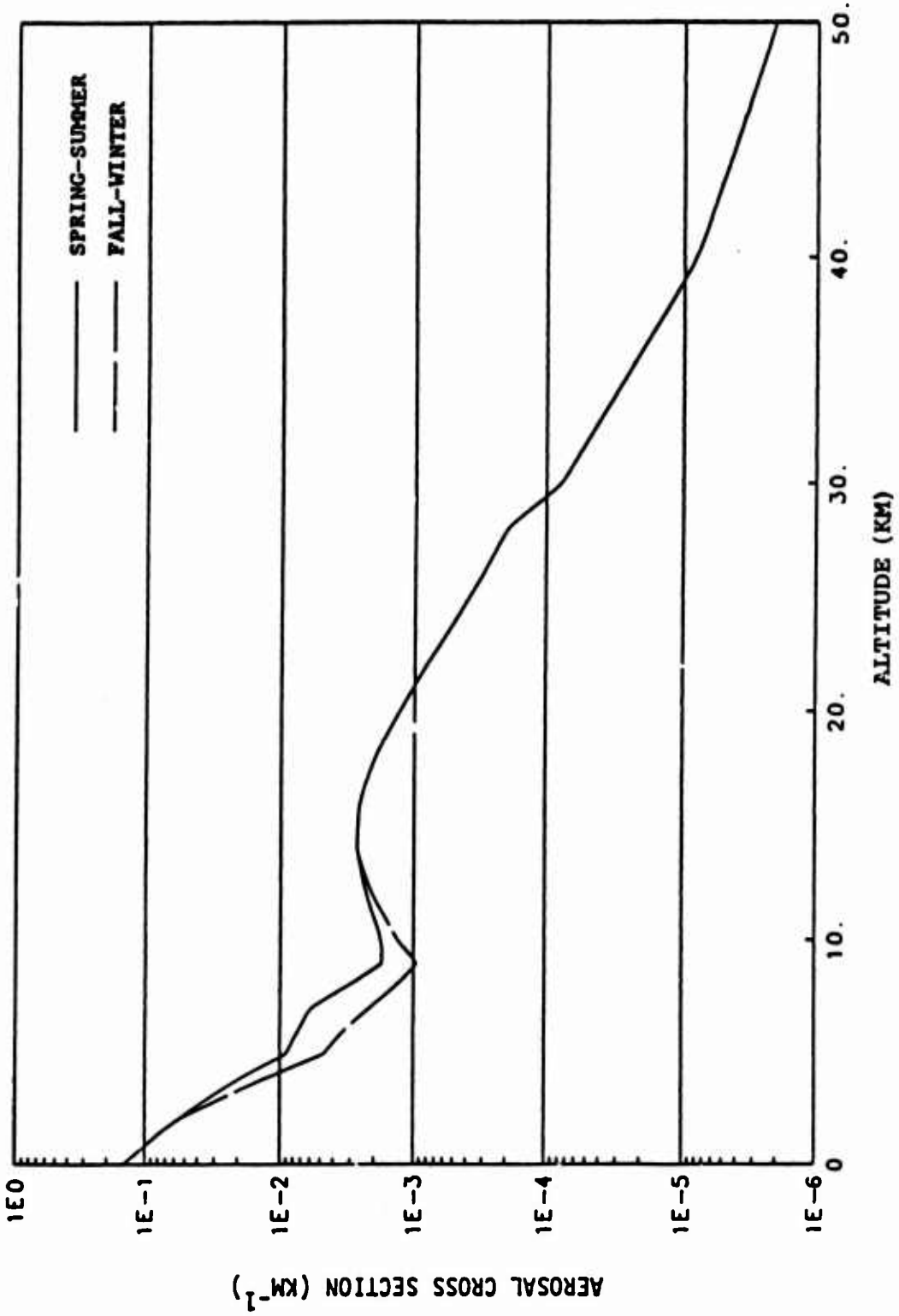

Figure 27. Comparison of Aerosol Cross Section for Two Model Atmosphere.

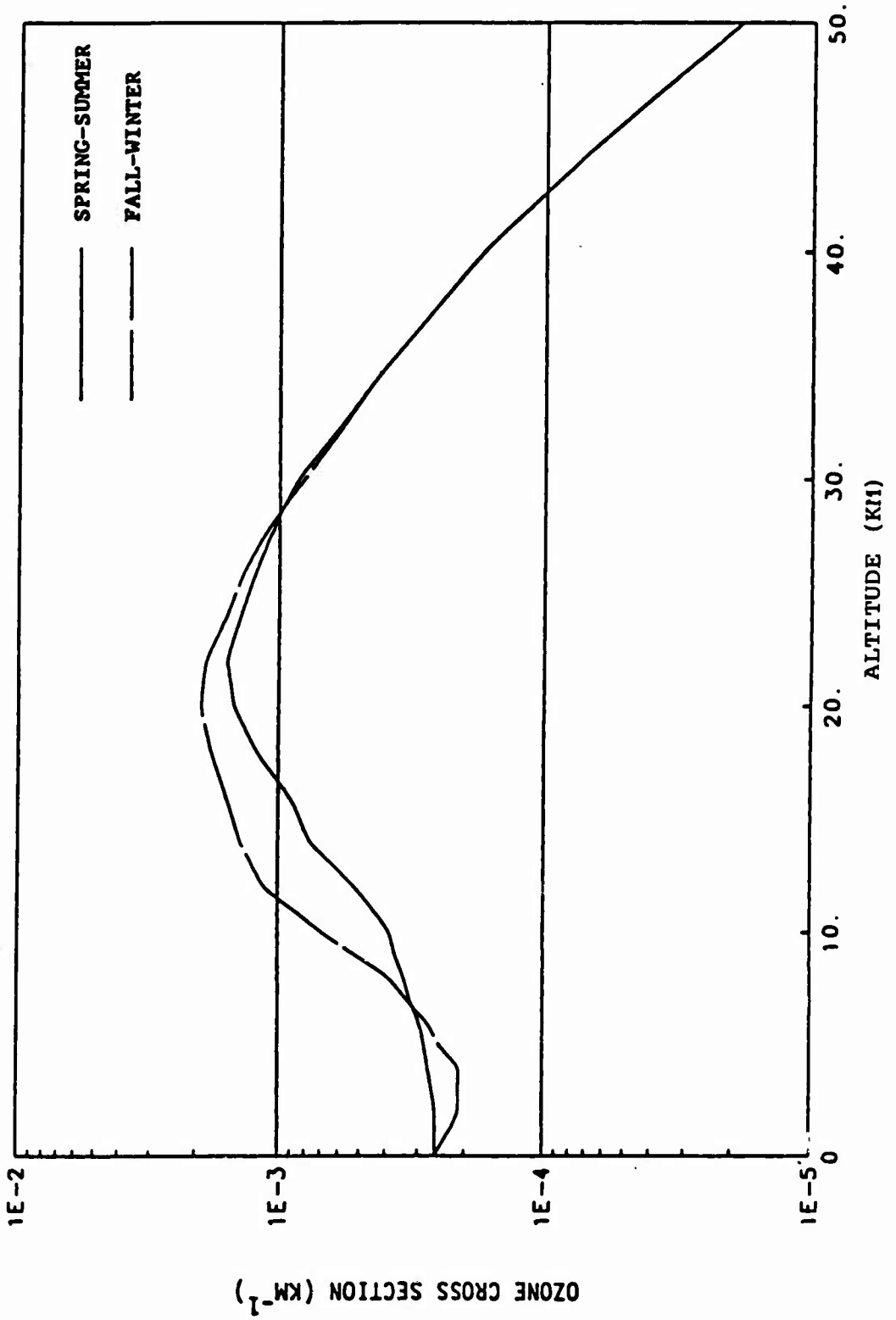

Figure 28. Comparison of Ozone Cross Section for Two Model Atmosphere.

Table 10. Scattering Parameters for the Spring-Summer Model Atmosphere.

ALTITUDE (KM)	RAYLEIGH CROSS SECTION (KM^{-1})	RAYLEIGH OPTICAL DEPTH	AEROSOL CROSS SECTION (KM^{-1})	AEROSOL OPTICAL DEPTH	OZONE CROSS SECTION (KM^{-1})	OZONE OPTICAL DEPTH
0.0	1.188E-02	1.081E-01	1.461E-01	3.290E-01	2.579E-04	2.933E-02
1.0	1.076E-02	9.180E-02	9.214E-02	2.119E-01	2.579E-04	2.907E-02
1.5	1.023E-02	8.655E-02	7.371E-02	1.706E-01	2.579E-04	2.894E-02
2.0	9.727E-03	8.156E-02	5.780E-02	1.379E-01	2.579E-04	2.881E-02
3.0	8.819E-03	7.229E-02	3.297E-02	9.368E-02	2.665E-04	2.855E-02
4.0	7.972E-03	6.390E-02	1.763E-02	6.917E-02	2.751E-04	2.828E-02
5.0	7.189E-03	5.633E-02	8.861E-03	5.643E-02	2.873E-04	2.800E-02
6.0	6.467E-03	4.951E-02	7.346E-03	4.835E-02	2.966E-04	2.771E-02
7.0	5.811E-03	4.338E-02	5.926E-03	4.174E-02	3.7224-04	2.740E-02
8.0	5.209E-03	3.787E-02	3.201E-03	3.731E-02	3.396E-04	2.707E-02
9.0	4.654E-03	3.295E-02	1.725E-03	3.493E-02	3.697E-04	2.671E-02
10.0	4.146E-03	2.855E-02	1.753E-03	3.391E-02	3.869E-04	2.633E-02
12.0	3.259E-03	2.118E-02	2.321E-03	2.914E-02	5.159E-04	2.544E-02
14.0	2.455E-03	1.551E-02	2.738E-03	2.409E-02	7.738E-04	2.417E-02
16.0	1.793E-03	1.129E-02	2.596E-03	1.876E-02	9.028E-04	2.243E-02
18.0	1.301E-03	8.224E-03	1.989E-03	1.420E-02	1.204E-03	2.040E-02
20.0	9.423E-04	6.000E-03	1.279E-03	1.099E-02	1.462E-03	1.774E-02
22.0	6.850E-04	4.387E-03	8.147E-04	8.926E-03	1.548E-03	1.473E-02
24.0	4.998E-04	3.212E-03	4.879E-04	4.385E-03	1.376E-03	1.181E-02
26.0	3.660E-04	2.353E-03	3.031E-04	1.091E-03	1.204E-03	9.239E-03
28.0	2.681E-04	1.724E-03	1.989E-04	5.965E-04	1.032E-03	7.008E-03
30.0	1.964E-04	1.263E-03	7.561E-05	3.415E-04	8.598E-04	5.121E-03
35.0	9.242E-05	5.733E-04	2.414E-05	1.161E-04	4.083E-04	2.090E-03
40.0	4.491E-05	2.442E-04	7.959E-06	4.321E-05	1.763E-04	7.090E-04
45.0	2.223E-05	8.292E-05	3.948E-06	1.460E-05	5.877E-05	1.741E-04
50.0	1.199E-05	0.000E+00	2.089E-06	0.000E+00	1.849E-05	0.000E+00

Table 11. Scattering Parameters for the Fall-Winter Model Atmosphere.

ALTITUDE (KM)	RAYLEIGH CROSS SECTION (KM^{-1})	RAYLEIGH OPTICAL DEPTH	AEROSOL CROSS SECTION (KM^{-1})	AEROSOL OPTICAL DEPTH	OZONE CROSS SECTION (KM^{-1})	OZONE OPTICAL DEPTH
0.0	1.297E-02	1.036E-01	1.461E-01	2.989E-01	2.579E-04	3.662E-02
1.0	1.159E-02	9.136E-02	9.214E-02	1.819E-01	2.321E-04	3.637E-02
1.5	1.094E-02	8.573E-02	7.371E-02	1.406E-01	2.192E-04	3.626E-02
2.0	1.033E-02	8.042E-02	5.780E-02	1.079E-01	2.107E-04	3.615E-02
3.0	9.201E-03	7.066E-02	2.592E-02	6.812E-02	2.107E-04	3.594E-02
4.0	8.257E-03	6.194E-02	1.143E-02	5.043E-02	2.107E-04	3.573E-02
5.0	7.388E-03	5.412E-02	4.621E-03	4.291E-02	2.493E-04	3.550E-02
6.0	6.593E-03	4.714E-02	3.373E-03	3.894E-02	2.751E-04	3.524E-02
7.0	5.867E-03	4.092E-02	2.191E-03	3.620E-02	3.310E-04	3.494E-02
8.0	5.206E-03	3.539E-02	1.343E-03	3.447E-02	3.869E-04	3.458E-02
9.0	4.604E-03	3.049E-02	9.337E-04	3.334E-02	5.159E-04	3.413E-02
10.0	4.058E-03	2.617E-02	1.307E-03	2.223E-02	6.878E-04	3.353E-02
12.0	2.989E-03	1.917E-02	2.094E-03	2.890E-02	1.118E-03	3.176E-02
14.0	2.198E-03	1.403E-02	2.738E-03	2.409E-02	1.376E-03	2.928E-02
16.0	1.616E-03	1.024E-02	2.596E-03	1.876E-02	1.548E-03	2.636E-02
18.0	1.185E-03	7.465E-03	1.989E-03	1.420E-02	1.768E-03	2.305E-02
20.0	8.663E-04	5.431E-03	1.279E-03	1.099E-02	1.935E-03	1.936E-02
22.0	6.320E-04	3.945E-03	8.147E-04	8.926E-03	1.894E-03	1.558E-02
24.0	4.610E-04	2.861E-03	4.879E-04	4.385E-03	1.548E-03	1.219E-02
26.0	3.363E-04	2.070E-03	3.031E-04	1.091E-03	1.333E-03	9.314E-03
28.0	2.447E-04	1.494E-03	1.989E-04	5.965E-04	1.076E-03	6.915E-03
30.0	1.778E-04	1.075E-03	7.561E-05	3.415E-04	8.168E-04	5.036E-03
35.0	7.908E-05	4.657E-04	2.414E-05	1.161E-04	4.083E-04	2.090E-03
40.0	3.613E-05	1.915E-04	7.959E-06	4.321E-05	1.763E-04	7.090E-04
45.0	1.738E-05	6.343E-05	3.948E-06	1.460E-05	5.877E-05	1.741E-04
50.0	8.926E-06	0.000E+00	2.089E-06	0.000E+00	1.849E-05	0.000E+00

Table 12. Wavelength Dependent Cross Section Factors.

WAVELENGTH BAND (μ)	RAYLEIGH	AEROSOL	OZONE
.25	21.84	1.77	1.82E3
.32	9.48	1.58	9.76
.36	5.76	1.52	1.95E-2
.45	2.28	1.14	3.81E-2
.55	1.0	1.0	1.0
.65	5.08E-1	0.899	6.74E-1
.80	2.19E-1	0.804	1.09E-1
.94	1.15E-1	0.747	0.0
1.03	7.91E-2	0.722	0.0
1.10	6.05E-2	0.709	0.0
1.23	3.86E-2	0.684	0.0
1.38	2.45E-2	0.665	0.0
1.6	1.36E-2	0.630	0.0
1.87	7.23E-3	0.595	0.0
2.17	3.99E-3	0.557	0.0
2.7	1.67E-3	0.506	0.0
3.2	8.10E-4	0.465	0.0
3.8	4.03E-4	0.415	0.0

tion in these tables is performed. The tables contain values for the .55 μ band. Values for other bands are calculated using the ratios (K) in Table 12 as follows:

$$\sigma(\lambda, H) = K(\lambda) * \sigma(.55, H). \tag{25}$$

The absorption expressions utilize the integrated amount of absorber (w) along the source to receiver path. If $H_s \neq H_r$ the amount of absorber is

$$w = |w(H_s) - w(H_r)| * R \quad |H_s - H_r| \tag{26}$$

where

$$w(H_s) = \int_{H_s}^{50} \rho dH \tag{27}$$

and ρ is the absorber concentration (either CO_2 or H_2O). If $H_s = H_r$ then

$$w = \rho * R. \tag{28}$$

For horizontal paths the pressure (P) used in the expression is the pressure at the relevant altitude. If $H_s \neq H_r$ then an average pressure is used defined by

$$P = \frac{Pw(H_s) - Pw_{(H_r)}}{w(H_s) - w(H_r)} \tag{29}$$

where

$$P_w(H_s) = \int_{H_s}^{50} P\rho dH. \tag{30}$$

The CO_2 density in these expressions is expressed in units of atmosphere-cm/km and the H_2O density is expressed in units of precipitable-cm/km. The unit atmosphere-cm refers to the depth of absorber resulting from the absorber traversing along a path which was reduced to STP conditions. This quantity is computed by integrating the absorber density along the path and dividing by the STP density. The carbon dioxide concentration is assumed constant at 0.0314 percent by volume for all altitudes with the number density as a function of altitude determined by the model atmosphere used. The units pr-cm are analogous with the definition of atmosphere-cm where it is assumed that the water vapor is converted to the liquid state of STP. Since the density at STP is essentially unity, $^{W}H_2O$ numerically is just the integral of the water vapor is g/cm² along the path.

The quantities $^{\rho}H_2O$, $^{\rho}CO_2$, $^{W}H_2O$ and $^{W}CO_2$ as a function of altitude as well as the quantities weighted by the pressure are needed to compute the IR absorption. In Table 13 the quantities $^{\rho}CO_2$, $^{W}CO_2$, and $^{\rho_W}CO_2$ are given as a function of altitude

for the spring-summer atmosphere model. Corresponding values are given in Table 14 for the fall winter model atmosphere. Likewise, in Tables 15 and 16 the corresponding values are given for the water vapor concentration.

In Figure 29 the carbon dioxide concentrations for the two model atmospheres are compared with the solid line representing the spring-summer and the dashed line representing the fall-winter model. In Figure 30 the water vapor density for the two models is compared. The spring-summer model is seen to be significantly wetter than the fall-winter at altitudes below about 10 km. The units are pr-cm/km and the values must be multiplied by 10 to obtain g/m^3.

The previously described atmospheric parameters are required for the basic Monte Carlo data base requirements and are also required as a basis for the prediction code TAXV to be described in the next section. In a specific transmission prediction run the weather parameters for that case need to be specified. The primary parameters of interest are: the ground and cloud ceiling altitudes and the percentage cloud cover, the visibility and the water vapor density along the ground surface, the model atmosphere type, and the ground albedo.

The ground surface visibility and water vapor density are used to define atmospheric properties in the boundary layer near the ground. The cloud and ground parameters are used to define albedo surface enhancement factors in the calculations.

In the UK weather analysis cloud ceiling above 3 km was equated with the absence of clouds. Actually, the transmission factor for a cloud ceiling at 6 km, for instance, is much larger than that obtained with no cloud layer. The 95% curve obtained with clouds is much higher than the curve without clouds. The effect this assumption had on thermal transmissivity curves can

Table 13. Carbon Dioxide Absorption Parameters for the Spring-Summer Model Atmosphere.

	CARBON DIOXIDE		PRESSURE * CARBON DIOXIDE	
ALTITUDE KM	DENSITY ATM-CM/KM	DEPTH ATM-CM	DENSITY MBAT-CM/KM	DEPTH MBATM-CM
0.0	3.042E+01	2.639E+02	3.084E+04	1.337E+05
1.0	2.755E+01	2.350E+02	2.485E+04	1.060E+05
1.5	2.620E+01	2.215E+02	2.228E+04	9.423E+04
2.0	2.490E+01	2.088E+02	1.996E+04	8.368E+04
3.0	2.257E+01	1.851E+02	1.604E+04	6.575E+04
4.0	2.041E+01	1.636E+02	1.282E+04	5.139E+04
5.0	1.840E+01	1.442E+02	1.019E+04	3.994E+04
6.0	1.655E+01	1.267E+02	8.055E+03	8.086E+04
7.0	1.488E+01	1.110E+02	6.343E+03	2.369E+04
8.0	1.333E+01	9.694E-01	4.965E+03	1.807E+04
9.0	1.191E+01	8.434E+01	3.859E+03	1.368E+04
10.0	1.061E+01	7.308E+01	2.981E+03	1.027E+04
12.0	8.342E+00	5.422E+01	1.740E+03	5.664E+03
14.0	6.285E+00	3.969E+01	9.585E+02	3.043E+03
16.0	4.589E+00	2.890E+01	5.108E+02	1.620E+03
18.0	3.330E+00	2.105E+01	2.704E+02	8.643E+02
20.0	2.412E+00	1.536E+01	1.435E+02	4.637E+02
22.0	1.754E+00	1.123E+01	7.663E+01	2.506E+02
24.0	1.279E+00	8.221E+00	4.123E+01	1.363E+02
26.0	9.368E-01	6.023E+00	2.234E+01	7.468E+01
28.0	6.862E-01	4.413E+00	1.215E+01	4.122E+01
30.0	5.028E-01	2.233E+00	6.647E+00	2.297E+01
35.0	2.366E-01	1.468E+00	1.543E+00	5.493E+00
40.0	1.150E-01	6.250E-01	3.828E-01	1.331E+00
45.0	5.690E-02	2.123E-01	9.827E-02	2.845E-01
50.0	3.068E-02	0.000E+00	2.919E-02	0.000E+00

Table 14. Carbon Dioxide Absorption Parameters for the Fall-Winter Model Atmosphere.

	CARBON DIOXIDE		PRESSURE * CARBON DIOXIDE	
ALTITUDE KM	DENSITY ATM-CM/KM	DEPTH ATM-CM	DENSITY MBAT-CM/KM	DEPTH MBATM-CM
0.0	3.320E+01	2.653E+02	3.380E+04	1.349E+05
1.0	2.966E+01	2.339E+02	2.661E+04	1.049E+05
1.5	2.801E+01	2.195E+02	2.359E+04	9.235E+04
2.0	2.645E+01	2.058E+02	2.089E+04	8.124E+04
3.0	2.355E+01	1.809E+02	1.634E+04	6.272E+04
4.0	2.114E+01	1.585E+02	1.285E+04	4.820E+04
5.0	1.891E+01	1.385E+02	1.005E+04	3.680E+04
6.0	1.688E+01	1.207E+02	7.809E+03	2.792E+04
7.0	1.502E+01	1.047E+02	6.031E+03	2.104E+04
8.0	1.333E+01	9.059E+01	4.628E+03	1.574E+04
9.0	1.179E+01	7.805E+01	3.527E+03	1.169E+04
10.0	1.039E+01	6.698E+01	2.667E+03	8.613E+03
12.0	7.650E+00	4.908E+01	1.440E+03	4.631E+03
14.0	5.627E+00	3.591E+01	7.754E+02	2.484E+03
16.0	4.136E+00	2.622E+01	4.169E+02	1.329E+03
18.0	3.032E+00	1.911E+01	2.231E+02	7.088E+02
20.0	2.218E+00	1.390E+01	1.190E+02	3.775E+02
22.0	1.618E+00	1.010E+01	6.334E+01	2.009E+02
24.0	1.180E+00	7.323E+00	3.370E+01	1.070E+02
26.0	8.609E-01	5.299E+00	1.794E+01	5.698E+01
28.0	6.263E-01	3.824E+00	9.526E+00	3.039E+01
30.0	4.552E-01	2.752E+00	5.066E+00	1.627E+01
35.0	2.024E-01	1.192E+00	1.050E+00	3.508E+00
40.0	9.249E-01	4.903E-01	2.340E-01	7.894E-01
45.0	4.448E-02	1.624E-01	5.751E-02	1.606E-01
50.0	2.285E-02	0.000E+00	1.560E-02	0.000E+00

Table 15. Water Vapor Absorption Parameters For The Spring-Summer Model Atmosphere

ALTITUDE KM	WATER VAPOR DENSITY PR-CM/KM	WATER VAPOR DEPTH PR-CM	PRESSURE * WATER VAPOR DENSITY MB PR-CM/KM	PRESSURE * WATER VAPOR DEPTH MB PR-CM
0.0	1.387E+00	2.845E+00	1.406E+03	2.354E+03
1.0	9.213E-01	1.707E+00	8.312E+02	1.260E+03
1.5	6.340E-01	1.323E+00	5.393E+02	9.231E+02
2.0	5.845E-01	1.018E+00	4.685E+02	6.715E+02
3.0	3.269E-01	5.750E-01	2.323E+02	3.349E+02
4.0	1.882E-01	3.238E-01	1.182E+02	1.660E+02
5.0	9.906E-02	1.849E-01	5.484E+01	8.350E+01
6.0	6.043E-02	1.068E-01	2.940E+01	4.269E+01
7.0	3.665E-02	5.922E-02	1.563E+01	2.089E+01
8.0	2.080E-02	3.123E-02	7.747E+00	9.662E+00
9.0	1.189E-02	1.530E-02	3.851E+00	4.088E+00
10.0	6.340E-03	6.476E-03	1.781E+00	1.403E+00
12.0	5.944E-04	1.622E-03	1.240E-01	1.597E-01
14.0	9.906E-05	1.069E-03	1.511E-02	5.623E-02
16.0	6.340E-05	9.089E-04	7.056E-03	3.508E-02
18.0	4.953E-05	7.965E-04	4.022E-03	2.428E-02
20.0	4.458E-05	7.025E-04	2.651E-03	1.770E-02
22.0	5.052E-05	6.075E-04	2.208E-03	1.286E-02
24.0	5.944E-05	4.978E-04	1.916E-03	8.742E-03
26.0	6.835E-05	3.703E-04	1.630E-03	5.204E-03
28.0	5.448E-05	2.479E-04	9.649E-04	2.667E-03
30.0	3.566E-05	1.591E-04	4.714E-04	1.289E-03
35.0	1.124E-05	5.335E-05	7.335E-05	2.192E-04
40.0	4.260E-06	1.738E-05	1.418E-05	3.920E-05
45.0	1.352E-06	4.708E-06	2.335E-06	6.358E-06
50.0	6.241E-07	0.000E+00	5.937E-07	0.000E+00

Table 16. Water Vapor Absorption Parameters for the Fall-Winter Model Atmosphere.

ALTITUDE KM	WATER VAPOR DENSITY PR-CM/KM	WATER VAPOR DEPTH PR-CM	PRESSURE * WATER VAPOR DENSITY MB PR-CM	PRESSURE * WATER VAPOR DEPTH MB PR-CM
0.0	3.467E-01	8.498E-01	1.530E+02	6.845E+02
1.0	2.476E-01	5.554E-01	2.222E+02	4.019E+02
1.5	2.179E-01	4.392E-01	1.835E+02	3.008E+02
2.0	1.783E-01	3.404E-01	1.403E+02	2.201E+02
3.0	1.189E-01	1.939E-01	8.247E+01	1.111E+02
4.0	6.538E-02	1.044E-01	3.976E+01	5.255E+01
5.0	3.764E-02	5.414E-02	2.000E+01	2.480E+01
6.0	2.080E-02	2.574E-02	9.625E+00	9.612E+00
7.0	8.420E-03	1.205E-02	3.382E+00	3.643E+00
8.0	3.467E-03	6.469E-03	1.204E+00	1.534E+00
9.0	1.585E-03	4.065E-03	4.744E-01	7.508E-01
10.0	7.429E-04	2.953E-03	1.908E-01	4.395E-01
12.0	5.944E-04	1.622E-03	1.119E-01	1.438E-01
14.0	9.906E-05	a.069E-03	1.365E-02	5.042E-02
16.0	6.340E-05	9.089E-04	6.391E-03	3.129E-02
18.0	4.953E-05	7.965E-04	3.644E-03	2.151E-02
20.0	4.458E-05	7.025E-04	2.392E-03	1.557E-02
22.0	5.052E-05	6.075E-04	1.978E-03	1.121E-02
24.0	5.944E-05	4.978E-04	1.697E-03	7.540E-03
26.0	6.835E-05	3.703E-04	1.424E-03	4.426E-03
28.0	5.448E-05	2.479E-04	8.287E-04	2.226E-03
30.0	3.556E-05	1.591E-04	3.969E-04	1.053E-03
35.0	1.124E-05	5.335E-05	5.833E-05	1.708E-04
40.0	4.260E-06	1.738E-05	1.078E-05	2.950E-05
45.0	1.352E-06	4.708E-06	1.748E-06	4.683E-06
50.0	6.241E-07	0.000E+00	4.261E-07	0.000E+00

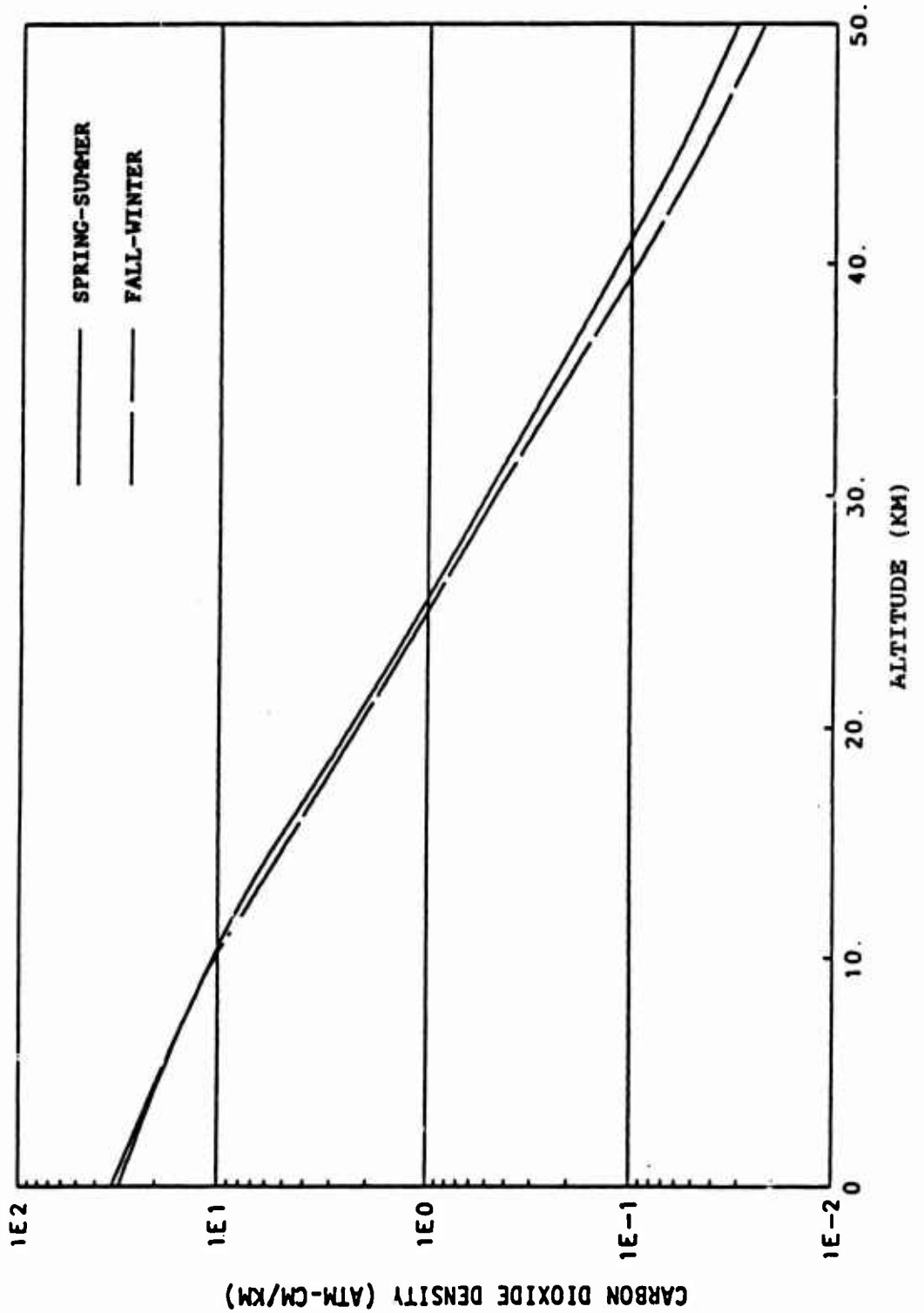

Figure 29. Comparison of Carbon Dioxide Density for the Two Model Atmosphere.

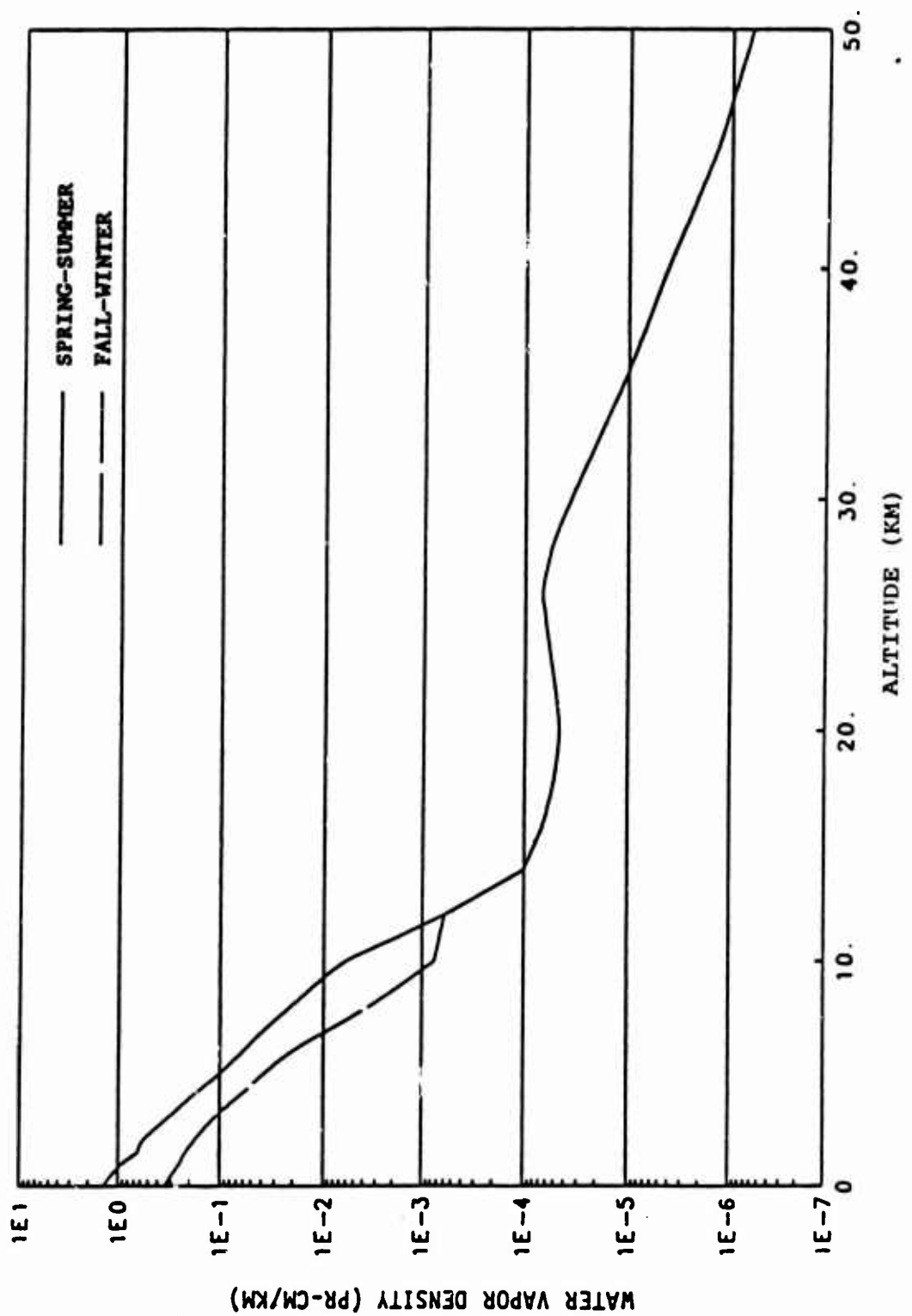

Figure 30. Comparison of Water Vapor Density for the Two Model Atmosphere.

be seen in Figure 45. In these cases, KSC used two procedures. In the first case, there were no clouds above 1.5 km in the calculation, and in the second case, KSC used cloud cover at 3 km. The effect this had on predicted thermal energy at a given location can be seen in Figures 46 thru 49.

3.4 KSC TRANSMISSION TECHNIQUES.

The TAXV code was developed at KSC to calculate thermal environments for specific cases of interest using the Monte Carlo data base. The code reads in a specific burst altitude and receiver altitudes and ranges of interest along with the albedo surface specification and the surface visibility and water vapor density. The code then computes the irradiance at each of the receiver points as discussed previously and finds the exposure by integrating over time.

The transmission factor given previously in the expression for the irradiance is given by the product of the direct transmission and a scattering buildup

$$T = T_D * B_s = \exp(-R^* \left| \tau_e(\lambda, H_s) - \tau_e(\lambda, H_r) \right| / \left| H_s - H_r \right|) * T_{IR} * B_s \qquad (31)$$

where the exponential factor represents the attenuation due to aerosol and molecular scattering and ozone absorption, T_{IR} refers to the molecular absorption in the IR portion of the spectrum, and B_S represents the buildup due to multiple scattering in the atmosphere. The quantity τ_e is an optical depth defined by

$$\tau_e(\lambda, H_s) = \int_{H_s}^{50} \sigma_e(\lambda, H)\, dH \qquad (32)$$

where σ_e is the extinction cross section (km^{-1}) given by

$$\sigma_e(\lambda,H) = \sigma_a(\lambda,H) + \sigma_R(\lambda,H) + \sigma_{oz}(\lambda,H) \quad (33)$$

All quantities are dependent upon wavelength and altitude with σ_a, σ_R and σ_{oz} being the aerosol, Rayleigh and ozone cross sections respectively. Ozone is a molecular absorber and the details of the cross section will be given in a later section. The ozone absorption varies exponentially with ozone concentration so for convenience it is combined with the scattering cross sections in defining the model atmosphere parameters. If $H_s = H_r$, then the above exponential expression is replaced by

$$\exp(-R^* \sigma_e(\lambda,h_s)). \quad (34)$$

The previous two sections describe how the direct flux attenuation is computed including the effects of the scattering interactions and the gaseous absorption. The photons scattered from the main beam can undergo multiple scattering interactions with the aerosol and molecular constituents of the atmosphere and can contribute to the total irradiance at the receiver. Various techniques and expressions (Reference 11) have been defined in the past to represent this scattered buildup. The techniques based upon experimental measurements in general are not reliable when extrapolated beyond the range of the original experimental conditions.

The most reliable scattered flux predictions are obtained from Monte Carlo Transport calculations (References 11 and 14). Given a particular meteorological range and humidity on the ground surface then the scattered flux environment can be determined as a function of receiver range, altitude and orientation for a particular source wavelength and altitude. These types of runs are very expensive and time consuming and cannot be used directly for general environment predictions. Instead, the data from such runs must be processed and converted to a form permitting fast accurate environment predictions.

The buildup factor approach has proven to be the best approach for this type of prediction and has been used in many previous transmission predictive techniques. The buildup typi-

cally has been derived from elementary transport theory or experimental measurements such as used in the UK approach. The current procedure temporarily uses buildup factors taken from the RECIPE transmission routines which were derived to match the Monte Carlo data bases available. The buildup factors can be defined with the source wavelength and altitude, the receiver range, altitude and orientation and the model atmosphere variables as parameters.

Previous studies (Reference 11) have shown that marked simplification occurs if the buildup factors are expressed as a function of the scattering optical depth (SOD) from the source to the receiver. If $H_s \neq H_r$,

$$SOD = (\sigma_A(\lambda, H_s) + \sigma_R(\lambda, H_s)) * R, \quad (35)$$

and, if $H_s = H_r$

$$SOD = R * |(\tau_A(\lambda, H_s) - \tau_A(\lambda, H_r) + \tau_R(\lambda, H_r) - \tau_R(\lambda, H_r)| H_s - H_r| \quad (36)$$

where all variables have been previously defined. In earlier work buildup factors as a function of SOD defined above were compared with the source altitude, receiver altitude, wavelength, and various meteorological variables parameters. It was found that the wavelength dependence is the primary parameter of importance in representing the transport results. The source and receiver altitudes were relatively unimportant.

The wavelength dependence in the current model is shown in Figure 31 for wavelengths from .32 to 3.8. There is seen to be a smooth transition in the buildup to smaller values as the wavelength is increased. This transition follows that noted in the Monte Carlo data. This type of variation is expected considering the wavelength dependence of the scattering functions shown in Table 12.

The scattered flux does not show this smooth variation with wavelength in the IR region because of the extreme wavelength

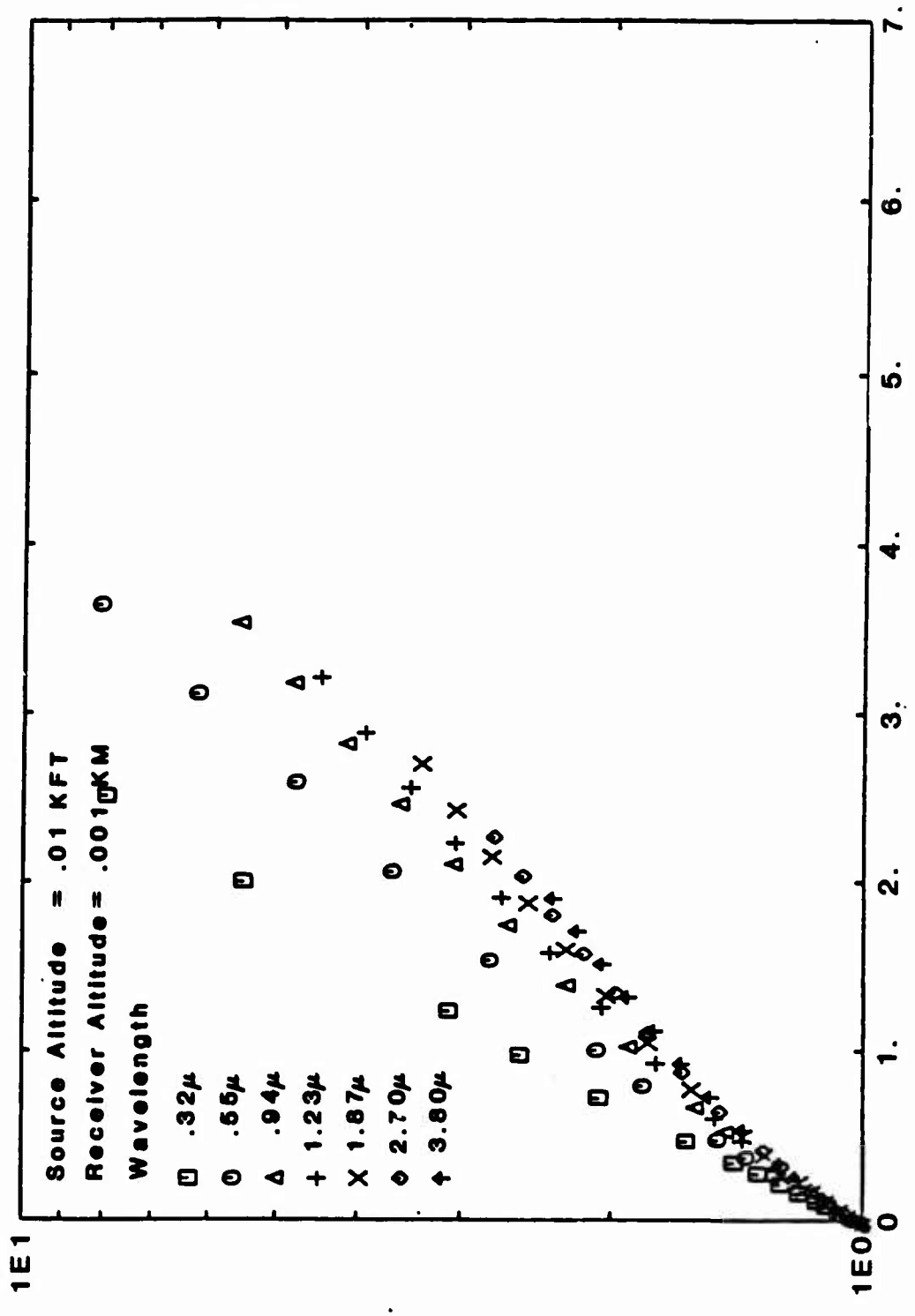

Figure 31. Comparison of Scattering Build-up Factors for Various Wavelengths.

dependence of the gaseous absorption. Since the buildup factor comes from the ratio of the total to direct flux, it displays the characteristics of the scattering and not the absorption interactions.

The curves in Figure 31 were obtained from the expressions used in the updated TAXV. They were taken from the RECIPE code which defines the buildup factor as follows:

$H_r < 49$ km

$$B_\lambda (\tau_s) = 1.3 * \exp(\Delta \tau_s)/z \quad (37)$$

where

$$\tau_s = \tau_A + \tau_R \quad (38)$$

$$z = 1 + .3 \exp(-2 \tau_s) \quad (39)$$

and

$$\Delta = \alpha \exp(-\upsilon V) \quad (40)$$

where V is the visual range (meteorological range). The variable is a function of the field of view (FOV) given by

$$\upsilon = 2.96 \exp(-2\ \mathrm{FOV}) + .055 \exp(-.05\ \mathrm{FOV}) \quad (41)$$

and α is a function of wavelength (μ) given by

$$\alpha = .38\lambda^{-.145} + .025\lambda^{-2.08}. \quad (42)$$

$H_r > 49$ km

$$B_\lambda (\tau_s) = B \exp(\Delta \tau_s) \quad (43)$$

where

$$\Delta = \frac{(.4 + .1 + 2.29\ V^{-.65} - 1)}{\lambda(1.08 + .00127\ V^{2.1})} \quad (44)$$

and

$$B = 1 + 8\ (.15/\lambda)^{1.86} \exp(.00926V) \quad (45)$$

It is assumed that the orientation dependence of the scattered flux is the same as the direct flux. This is reasonable because the scattering is strongly forward peaked resulting in a narrow angular distribution about the source to receiver direction.

3.5 KSC PROBABILISTIC TRANSMISSION METHOD.

A method has been developed to compute probabilistic transmission factors and exposures using the KSC thermal atmospheric transmission and source output models described in the preceding sections. This methodology is detailed in Figure 32. As discussed previously, the first step in the procedure is a careful analysis of the weather at the region of interest. The data base containing the build up factors and the model atmospheres stored in TAXV must be compatible with the altitude dependent atmospheric parameters for the region of interest. The current models as discussed previously are applicable to mid-latitude temporate regions with a fall-winter or spring-summer seasonal choice. Other regions such as the tropic, mideast desert, or arctic regions will require additional modelling of atmospheres for these regions. Necessary information is available in the literature and in fact considerable experience for the arctic and tropic regions has been obtained in previous studies. When the data base is expressed as buildup factors as a function of scattering optical depth relatively small variations will be noted for the various atmosphere models. Storing the data as scattered flux as a function of the geometrical variables as is done in QRT, results in a data base with greater variation between model types and with no well defined technique for interpolating results between models.

The weather analysis required in the KSC approach involves defining a set of cases involving relevant atmospheric parameters each of which represents an equal occurrence probability.

Typically the parameters of most importance are the visibility (or meteorological range) and the albedo surface characteristics including ground elevation and albedo and cloud ceiling altitude and coverage. For some conditions it may be necessary to include additional parameters such as the water vapor density. These parameters can be described in any desired detail as monthly seasonal or annual averages.

The approach used in the UK analysis was to consider cloud ceiling altitude and visibility as parameters. The details of the UK analysis were discussed in Section 2. Basically, the probability of occurrence of visibility was given for three different ceiling altitudes. For the demonstration calculations and comparisons, 20 different sets of weather conditions were defined each of which represents an occurrence probability of 5%. These 20 different cases are shown in Table 16.

A serious problem with the UK analysis was their equating a high altitude ceiling with no cloud cover. These imply completely different transmission probabilities as will be shown in the following discussion and led to the definition of the two alternate sets in Table 16.

There is a certain range of visibilities associated with each condition. The maximum visibility for each condition is used to identify the case. Thus this gives the upper limit to the transmission associated with the range of visibilities for that case. This is the proper approach for USANCA applications when sure safe type environments are being developed. The i and j indices are merged into the 1 index.

The next step as indicated in Figure 32 is to compute the transmission as a function of range for each of the 20 sets of conditions. This is straightforward and involves running the TAXV code for each case and storing the transmission factor as a

WEATHER ANALYSIS

DEFINE PROBABILITY vs. VISIBILITY

CLOUD LAYERS DEPEND ON REGION

MONTHLY, SEASONAL, ANNUAL

IDENTIFY $\Delta P_{ij} = \int_{V_{i-1}}^{V_i} \left(\frac{dP}{dV}\right) dv$ VS V_i

i LABELS VISIBILITY

j LABELS CLOUD LAYER/GROUND ALBEDO CONDITIONS

CHOOSE Vi TO GET EQUAL ΔP_{ij}

TRANSMISSION CALCULATIONS

CALCULATE T_{ijk} vs. R_k USING TAXV

EACH T_{ijk} HAS ASSOCIATED ΔP_{ij}

DETERMINE T vs PROBABILITY OF OCCURRENCE

REORDER $T_{ijk} = T_{lk}$ AND $\Delta P_{ij} = \Delta P_l$ FOR EACH k

MONOTONICALLY INCREASING $T_{l-1} \leq T_l$

DEVELOP $P_l = \sum_{m=1}^{l} P_l$ vs. T_{lk} FOR EACH k

GENERATE T_{lk} vs. R_k CURVES FOR DESIRED P_l

TRANSMISSION CURVES DIRECTLY REPRESENT OCCURRENCE PROBABILITY

Figure 32. KSC Probabilistic Transmission Method.

function of the range. One then has a matrix of transmissions as shown in Table 17 for the 20 different cases (1 index) and ranges (R_k). This table represents the case where clouds were assumed to exist at 3km for group III conditions. As expected the transmission in general increases as the visibility increases within each albedo group at a particular range. A priori one cannot predict the relative transmissions for different groups because the enhancement factor from the albedo surfaces depends upon both cloud, source, and receiver altitudes and the range in a complicated fashion. In general, as indicated previously for higher ceilings, the maximum enhancement occurs at larger ranges.

These results are plotted in Figure 33 where the symbols A through J represent cases 1 through 20, respectively, and in Figure 34 where the data points are connected by straight lines. Recall that each case represents a 5% occurrence probability.

The next step as noted in Figure 32 is to reorder the 1 index independently at each R_k in order of increasing transmission. This results in Figure 35 where now the symbols are associated with the reordered 1 index at each R_k and represent increasing (or equal) transmissions. Since each case represents an occurrence probability of 5%, the reordered 1 index at each R_k and each symbol also represents an integrated probability from .05 to 1 in steps of .05. The data are shown as continuous curves in Figure 36 where finally the cumulative occurrence probability transmission factors are displayed. As indicated previously, the set of conditions corresponded to the choice of a cloud ceiling at 3km altitude, choosing no cloud at that altitude (an equivalent condition in the UK weather analysis) results in a much lower transmission as will be noted in the comparisons given in the next section.

Table 17. Equiprobable Sets of Meteorological Data (5% Δ P).

L	J	I	CLOUD-BASE VISIBILITY ALTITUDE RANGE (KM)	
1	1	1	0 - .3KM	0 - 0.5
2	1	2	0 - .3KM	0.5 - 1
3	1	3	0 - .3KM	1 - 1.55
4	1	4	0 - .3KM	1.55 - 2
5	1	5	0 - .3KM	2 - 2.75
6	1	6	0 - .3KM	2.75 - 3.75
7	1	7	0 - .3KM	3.75 - 6.0
8	1	8	0 - .3KM	6.0 - 50.0
9	2	1	.3 - 1.5KM	0 - 3.25
10	2	2	.3 - 1.5KM	3.25 - 5.0
11	2	3	.3 - 1.5KM	5.0 - 7.0
12	2	4	.3 - 1.5KM	7.0 - 10.0
13	2	5	.3 - 1.5KM	10.0 - 16.0
14	2	6	.3 - 1.5KM	16.0 - 50.0
15	2	7	>1.5KM	0 - 3.0
16	2	8	CLOUD	3.0 - 5.0
17	3	1	BASE	5.0 - 7.5
18	3	3	OR < .5	7.5 - 11.0
19	3	3	CLOUD	11.0 - 18.0
20	3	4	COVER	18.0 - 50.0

Table 18. Transmission vs. Range and Case, Cookes Weather Data, KSC Transmission, Clouds at 3.0KM (Group III).

Group No.	Case No.	RANGE (KM) 0.	.25	.5	1.	1.5	2.	3.	4.	5.	7.5	10.	12.5	15.	17.5	20.
I	1	1.0	.85	.7	.475	.3	.206	.113	.056	.025	.006	.002	0.	0.	0.	0.
	2	1.0	.85	.7	.475	.3	.206	.113	.056	.025	.006	.002	0.	0.	0.	0.
	3	1.0	.90	.8	.644	.5	.375	.206	.125	.075	.025	.0125	0.	0.	0.	0.
	4	1.0	.95	.875	.750	.620	.500	.300	.188	.125	.050	.022	.0125	.006	0.	0.
	5	1.0	.963	.906	.806	.7	.613	.438	.288	.194	.10	.05	.025	.0125	.01	0.
	6	1.0	1.125	1.188	1.175	1.0	.863	.6	.425	.3	.15	.088	.05	.028	.013	.01
	7	1.0	1.2	1.3	1.319	1.275	1.113	.875	.688	.525	.276	.168	.094	.075	.05	.03
	8	1.0	1.35	1.46	1.563	1.73	1.638	1.575	1.425	1.281	1.05	.863	.722	.6	.488	.394
II	9	1.0	.95	.9	.8185	.7375	.656	.513	.4	.313	.194	.119	.070	.044	.025	.017
	10	1.0	.994	.988	.956	.913	.863	.75	.638	.544	.344	.288	.163	.113	.08	.05
	11	1.0	1.012	1.019	1.025	1.024	1.006	.95	.869	.781	.538	.363	.263	.2	.15	.113
	12	1.0	1.036	1.063	1.094	1.113	1.125	1.113	1.075	1.0	.769	.563	.410	.3	.225	.175
	13	1.0	1.05	1.09	1.175	1.22	1.25	1.288	1.29	1.26	1.088	.888	.70	.556	.438	.338
	14	1.0	1.05	1.10	1.2	1.288	1.375	1.510	1.613	1.66	1.650	1.550	1.413	1.275	1.125	1.0
III	15	1.0	.90	.813	.688	.60	.525	.40	.313	.250	.175	.119	.075	.05	.025	.0185
	16	1.0	.925	.875	.813	.762	.725	.65	.575	.488	.350	.269	.210	.163	.122	.088
	17	1.0	.956	.925	.875	.869	.856	.825	.775	.738	.613	.469	.370	.30	.250	.210
	18	1.0	.969	.950	.926	.938	.950	.969	.964	.938	.85	.725	.588	.475	.378	.313
	19	1.0	.980	.963	.975	1.0	1.038	1.10	1.15	1.175	1.188	1.125	1.013	.881	.756	.638
	20	1.0	.988	.981	1.0	1.063	1.131	1.256	1.375	1.50	1.688	1.80	1.81	1.788	1.725	1.644

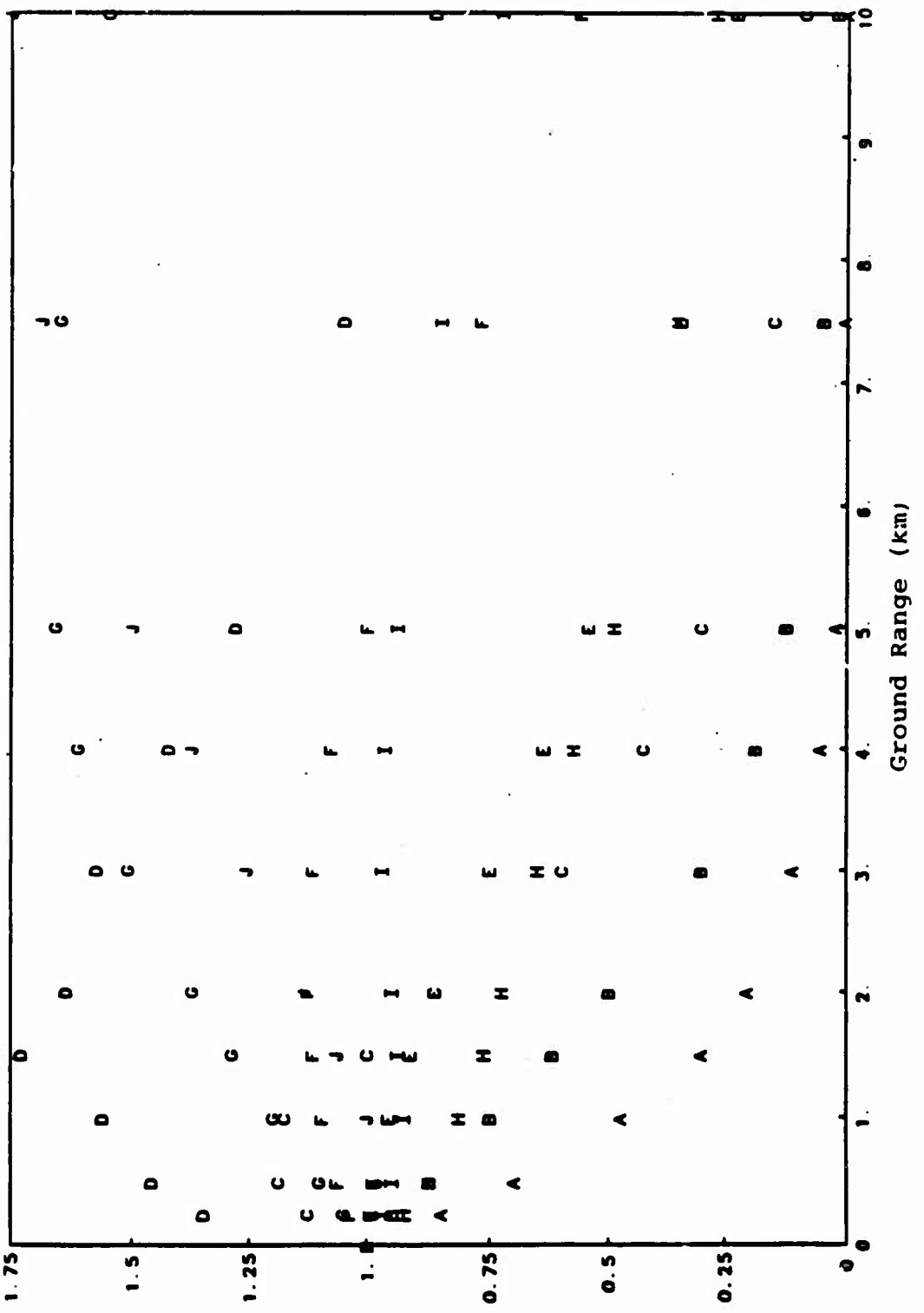

Figure 33. Sample Case. Data Identified by Weather Conditions.

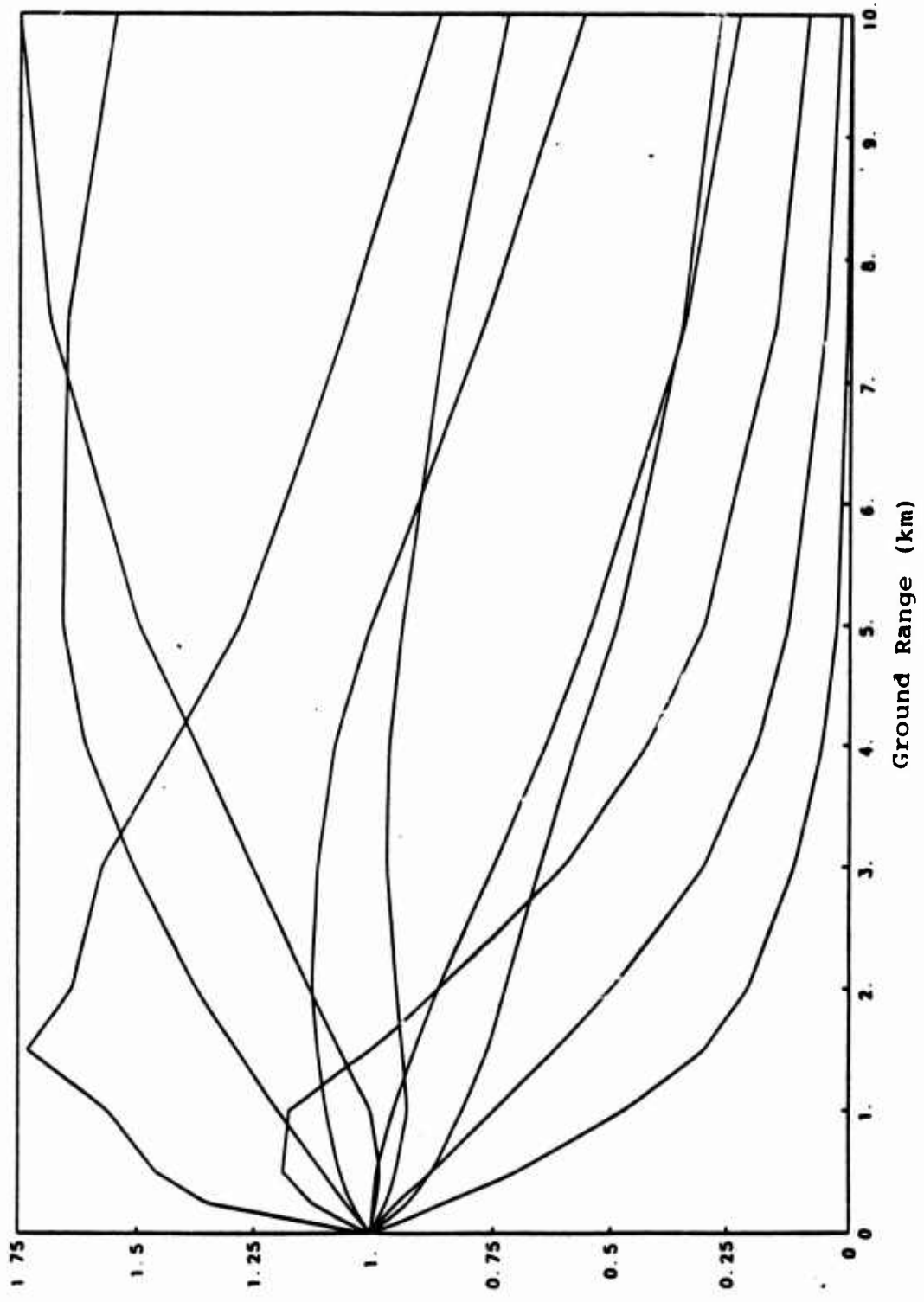

Figure 34. Sample Case. Transmission Curves for Weather Conditions.

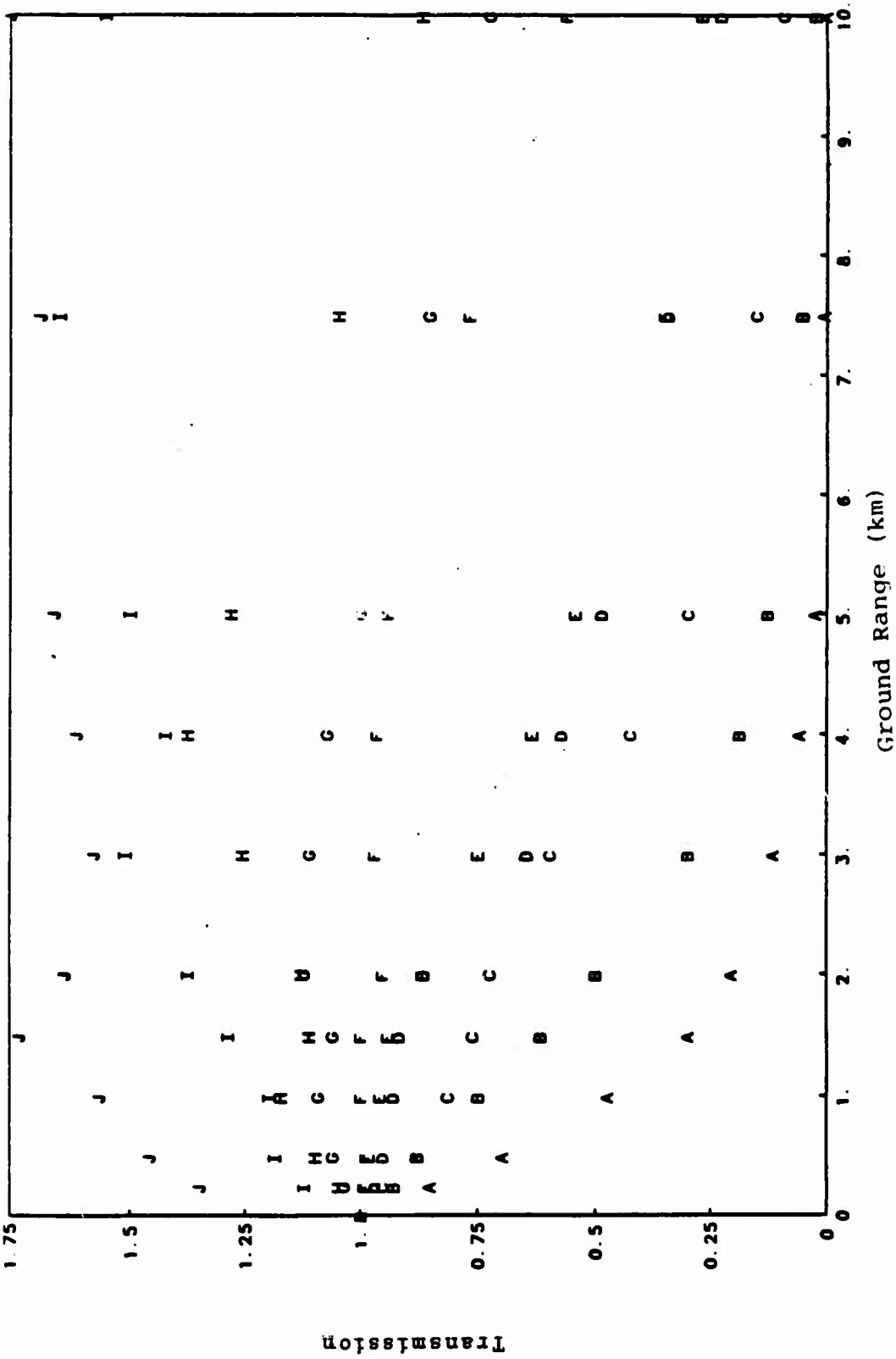

Figure 35. Sample Case. Data Identified by Cumulative Occurrence Probability.

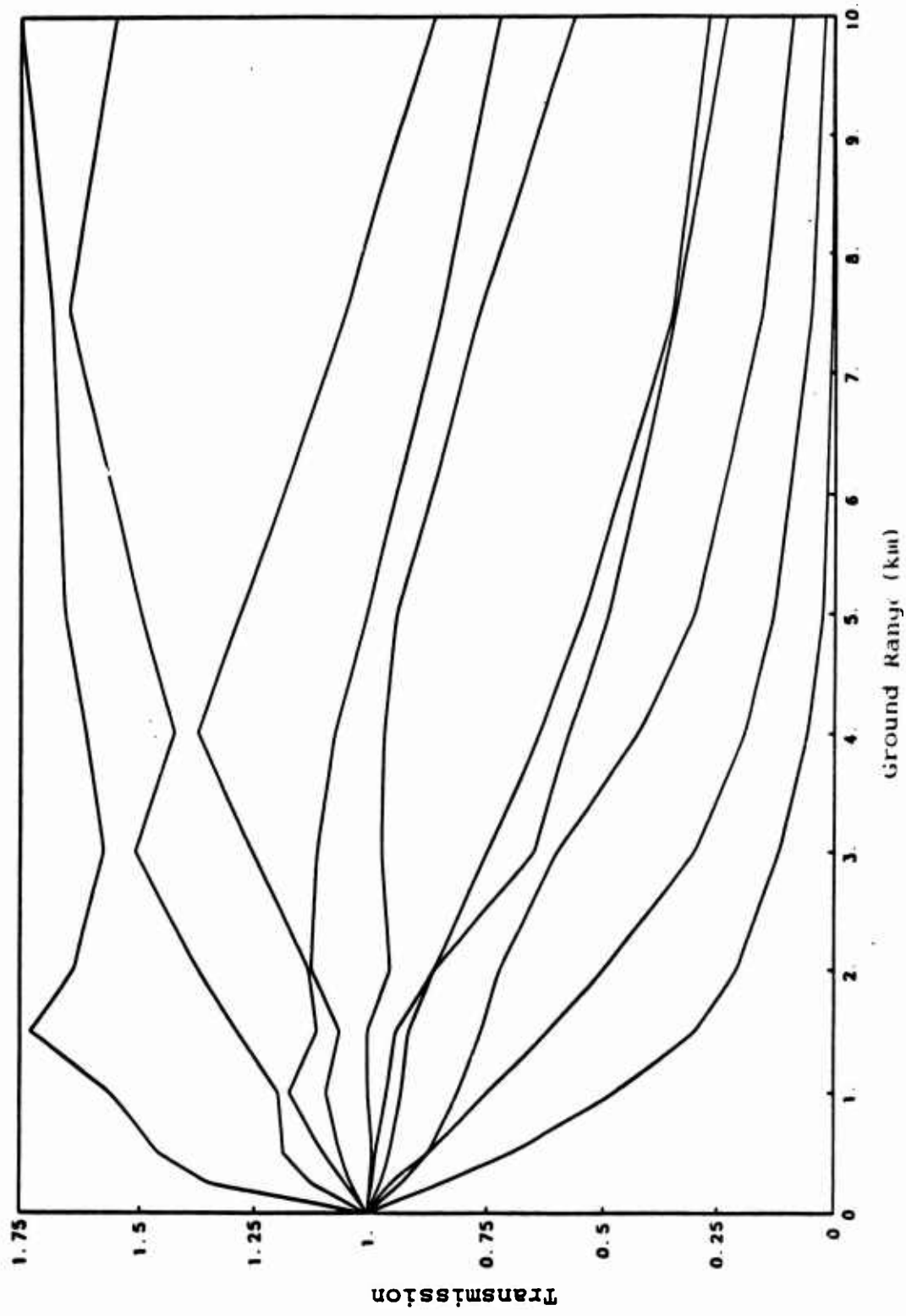

Figure 36. Sample Case. Transmission Curves for Cumulative Occurrence Probability.

SECTION 4

COMPARISONS OF KSC AND UK RESULTS

In this section comparisons of KSC and UK results are presented. Early in the study it was recognized that the UK method disagreed with KSC transmission results. The UK method could not be recommended for general USANCA purposes because crucial parameters of importance were not included. However, the bulk of the KSC data base was developed prior to a redefinition of atmospheric models as discussed in subsection 3.2. A more recent data base developed for the QRT code was based on later model atmospheres but needs considerable extension and manipulation before it can be used for general thermal predictions as will be discussed in Section 5.

The approach used in the current study was to generate transmission factors relevant to the UK weather analysis and pinpoint the important parameters. As noted in the last section an example calculation was completed and probabilistic transmissions were calculated.

Early in this study a series of runs were made with TAXV using parameters obtained from the UK analysis. The code at that time was structured with a table of buildup and enhancement factors. The various parameters varied in the runs are noted in Table 4.1 and were chosen to indicate the relative importance of the parameters for USANCA thermal predictions.

Two different yields and source spectra were chosen to show the effect of spectra on the transmission calculations. Figures 37 and 38 show the effect, respectively, of yield and surface interaction spectral changes on the transmission for a surface burst with a ground albedo with nominal dirt values, a cloud

Table 19. Transmission Run Parameters.

YIELDS: 10KT, 100KT

GROUND ALBEDO: ZERO, DIRT, SNOW

CLOUD BASE ALTITUDES: NONE, .3, 1.5, 3.0 KM

SPECTRA: SURFACE, FREE AIR

SOURCE ALTITUDE: ZERO, 1KM

VISIBILITY: 25KM, 6.5KM

RECEIVER: FLAT PLATE ON GROUND FACING SOURCE

HUMIDITY: 1.5, 10G/M^3

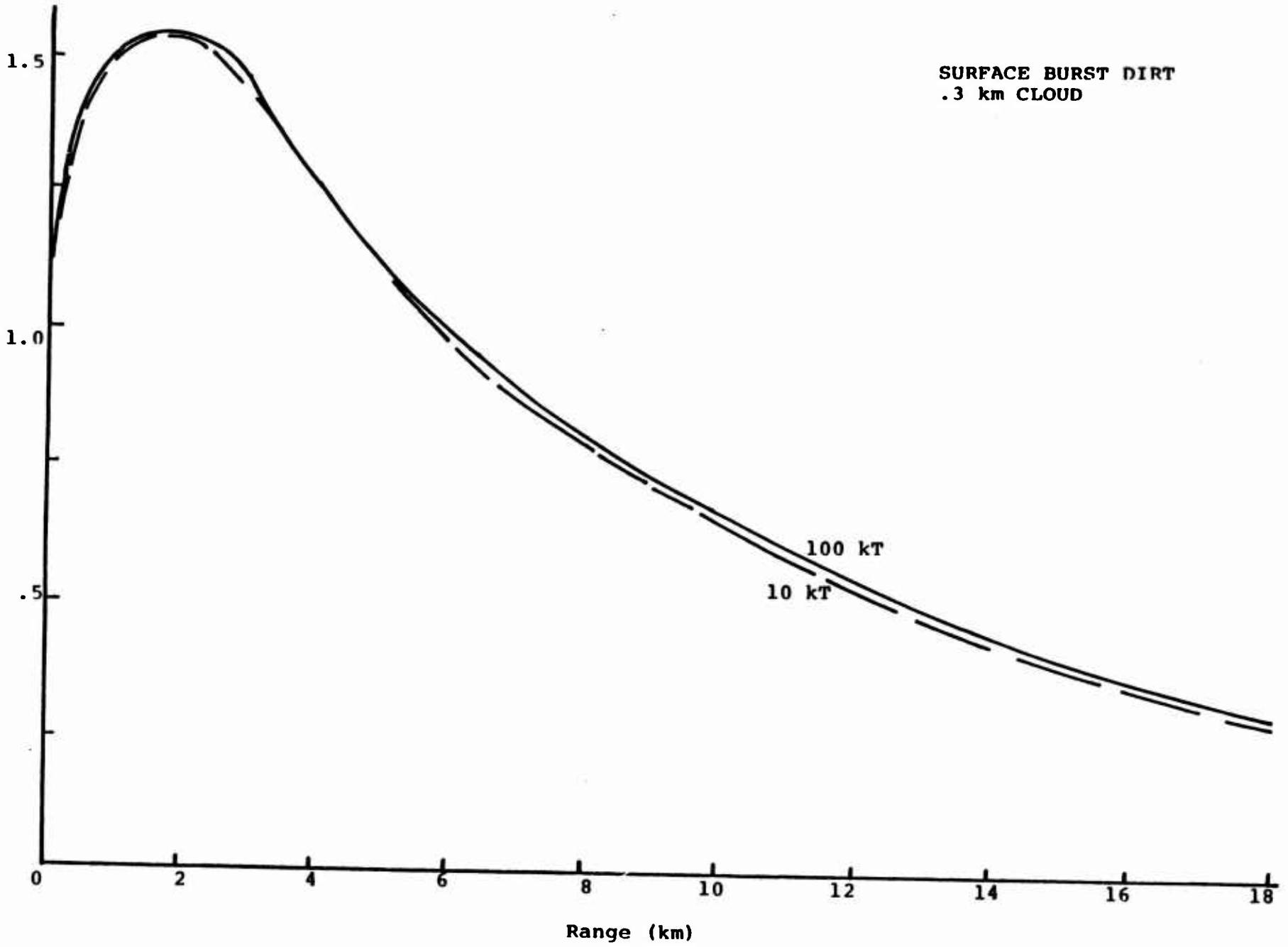

Figure 37. Effect of Yield on Transmission Predictions.

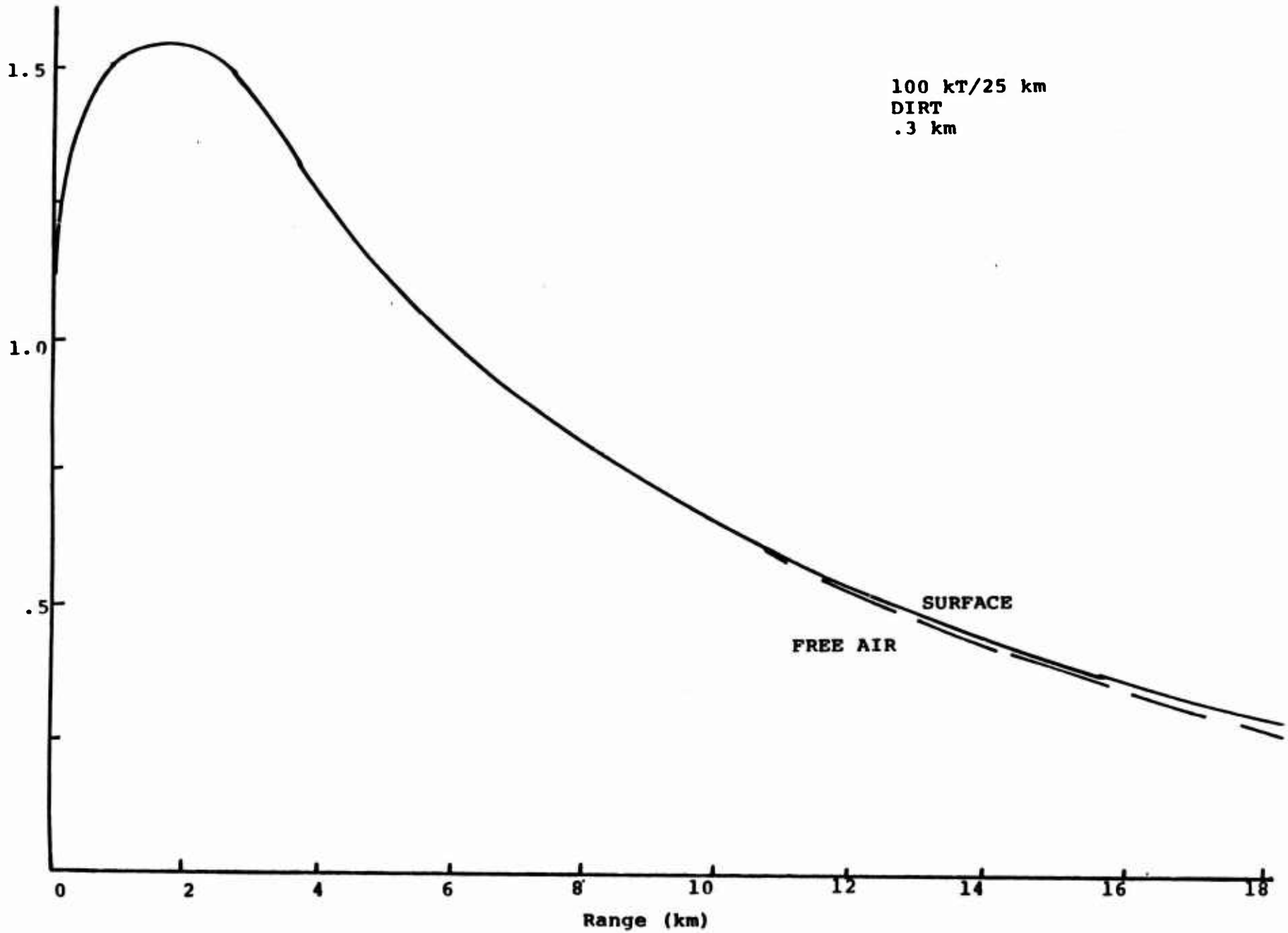

Figure 38. Effect of Spectrum Differences Caused by Surface Interactions on Transmission.

ceiling at .3 km and a visibility of 25 km. The differences are seen to be negligible in both cases. Figure 39 shows the effects of source altitude on the transmission. The transmission for the 1 km source altitude is much higher than for surface bursts. This effect is not allowed for in the UK method and their transmission corresponds in general to surface bursts and receiver altitudes. Neglect of this dependence can seriously underpredict the thermal exposure.

Figures 40 through 43 show the effects of the albedo surfaces on the transmission for various conditions. In Figure 40, the transmission factors for ceiling altitudes of .3, 1.5 and 3 km are compared to the transmission with no cloud and with zero ground albedo assumed. A buildup is noted in each case over the no cloud case. The range at which the maximum buildup is noted increases as the cloud ceiling is raised. Note that at large ranges the transmission with a cloud ceiling becomes smaller than for the no cloud case.

Comparable results are shown in Figure 41 for a dirt ground surface albedo. The differences are much larger because of the "channeling" of thermal energy to much longer ranges because of the reflective surfaces. In Figure 42 the effect of the ground albedo is shown for the .3 km cloud ceiling. The albedo for the dirt surface corresponds to sandy soils.

In Figure 43, the combined effects of the albedo surfaces and burst altitudes are shown for dirt ground albedo and 25 km visibility. Again raising the burst altitude to 1 km results in a dramatic increase in the transmission factor.

The above examples all used a 25 km visibility. The effect of surface albedo for a 6.5 km visibility is noted in Figure 44 and should be compared with Figures 37-52 where comparable results are given for a 25 km visibility. The same general trends are noted but as expected the enhancement is less for the smaller visibility and the transmission is less at the longer ranges.

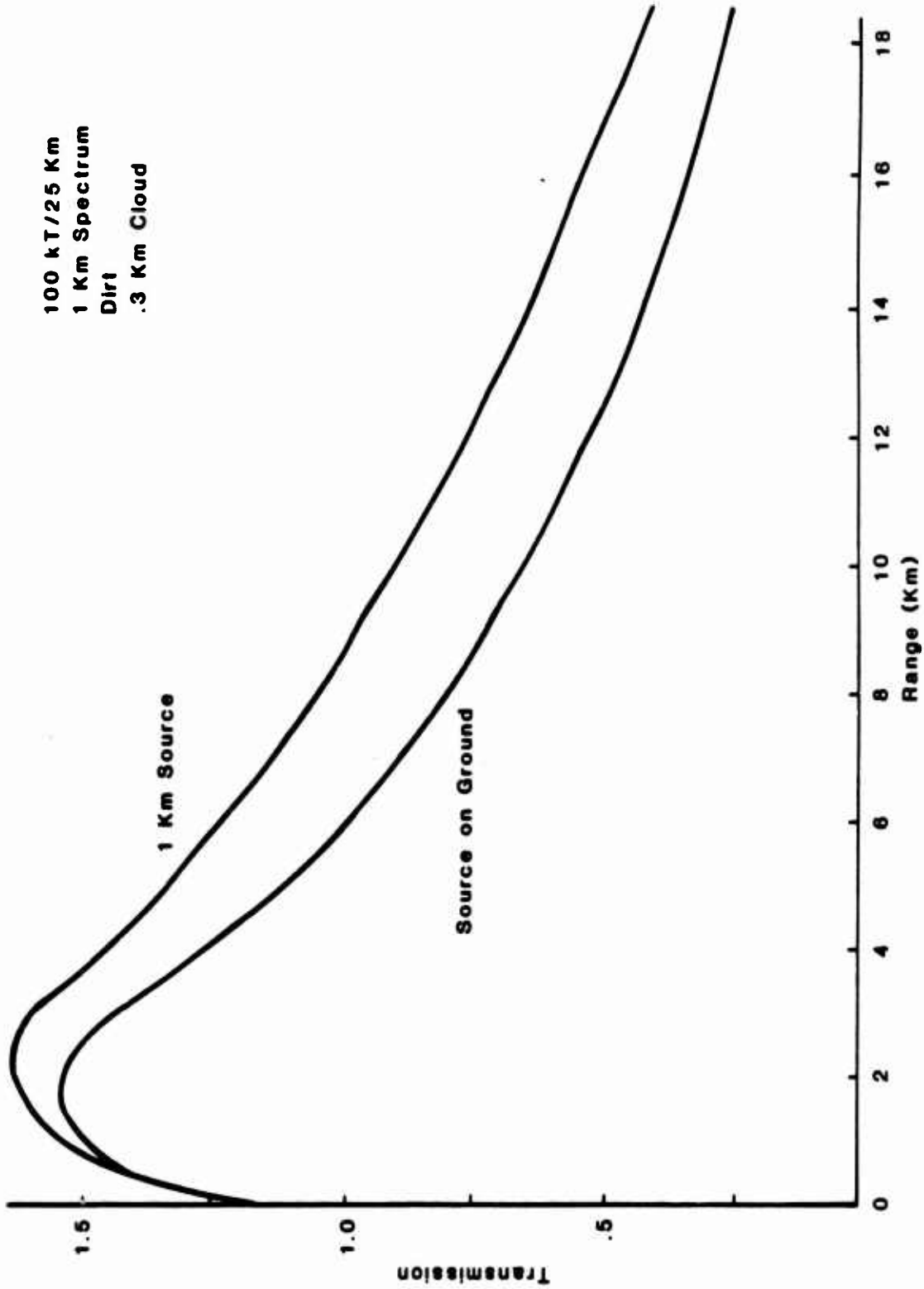

Figure 39. Effect of Source Altitude on Transmission Predictions.

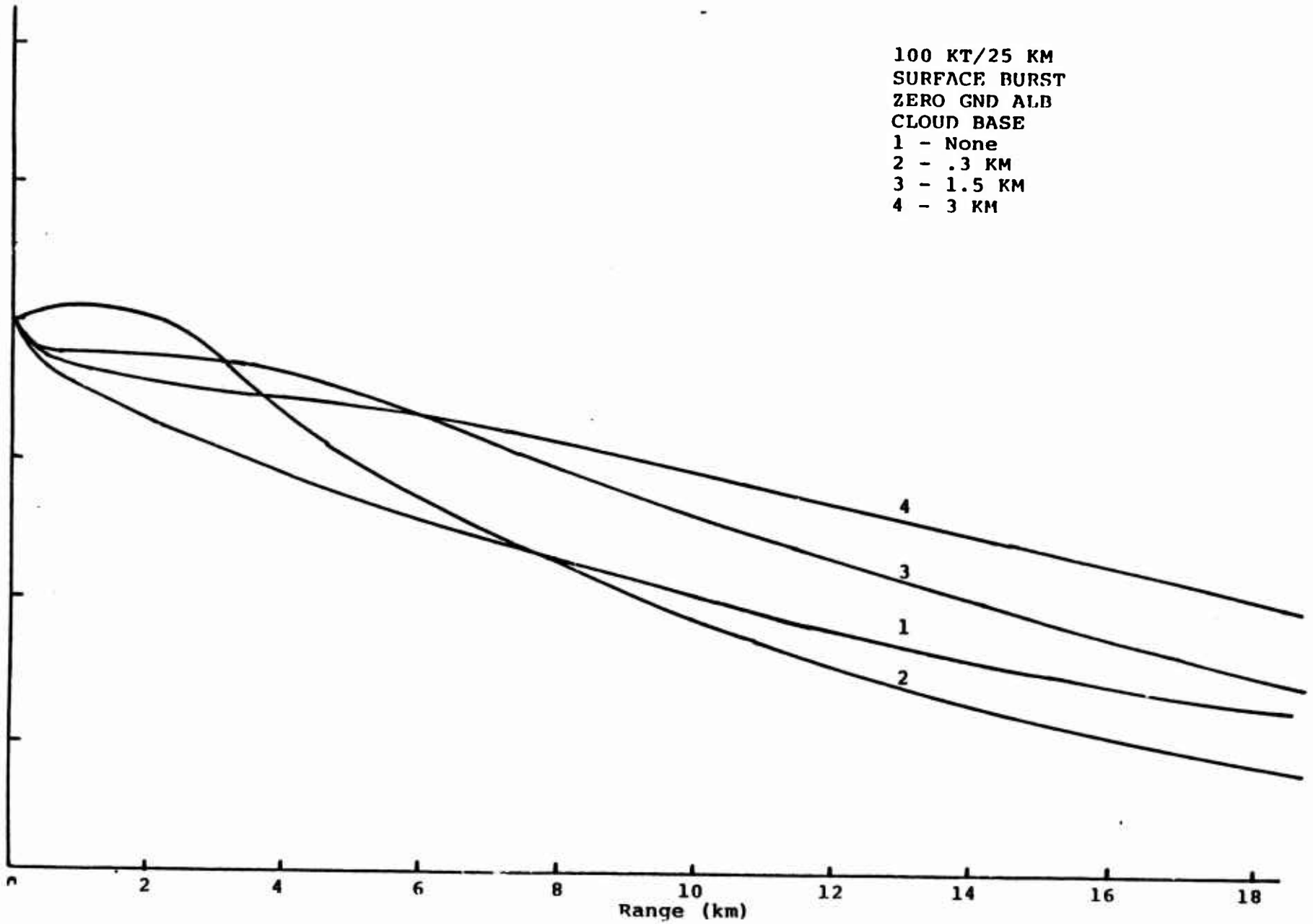

Figure 40. Effects of Cloud Ceiling Altitudes on the Transmission for Zero Ground Albedo.

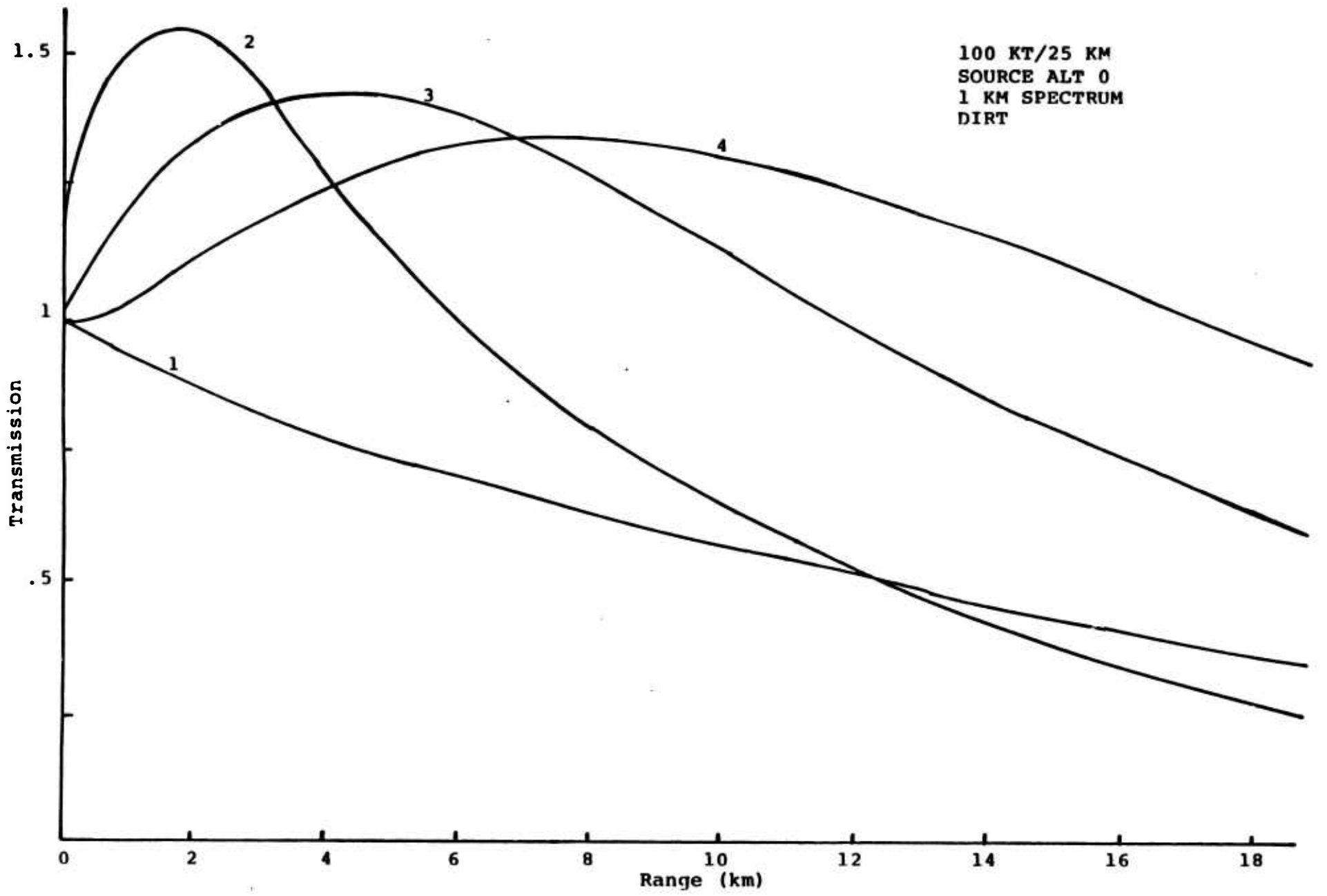

Figure 41. Effect of Cloud Ceiling Altitude on the Transmission for Dirt Ground Surface.

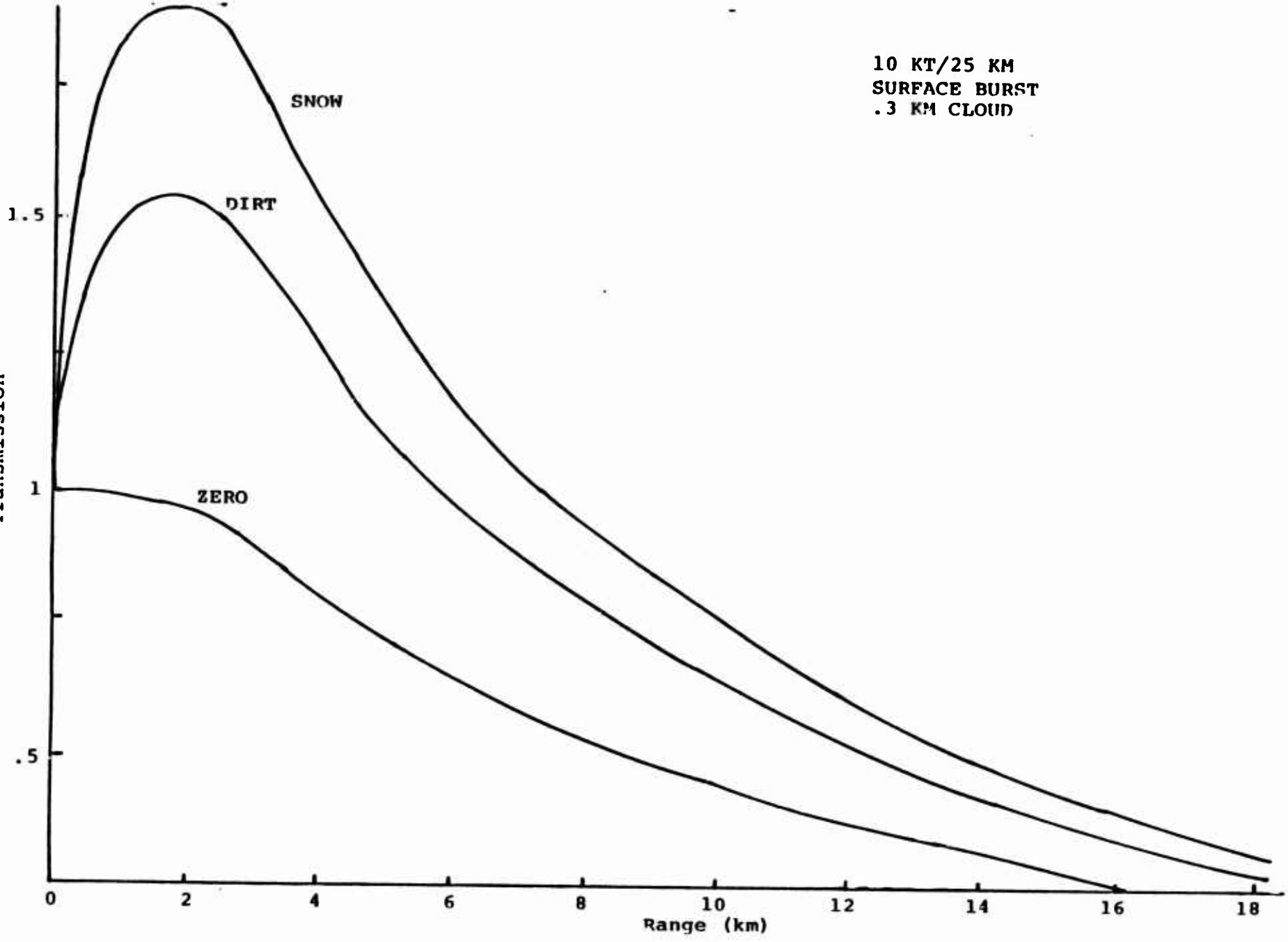

Figure 42. Effect of Ground Albedo on the Transmission.

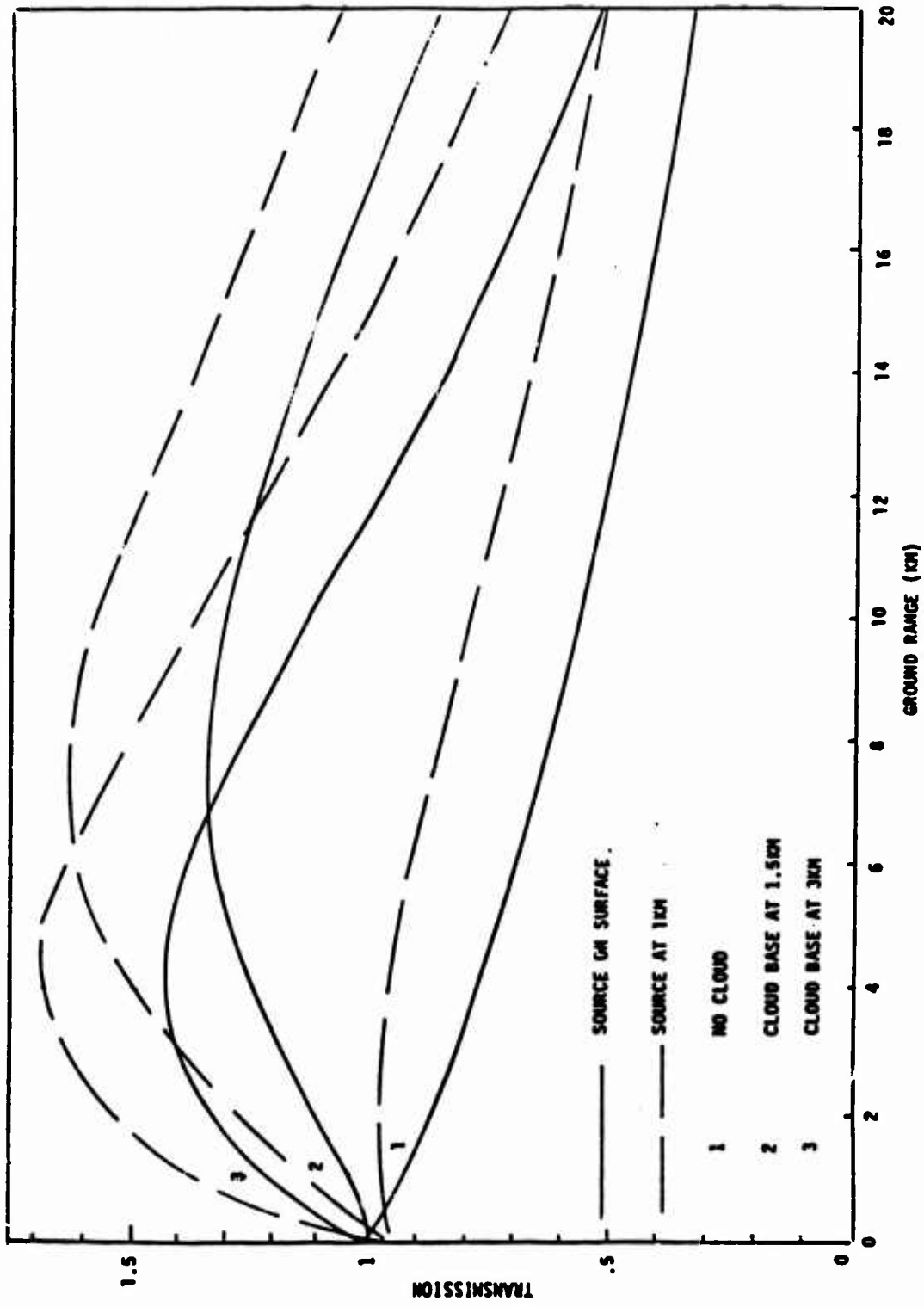

Figure 43. Effect of Burst Altitude on Transmission with Albedo Surfaces.

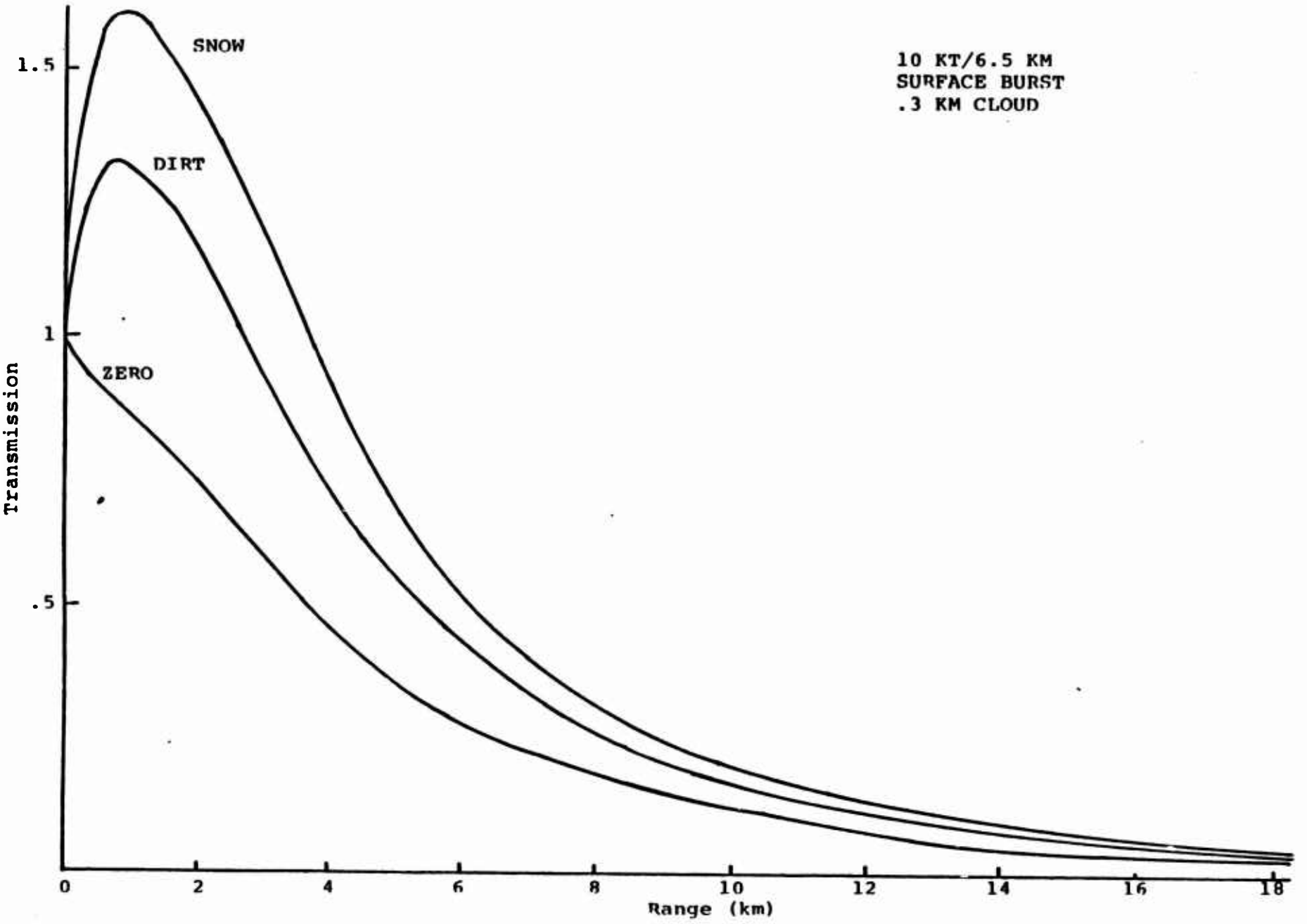

Figure 44. Effect of Surface Albedo for 6.5 km Visibility.

As discussed in the previous section a set of probabilistic transmission factors was developed using the UK weather analysis. The 95% and the 50% curves are compared in Figure 45. The solid lines represent the KSC analysis with no clouds above 1.5 km. The dashed lines refer to the KSC analysis assuming clouds at 3 km for the group 3 cloud ceiling condition discussed previously. As expected the cases with clouds have a much higher transmission than the cases without clouds. Shown also are the UK curves given by Cooke. The 95% curves are considerably different, whereas, the Cooke 50% curve is fairly close to the KSC curve without clouds out to ranges of about 8 km. The Cooke 95% curve does not appear to show the influence of more than one cloud layer because of the narrow range of ground ranges where albedo surface enhancement occurs. The Cooke 95% curve is seen to be larger than the KSC curve only for ranges of about 2 km and for ranges of 10 km and greater. The flattening out of the Cooke 95% and 50% curves beyond 5 km is not expected. The KSC curves with a cloud present a small percentage of the time show how crucial the difference between no cloud ceiling and a cloud ceiling at 3 km is even though both cases were treated as equivalent in the UK analysis.

Of ultimate concern is the exposure prediction one obtains for particular cases of interest. In Figure 46 the thermal exposure as a function of ground range is shown for a 100 kt surface burst for the 95% case with the curve identification being the same as in the previous figure. All curves use the same source output as described in Section 3.1 and the only difference is the transmission factors. The Cooke transmission factor leads to an underprediction of the exposure for exposure levels less than about 30 cal/cm^2. The presence of clouds at 3 km results in an increase in the exposure for levels less than about 9 cal/cm^2.

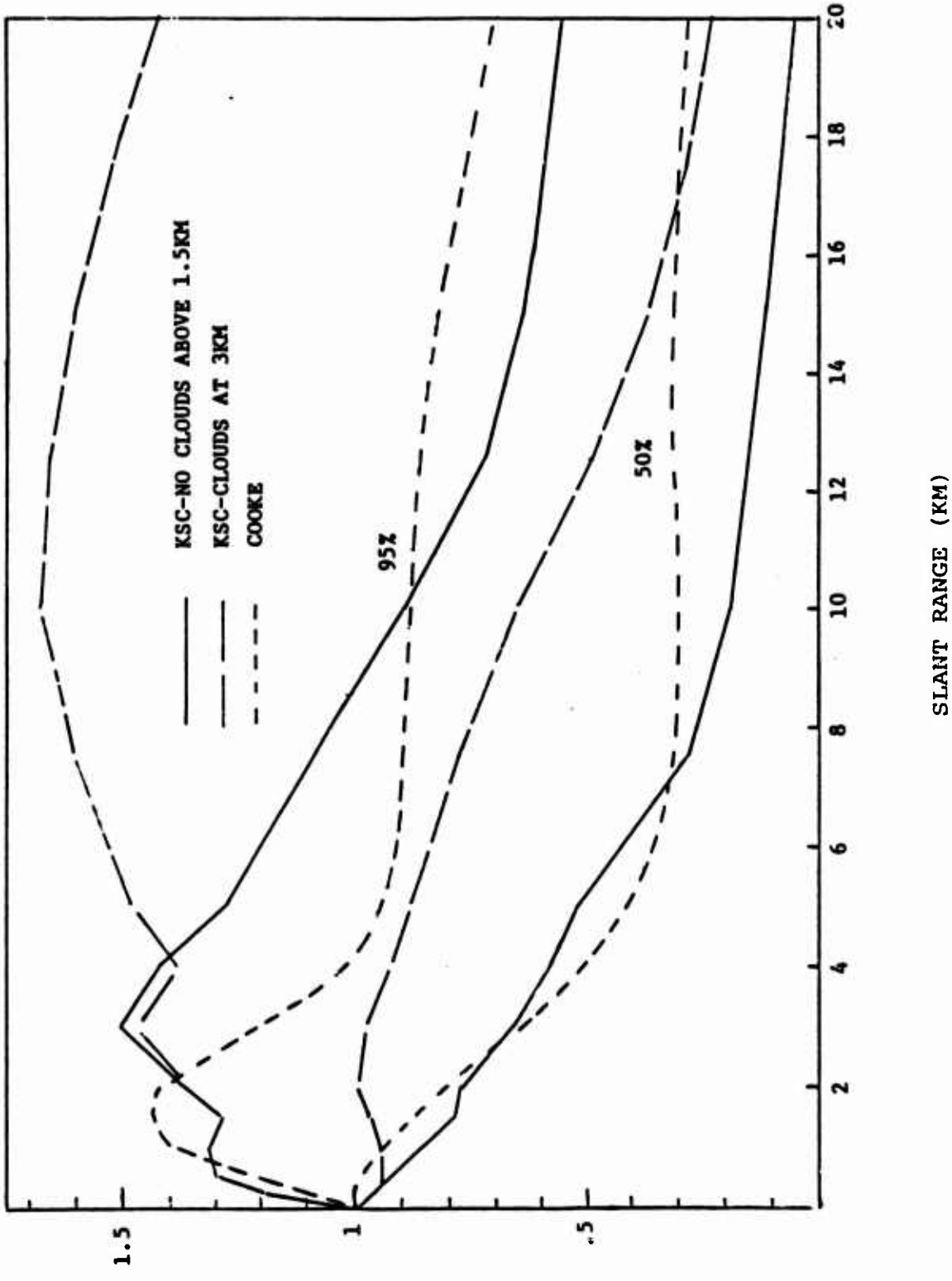

Figure 45. Comparison of KSC and UK Transmission Factors.

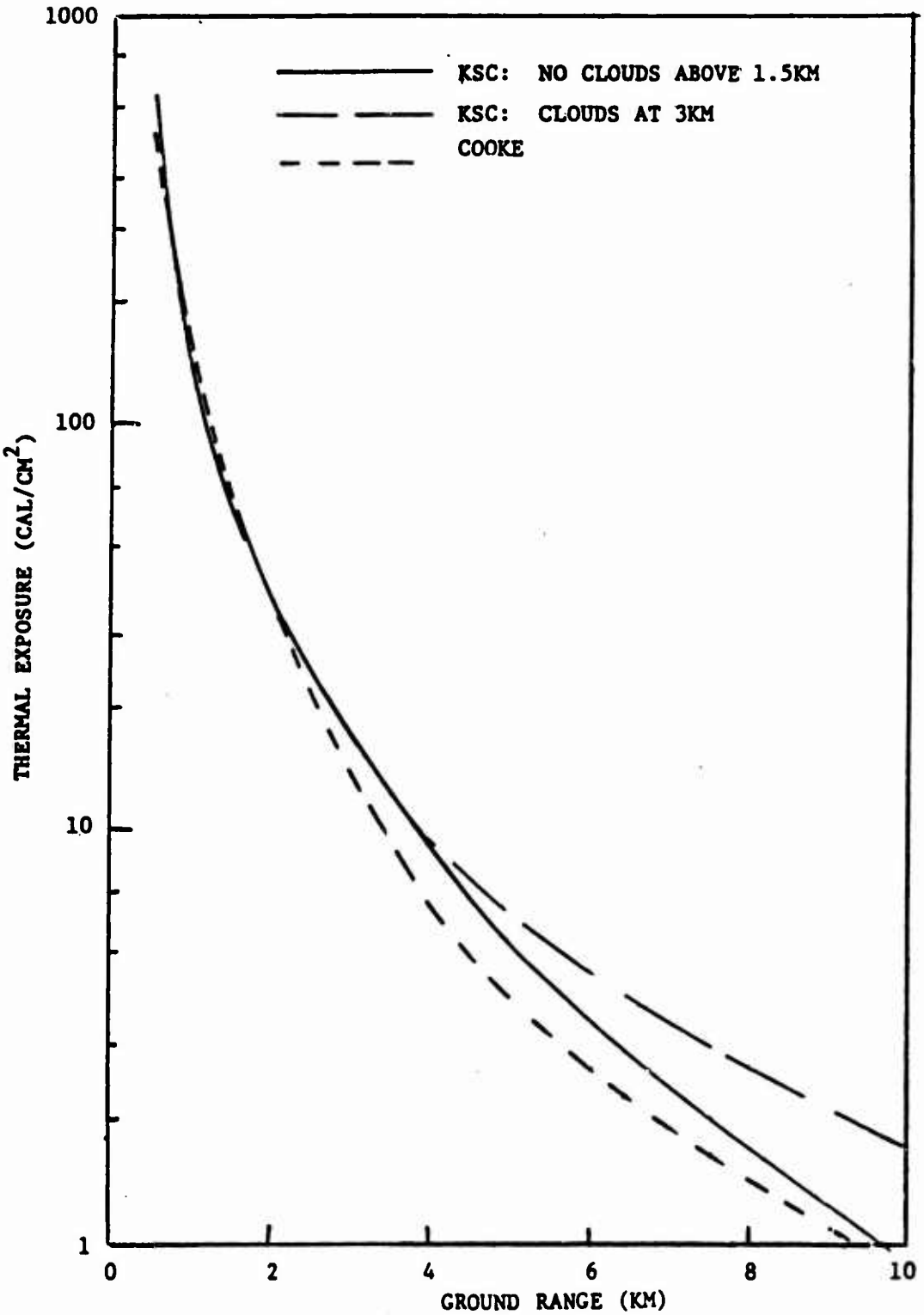

Figure 46. Comparison of KSC and Cooke Results 100 KT Surface Burst: 95% Case.

In Figure 47 the exposures for the 50% case are shown. The Cooke curve under predicts the exposure for levels less than 8 cal/cm^2. The 3 km cloud ceiling predicts higher exposures for all levels less than 60 cal/cm^2.

The same exposure predictions are shown for a 1 Mt surface burst in Figures 48 and 49. The differences are emphasized relative to the 100 kt case and begin to show up at higher exposures. These comparisons indicate that the Cooke curves should not be used for the USANCA applications. The KSC curves are uncertain because of data base uncertainties. As indicated previously, the major uncertainties occur at small visibilities. The results at higher visibilities corresponding to larger probabilities will not have large uncertainties. In the next section, the QRT data base is described, required extensions are discussed and sample results are shown.

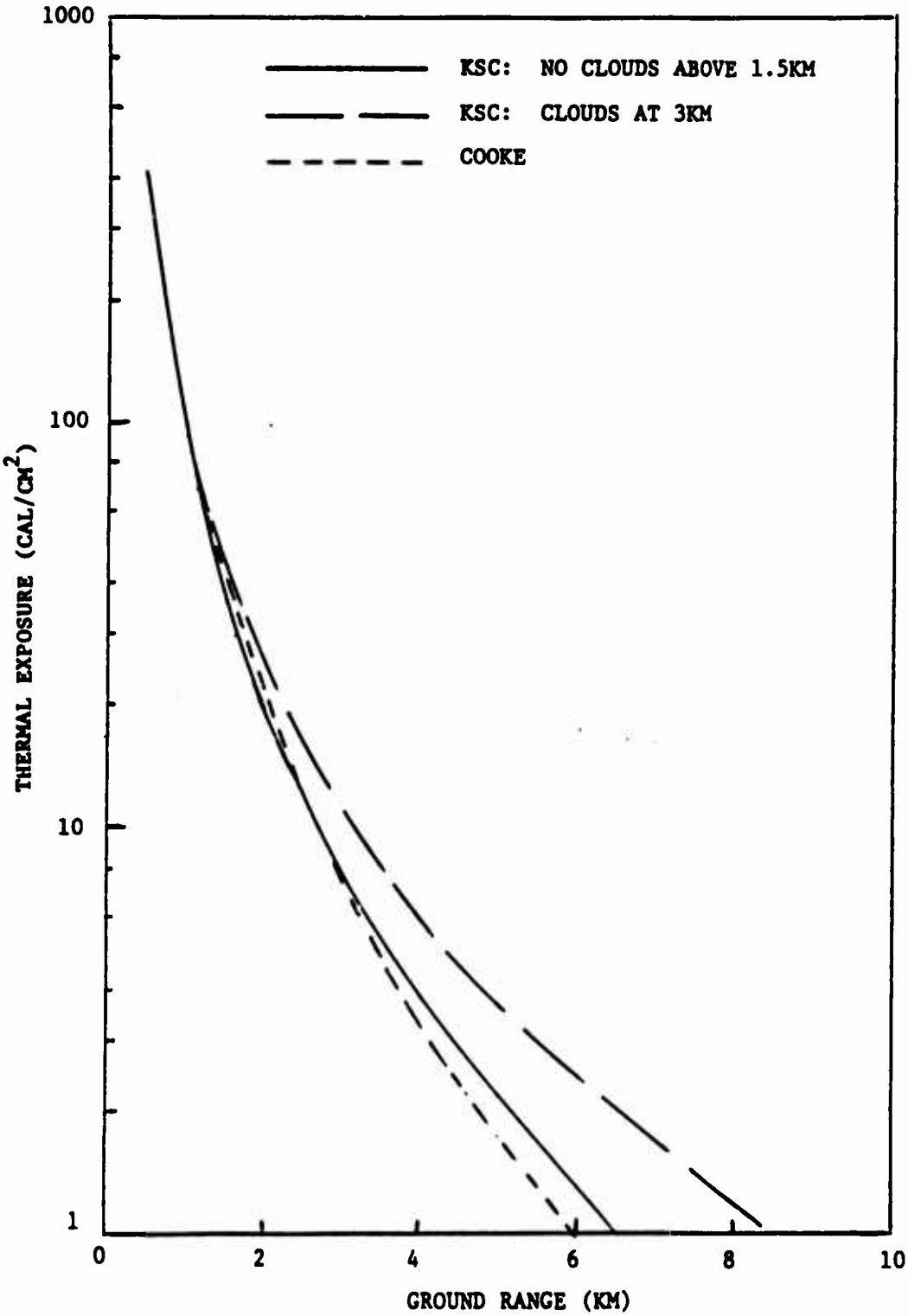

Figure 47. Comparison of KSC and Cooke Results 100 KT Surface Burst: 50% Case.

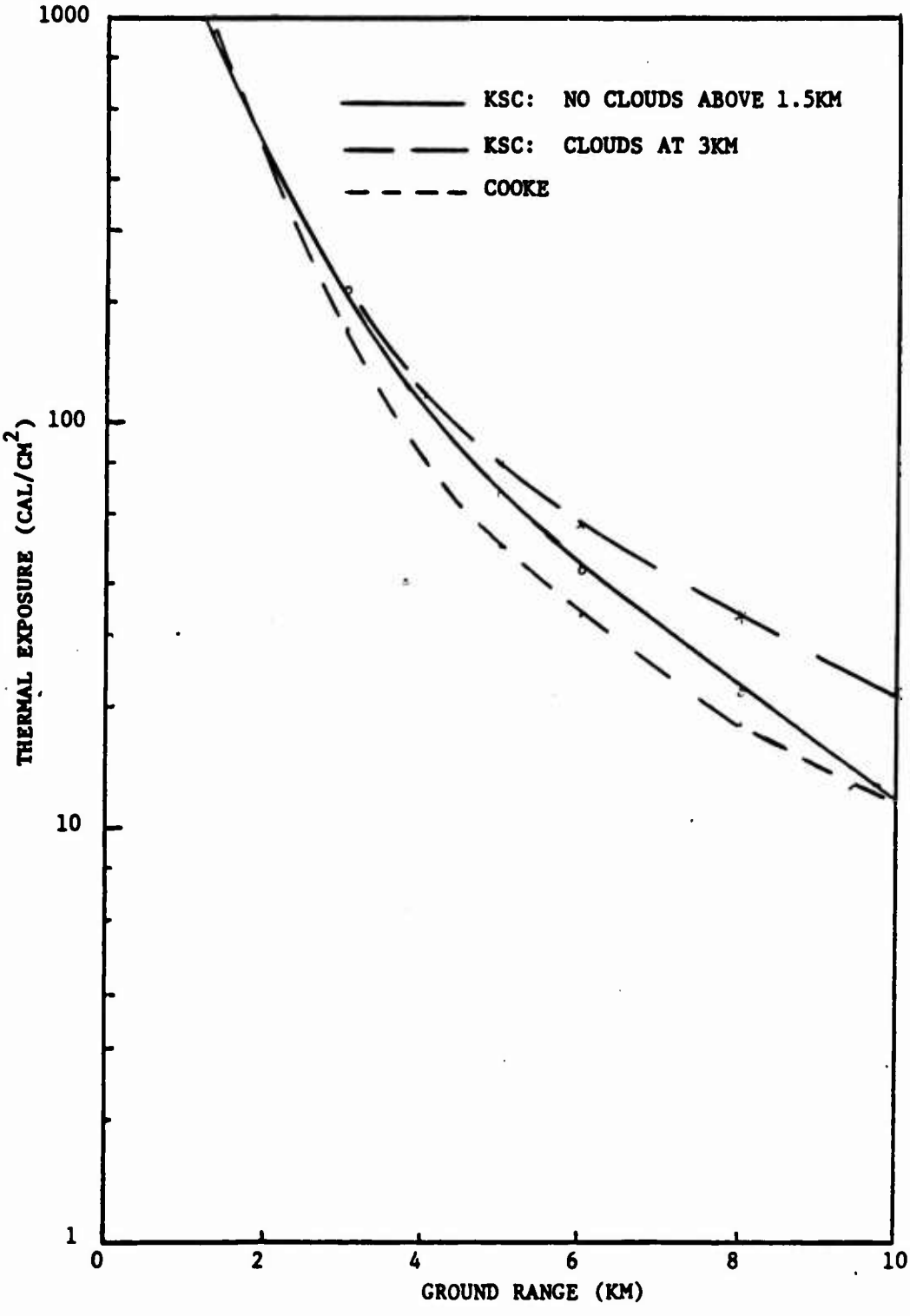

Figure 48. Comparison of KSC and COOKE Results 1 MT Surface Burst: 95% Case.

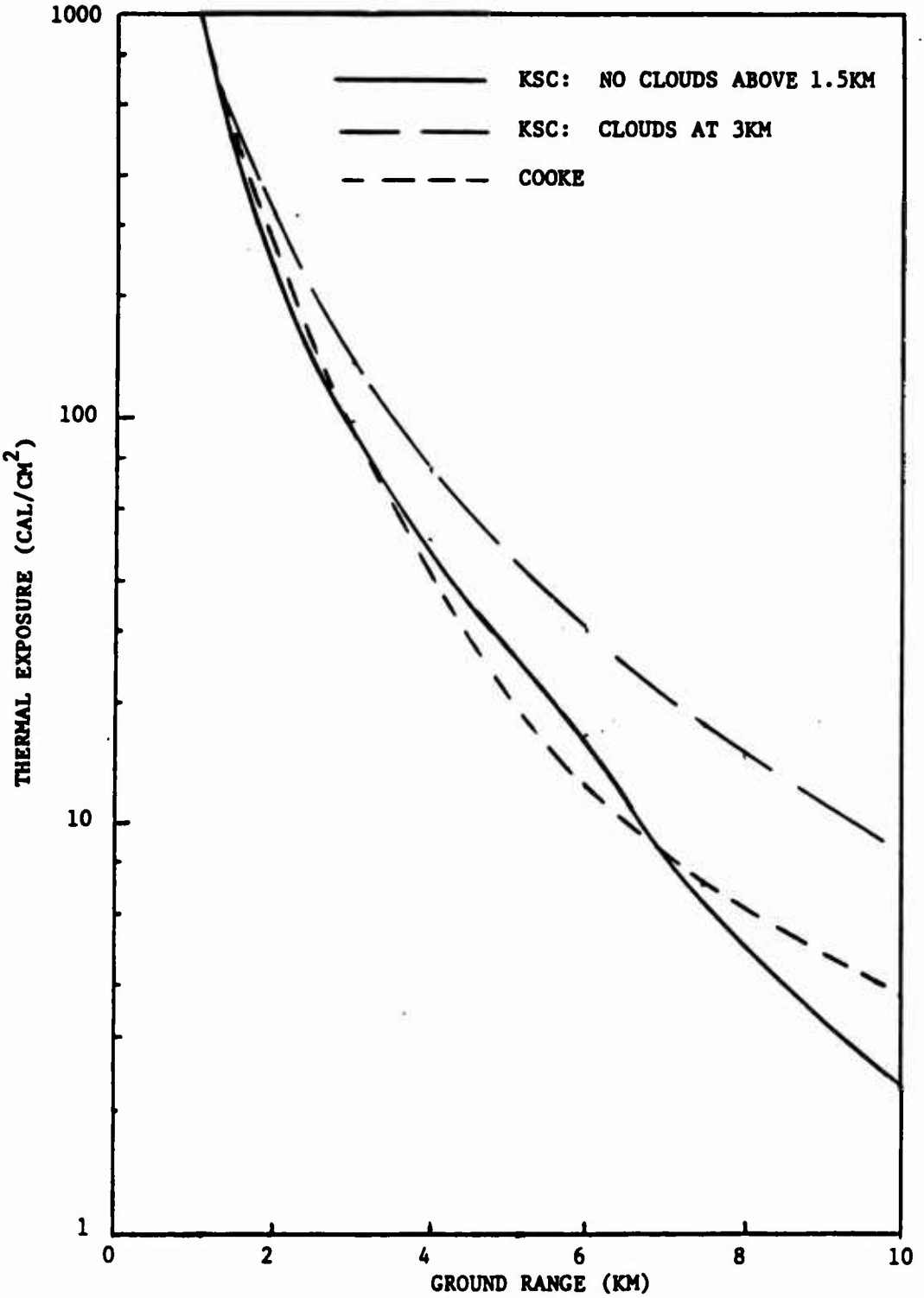

Figure 49. Comparison of KSC and COOKE Results 1 MT Surface Burst: 50% Case.

SECTION 5

MONTE CARLO DATA BASE DEVELOPMENT

As discussed the QRT data base was generated using recent model atmospheres although only one aerosol distribution (rural) was actually used in defining aerosal scattering phase functions. The data base was generated with a fairly limited set of meteorological parameters and other limitations which restrict the usefulness without considerable modification and extension. In this section, the data base is described, and the limitations are identified.

5.1 QRT DATA BASE AND PREDICTIVE APPROACH.

In Table 20, the major parameters of the QRT data base are identified. The data base basically contains 3 groups of data. Data sets 1, 2, and 3 contain data for the 3 indicated meteorological ranges for two different ground albedos and no clouds. Data sets 4 and 5 contain data for the same geometry except the ground altitude is at 1.524 km (5 kft). Data sets 6 and 7 contain data for two different cloud ceiling altitudes as a function of a ground albedo. All the data are raw unsmoothed Monte Carlo data representing the scattered flux received on a flat plate detector oriented at 119 ((15-2)* 9 + 2) different possible directions. Only six different wavelengths were used which, as noted previously (and detailed in the following subsection), can not adequately represent the nuclear thermal spectrum.

The QRT approach consists of calculating the direct flux at six wavelengths including scattering and narrow bank IR absorption effects. The scattered flux is determined by interpolating in the massive Monte Carlo data base which stores the scattered flux per unit source versus source altitude, receiver altitude

Table 20. QRT Data Base.

DATA SET NO.	GROUND ELEVATION (KM)	MET. RANGE (KM)	CLOUD BASE (KM)	GROUND ALBEDO
1	0	23	--	0, .8
2	0	10	--	0, .8
3	0	2	--	0, .8
4	1.524	23	--	0, .8
5	1.524	10	--	0, .8
6	0	23	1.53	0, .2, .4, .6, .8
7	0	23	3.65	0, .2, .4, .6, .8

SOURCE ALTITUDES: .01, 2, 5, 20, 80 (KFT)
RECEIVER ALTITUDES: .001, 1, 2, 5, 10, 20, 30 (KM)
RECEIVER RANGES: .82, 4.92, 16.4, 32.8, 49.2, 65.6, 82, 98.4, 114.8, 131.2(KM)
SAMPLING SURFACE ORIENTATION: 15 Polar and 9 Azimuthal Directions
SOURCE WAVELENGTHS: .337, .55, .94, 1.06, 1.25, 1.7
STORED DATA: Scattered Monte Carlo Fluence Received on Flat Plate Detector (1/2 angle field of view of 90°)

and range, azimuth and polar angles, ground albedo, and ground level meteorological range. The fluxes are curve fit at up to 20 wavelength intervals. The receiver exposure is then calculated by integrating the direct and scattered contributions over the fireball spectral output.

The direct flux from a point source is represented by

$$T_D(\lambda_i) = \frac{\cos\theta_z}{4\pi x^2} e^{-\tau/\cos\theta_o} * F_A(\lambda, x) \qquad (46)$$

where:

x	=	source to receiver distance
θ_z	=	angle between the source to receiver vector and the receiver surface normal
θ_o	=	angle between the source to receiver vector and the ground surface normal
τ	=	atmospheric scattering optical thickness between the source and receiver planes
$F_A(\lambda,x)$	=	gaseous attenuation factor for wavelength and source-receiver distance x.

If the source and receiver are at the same altitude then the exponential argument is replaced by -sx where s is the atmospheric scattering extinction coefficient at the source altitude.

As described in the QRT manual, the gaseous attenuation factor accounts for the attenuation by atmospheric gases in the infrared wavelength region. Gases included in the modeling

include H_2O, CO_2, CH_4, and O_2 for the wavelengths chosen in the data base. The transmission along a path is given by

$$F_A = \exp\left\{ -\sum_j \frac{(AH(j, h_1) - AH(j, h_2))/|\cos\theta|}{200\sqrt{1 + \frac{(AH(j, h_1) - AH(j,h_2))^2/|\cos\theta|}{(BH(j, h_1) - BH(j, h_2))}}} \right. \quad (47)$$

where h_1 and h_2 are the source and receiver altitudes respectively, θ_o is defined above, and the summation is over the contributing absorbing species for the various wavelengths (H_2O for .94 μm, H_2O, CO_2, and O_2 for 1.25 μm and H_2O, CO_2, and CH_4 for 1.7 μm). FA = 1 for wavelengths of .337, .55 and 1.06 μm. The AH and BH arrays are defined by

$$AH(j, h) = \int_h^\infty A(j, h) * m(j, h)dh \quad (48)$$

and

$$BH(j, h) = \frac{4}{1013} * \int_h^\infty B^2(j, h) * m(h, h) * p(h)dh, \quad (49)$$

where m is the absorber density and p is the atmospheric pressure. A and B are parameters defined in the Goody model and are given by

$$A = \sum S(i) \text{ and } B = \sum\sqrt{S(i)\ \alpha(i)} \quad (50)$$

where S(i) is the line strength and $\alpha(i)$ is the line width and the summation is over the lines in the relevant wavelength interval.

This approach is based upon a wavelength interval of 200 wavenumbers which is the basis interval used in the AFGL absorption data base. The actual width of the IR intervals is considerably larger than 200 (as will be discussed later) which can lead to inaccuracies in the transmission predictions in the IR region.

Note that O_3 was not included as an absorbing species in the IR and apparently was not included in the UV and visible portion of the spectrum. O_3 can be important in that portion of the spectrum and can be easily included in the σ and τ variables in the exponential argument in the direct flux expression.

The scattered flux contributions are calculated by interpolating in the massive data base. The data represent the energy incident upon a small plane receiver which is oriented in particular directions at a particular location in space. Data are included for specified source altitudes and for certain meteorological ranges and albedo surface conditions for the six defined wavelengths. The data are the results of a large number of Monte Carlo runs for the particular conditions of interest in which angular sampling was performed to define the scattered intensity as a function of angle. The scattered intensity was then converted to the more useful results stored in the data base.

The data base parameters were summarized in Table 20. Seven different data sets are available for the particular albedo surface combinations and meteorological ranges shown. For each data set (1 to 5) two basic scattered flux arrays corresponding to zero ground albedo, and the additional scattered flux for an albedo of .8 are stored for all possible combinations of the other parameters listed. Each data set contains 30 different data groups containing the results of each of the six wavelengths run at the five different source altitudes. For each group scattered data are stored for 70 different receiver locations corresponding to the seven receiver altitudes and the ten receiver ranges. At each location the scattered flux is stored as a function of thirteen polar and nine azimuthal directions with the nadir and zenith polar directions being stored separately since the azimuthal directions are degenerate for those directions. As mentioned arrays are defined for zero and

non-zero albedo surfaces. The scattered flux for a unique combination of these different parameters is found by a complicated search and interpolation scheme for each of the wavelengths. If the particular receiver altitude and range do not correspond to the values in the table, values for the exposure are computed for each of the four locations braketing the location of interest and interpolation is then used to define the exposure for the location of interest. Interpolation using the cosines of the polar and azimuthal angles is performed to determine the scattered flux values.

As discussed previously arrays are stored representing the value of the scattered flux for an albedo value of zero and the difference resulting from an albedo of 0.8. An approximate procedure is then given to compute the scattered flux for any arbitrary albedo.

Using the methods described above, values of the direct and scattered flux are computed for each of the six wavelengths. The albedo correction is done separately for each wavelength. The direct flux and the scattered flux are then fit separately as a function of wavelength. As indicated in Figure 50, the 0.337 μm, 0.55 μm and the 1.06 μm results are fit to evaluate fluxes for wavelengths less than 1.06 with the exception of the region from .926 to .978 where the .94 results are treated separately. The narrow bands between 1.1 and 1.15 μm and 1.35 and 1.5 μm represent strong absorption bands and the energy in these regions are set to zero. The 1.25 and 1.7 μm results are used throughout their respective bands as shown. This curve illustrates one of the penalties of using the scattered flux approach. In the IR region the scattered flux as well as the direct flux shows a wide and non-predictable dependence upon wavelength because of the complicated IR absorption characteristics. The curve fitting procedure cannot be used consistently

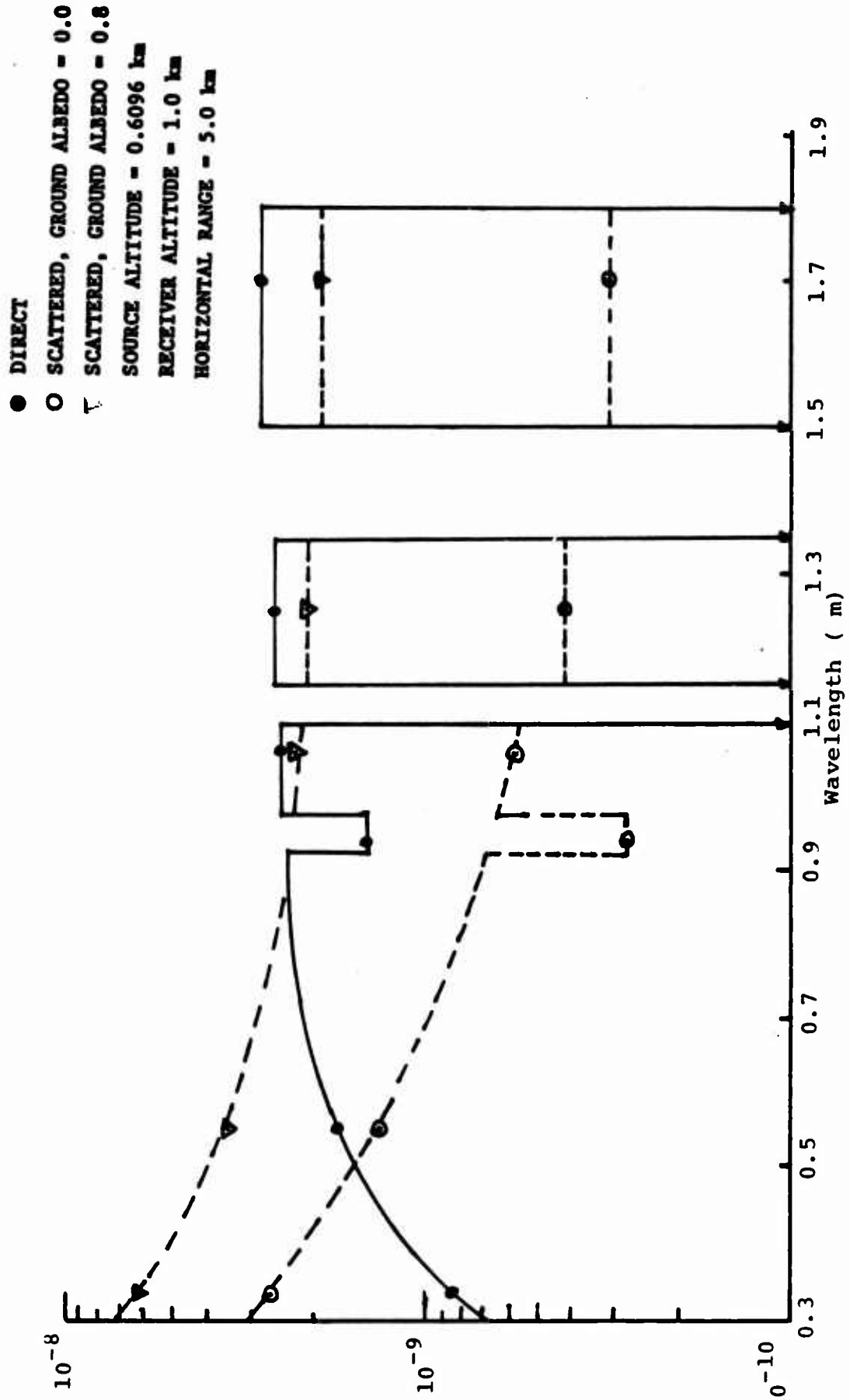

Figure 50. Direct and Integrated Scattered Intensity versus Wavelength (Ground Level Elevation = 0.0, Ground Meteorological Range = 23 km).

across the entire wavelength region and the arbitrary approach described above must be used. The buildup approach described previously which has been used in all of the KSC thermal transport calculations is a much more reasonable and consistent approach and can be used with confidence over the entire wavelength region.

Given the curve fits as described above, the fluxes are evaluated at up to 20 wavelengths and folded in with a time dependent spectral source output. Integration over wavelength then gives the irradiance at the receiver and integration over time gives the exposure.

A very large data base is thus available in the QRT code but it has been found that significant limitations in the predictive approach and data base exist and that significant modifications are required.

5.2 LIMITATIONS IN THE QRT CALCULATIONAL APPROACH AND DATA BASE.

5.2.1 Inadequate Wavelength Base.

As discussed in Section 5.1, there should be additional wavelengths in the IR region to represent properly the nuclear weapon thermal output spectrum adequately in this region. Adding these wavelengths and converting to the buildup factor approach to calculate the scattered flux would provide the best approach to solve this problem.

5.2.2 Utilization of Scattered Flux Data.

As discussed previously, the scattered flux magnitude varies very rapidly with wavelength in the IR region because of the very complicated molecular absorption band structure of the absorbing gases. In absorbing regions, the scattered flux will be very small relative to that in the windows adjacent to the absorbing

bands. Trying to fit the scattered flux as a function of wavelength is possible only in the UV and visible portion of the wavelength region as was shown in the previous section. In the IR region, it was found necessary to use band averaged values. To represent accurately the wavelength dependence of the scattered flux would require many more source wavelengths than currently used. This problem is solved by using buildup factors as described in subsection 3.2.

5.2.3 Utilization of Unsmoothed Monte Carlo Data.

The scattered flux data stored on the tapes are basically unsmoothed Monte Carlo data that have been integrated over sampling angles to represent the flux on flat plate receivers with a particular orientation at a particular location in space. Monte Carlo data always have statistical uncertainties which makes their usage suspect without using smoothing or curve fitting techniques. Large variations can occur in the scattered data as a function of receiver range and altitude and orientation angle. These variations can lead to inconsistent trends of the exposure versus range. Interpolation in the very large data base is extremely time consuming. Curve fitting and smoothing the buildup factors is a much more efficient and safe approach.

5.2.4 Narrow Band IR Absorption Parameters.

IR absorption parameters averaged over a band width of 200 wavenumbers were used in the model. In Table 21, the width of the bands as discussed in QRT supporting documentation is shown. The .337 and the .55 wavelengths are not treated as bands in the modeling. All of the bands are seen to be much wider than the 200 wavenumbers used to define the basic absorption parameters. Significant errors exist in representing the wide band absorptions by narrow bands at the band center.

Table 21. QRT Band Structure.

Band Wavelength (μm)	Band Limits (μm)	Band Width (wavenumber)
.337	N/A	N/A
.55	N/A	N/A
.94	.926 - .978	574
1.06	.978 - 1.10	1134
1.25	1.15 - 1.35	1288
1.70	1.50 - 1.80	1111

SECTION 6

RECOMMENDED APPROACH FOR QRT DATA BASE REVISIONS

In this section the recommended approaches for using the QRT code data base are discussed. The KSC wavelength band structure has been found to represent the output spectrum and if the buildup factor approach is used will give a very good description of the atmospheric transport properties. This basic wavelength band structure will be used with revised IR absorption techniques to calculate the direct flux as described in detail in Section 3.4.

The irradiance as a function of time will be given by the expression

$$H = \frac{g}{4\pi R^2} \sum_{\lambda} T_D(\lambda, h_s, h_r, R) * B_s(\lambda, h_s, h_r, \rho, \phi) * B_a(\lambda, h, h, R, \phi) * P(\lambda, \tau, \cos\theta) \quad (51)$$

where

T_D	=	the direct flux transmission discussed previously
B_s	=	buildup factor with zero albedo
B_a	=	buildup enhancement factor due to albedo surfaces
P	=	power output of the fireball
λ	=	wavelength
h_s, h_r	=	source and receiver altitudes
g	=	geometry factor
R	=	slant range
ρ	=	optical depth along slant path
t	=	time after burst
θ	=	polar angle to slant path
ϕ	=	orientation of sampling surface

The source altitude at zero time is the height of burst and thereafter is the fireball altitude which increases as a function of time. The receiver altitude and the slant range can also be a function of time for a moving target.

The B_s (λ , h_s, h_r, R, ρ , ϕ) represents the buildup factor evaluated for all of the listed parameters. These will be stored as curve fits in as many parameters as possible in order to reduce the running time and interpolation procedures will be used in the other parameters. The B_a (λ , h_s, h_r, R, ϕ) represent the buildup enhancement factors due to the albedo surfaces and again will be curve fit in as many parameters as possible. The P (λ , t, cos θ) represents the power output of the fireball and will be obtained from the revised RECIPE code described in Section 3.1. The exposure is then found by integrating the irradiance over time.

6.1 EXTENSION OF THE WAVELENGTH DATA BASE.

As discussed in Section 3.1 the current six wavelengths do not extend to high enough wavelengths to represent adequately the nuclear weapons termal output spectrum. In order to calculate the buildup factors for the entire range of wavelengths in the KSC wavelength band structure needed in the expression given above it will be necessary to generate scattered flux data at longer wavelengths than currently are in the QRT data base. In order to make maximum usage of the current data base it is suggested that two additional wavelengths be defined at 2.7 and 3.8 μm. Because of the predictable variation of the buildup, factors with wavelengths as shown in the previous section, it will be possible to represent accurately the multiple scattering buildup with the resulting eight wavelengths. Additional Monte Carlo runs will be made for those two wavelengths with the same general geometrical parameters as the current QRT data base for the .01, 5.0 and 80 kft source altitudes. If consistent predict-

able trends are noted, it may not be necessary to make runs at all of the possible combinations.

6.2 CONVERT SCATTERED FLUX DATA BASE TO BUILDUP FACTORS.

The buildup factors will be generated from the current data base by dividing the scattered flux arrays (SINT, SIT, and SIB) at each of the receiver locations by the proper element of the direct flux array RES. For each of the receiver locations the scattering optical depth can be calculated by the following equation

$$SOD = \frac{|\tau(h_s) - \tau(h_r)|}{|h_s - h_r|} * R \qquad (52)$$

where τ = the integral of the optical depth to the altitude of interest

h_s, h_r = source and receiver altitudes

and R = the slant range.

Example plots of the buildup factor for a wavelength of .55 μm, a source altitude of .01 kft, and a meteorological range of 23 km obtained from data set 1 are shown in Figure 51. The results are shown for receiver altitudes of .001, 1.0, 2.0, and 5.0 km. These factors were derived for a receiver orientation facing the source by interpolation in the angular information in the data base. Note that the buildup factors for the various altitudes do not differ by a large amount when plotted as a function of the optical depth. The points plotted were calculated from the ten sampling ranges used in the data base. For the lower altitudes, a larger optical depth is traversed along the slant path. The maximum optical depth plotted is seen to decrease as the altitude is increased. If the horizontal range were used as the independent variable the curves would be separate and distinct. Likewise if the scattered flux were treated as the primary

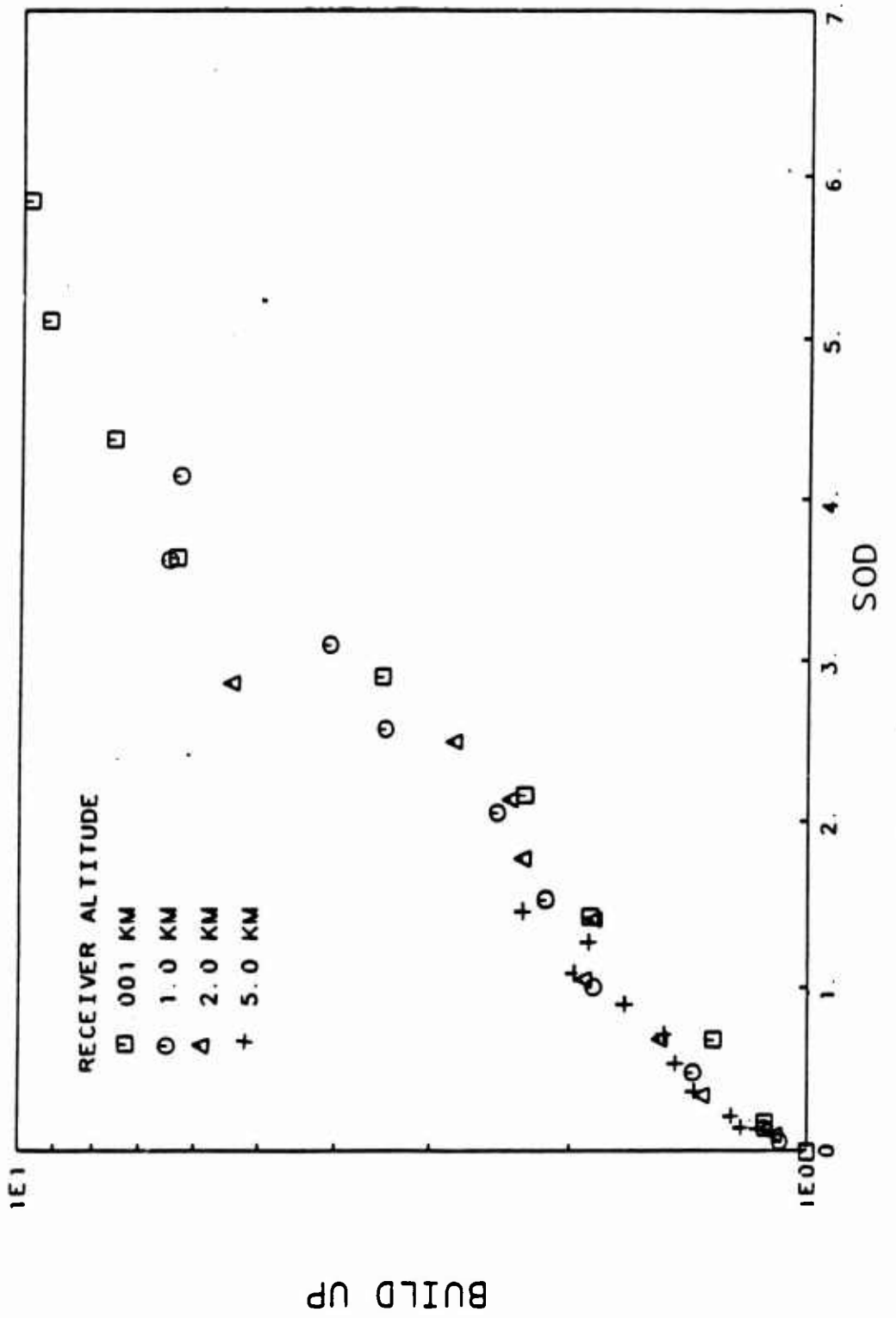

Figure 51. Plot of Buildup Factor with Source Altitude .01 KFT.

dependent variable separate curves would be obtained since the flux would be reduced much more for the lower altitudes than for the higher ones.

Similar results are plotted in Figure 52 for the 2 kft source altitude. Again note that the curves for the various sampling altitudes lie close to the same line. Comparing the two figures one notes also that the results for the two different source altitudes are very close together when plotted in this manner. This indicates that representing the results in this manner is a natural approach as one expects from elementary transport theory.

A similar procedure would be used in deriving the enhancement factors from the albedo surfaces using the TINT, RIT, and RIB arrays. Previous studies at KSC using the TRAX results have indicated that in this case the more natural procedure is to present the results as the buildup enhancement as a function of the distance from one of the albedo surfaces and the horizontal range with the unit of distance being the distance between the surfaces. This indicates that the effect is more nearly dependent upon the geometry of the problem and not on the optical depths involved.

6.3 SMOOTHING AND CURVE FITTING BUILDUP FACTORS.

All Monte Carlo results are statistically uncertain with the variance upon the penetration depths involved in the problem, the efficiency of variance reduction techniques used in the code, and the number of histories used in generating the results which directly impacts the running times of the problems. In practice one is always dealing with significant statistical uncertainties which if not handled carefully can lead to inconsistent results. For instance, observe the pluses plotted in Figure 52 representing a receiver altitude of 5 km. An increase in the buildup is noted as the SOD is increased as is expected from transport

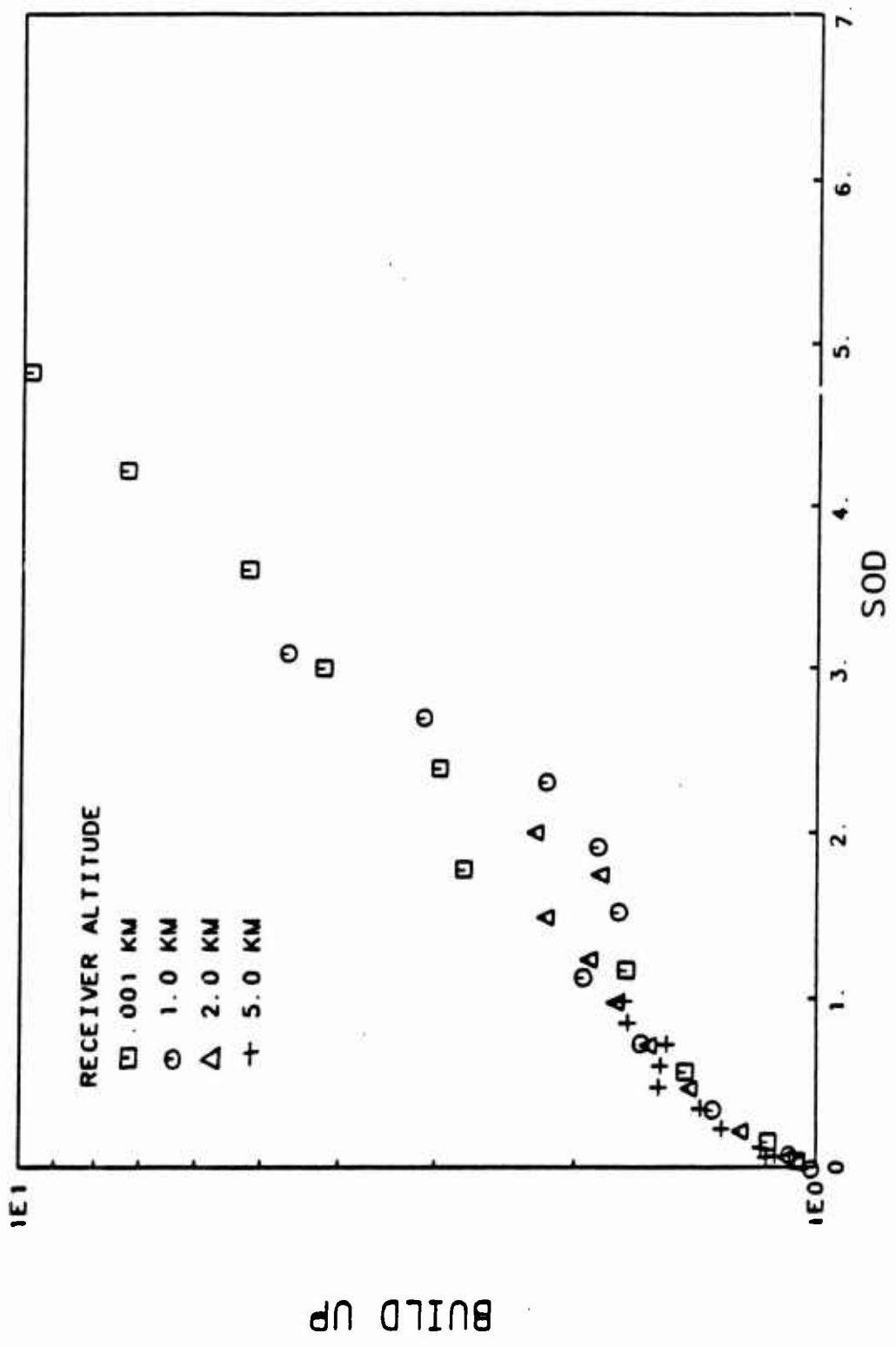

Figure 52. Plot of Buildup Factors with Source Altitude 2KFT.

theory. However, at about .5 the reverse trend is noted for three points, then the remaining two points increase with increase in SOD. This trend is not real but merely indicates the uncertainty in the results. If the raw Monte Carlo results were used with interpolation then a fallacious dependence of the flux versus range would be obtained. Likewise the circles show a strange unnatural behavior greater than 1.5. In order to obtain consistent results a cross plotting and smoothing procedure should be used.

Even if the data are smoothed and reduced to a common mesh table lookup and interpolation techniques are time consuming. A better approach is to curve fit the data in as many parameters as possible. This procedure smoothed results and is much faster than the other approach. As discussed in Section 3.4, curve fits have been developed which are capable of fitting buildup factors as a function of the various parameters and will be used in the future.

6.4 BROAD BAND IR ABSORPTION.

Narrow band absorption expressions should not be used to represent broad band transport calculations as is currently done in QRT according to the supporting documentation without a thorough investigation of the influence of the band width which has not been done. The expressions used in TRAX were derived from experiments in the laboratory and in the atmosphere. The narrow band 200nm AFGL expressions discussed earlier have been integrated over the broad bands and compared with the current TRAX expressions. No large discrepancies were noted; however, in order to make the predictive codes consistent with AFGL codes, such as low TRAX, the integrated AFGL results should be used.

SECTION 7

LIST OF REFERENCES

1. AFCRL-68-0256, Empirical Determination of Scattered Light Transport Through the Lower Atmosphere, George F. Riley, Air Force Cambridge Research Laboratory, May 1968.

2. Thermal Transmissivities in North-West Europe, Ministry of Defence, Unpublished.

3. Proceedings of the Meeting of Panel M2. Thermal Effects Symposium, 25-29 March 1968. Collected Papers, Vol. 1.

4. "Distribution of Irradiance in Haze and Fog," Eldridge and Johnson, Journal of the Optical Society of America, Volume 52, #7, p. 787 (1962).

5. Atmospheric Scattering in an Arctic Environment, Cantor and Petriev, Technical Report ECOM-2453, USAEL, 1964.

6. Atmospheric Scattering Properties of a Nevada Desert Atmosphere, Gibbons, et al., Journal of the Optical Society of America, Volume 51, 633 (1961).

7. Transmission and Scattering Properties of a Nevada Desert Atmosphere Under Cloudy Conditions, Gibbons, et al., Journal of the Optical Society of America, Volume 52, 38 (1962).

8. Unpublished Data, W.F. Lane, Chemical Defence Experimental Establishment, Porton Wetshire, England, 1965.

9. "The RECIPE Model," SAI, unpublished.

10. "The RECIPE Surface Burst Model," SAI, unpublished.

11. "Capabilities of Nuclear Weapons," DNA, unpublished.

12. "Nuclear Weapons Thermal Radiation Phenomena," KSC, unpublished.

13. TRAP

14. Blattner, W.G.M, and Warkentin, J.K., "Atmospheric Transmittance Data Base for Thermal Radiation From Point Sources," RRA-T8102, 1 March 1981.

15. Howard, J.N., Burch, D.L., and Williams, D., "Near-Infrared Transmission Through Synthetic Atmospheres," Geophysical Research Papers No. 40, Air Force Cambridge Research Center, November 1955.

16. Yates, H.W., and Taylor, J.H., "Infrared Transmission of the Atmosphere," Naval Research Laboratory Report No. 5453, 8 June 1960.

17. "U.S. Standard Atmosphere Supplements, 1966," Supplement of Documents, Washington, D.C., 1966.

18. Vigrous, E., "Contributions A l'etude Experimentale de l'absorption de l'ozone," Ann. Phys. (Paris) 8:709.

DISTRIBUTION LIST

DEPARTMENT OF DEFENSE

ASST TO THE SECY OF DEF ATOMIC ENERGY
ATTN: EXECUTIVE ASSISTANT

DEF RSCH & ENGRG
ATTN: STRAT & SPACE SYS(OS)
ATTN: STRAT & THEATER NUC

DEFENSE INTELLIGENCE AGENCY
ATTN: DB-4D
ATTN: DT-2
ATTN: RTS-2B

DEFENSE NUCLEAR AGENCY
2 CYS ATTN: SPAS
ATTN: SPSS
ATTN: SPTD
ATTN: STSP
4 CYS ATTN: STTI-CA

DEFENSE TECHNICAL INFORMATION CENTER
12 CYS ATTN: DD

FIELD COMMAND DEFENSE NUCLEAR AGENCY
ATTN: FCTT W SUMMA
ATTN: FCTXE

FIELD COMMAND DNA DET 2
LAWRENCE LIVERMORE NATIONAL LAB
ATTN: FC-1

JOINT CHIEFS OF STAFF
ATTN: GD50 J-5 FOR PLNG & PROG DIV
ATTN: J-5 NUC & CHEM DIV
ATTN: JAD/SFD
ATTN: JAD/SSD

DEPARTMENT OF THE ARMY

DEP CH OF STAFF FOR OPS & PLANS
ATTN: DAMO-NCZ

HARRY DIAMOND LABORATORIES
ATTN: SLCHD-NW-P J GWALTNEY

U S ARMY BALLISTIC RESEARCH LAB
ATTN: SLCBR-SS-T TECH LIB

U S ARMY MATERIAL TECHNOLOGY LABORATORY
ATTN: DRXMR-HH J DIGNAM

U S ARMY NUCLEAR & CHEMICAL AGENCY
ATTN: LIBRARY
ATTN: MONA-NU MR LONG

U S ARMY TRADOC SYS ANALYSIS ACTVY
ATTN: ATAA-TDC R BENSON

US ARMY MISSILE COMMAND
ATTN: AMSMI-RD-DEP W THOMAS
ATTN: AMSMI-RD-UB H GREENE

DEPARTMENT OF THE NAVY

NAVAL RESEARCH LABORATORY
ATTN: CODE 2627 TECH LIB
ATTN: CODE 4650 A WILLIAMS
ATTN: CODE 4770 G COOPERSTEIN

NAVAL SEA SYSTEMS COMMAND
ATTN: SEA-0352 M KINNA

NAVAL WEAPONS EVALUATION FACILITY
ATTN: CLASSIFIED LIBRARY

OFC OF THE DEPUTY CHIEF OF NAVAL OPS
ATTN: OP 654 STRAT EVAL & ANAL BR

STRATEGIC SYSTEMS PROGRAM OFFICE (PM-1)
ATTN: SP-272

DEPARTMENT OF THE AIR FORCE

AERONAUTICAL SYSTEMS DIVISION
ATTN: ASD/ENSSS H GRIFFIS

AIR FORCE ROCKET PROPULSION LAB
ATTN: LKCS G BEALE

AIR FORCE SYSTEMS COMMAND
ATTN: SDM
ATTN: XRTO

AIR FORCE WEAPONS LABORATORY, AFSC
ATTN: HO R DUFFNER
ATTN: NTA A SHARP
ATTN: NTES
ATTN: SUL

AIR FORCE WRIGHT AERONAUTICAL LAB
ATTN: FIMG

AIR FORCE WRIGHT AERONAUTICAL LAB
ATTN: AFWAL MLBT W ANSPACH

AIR UNIVERSITY LIBRARY
ATTN: AUL-LSE

DEPARTMENT OF THE AIR FORCE (CONTINUED)

BALLISTIC MISSILE OFFICE/DAA
ATTN: ENSN
ATTN: ENSX
ATTN: MYE

DEPUTY CHIEF OF STAFF/AF-RDQI
ATTN: AF/RDQI

HEADQUARTERS U S AIR FORCE
ATTN: AFXOOTS

DEPARTMENT OF ENERGY

DEPARTMENT OF ENERGY
ATTN: OMA/DP-225

UNIVERSITY OF CALIFORNIA
LAWRENCE LIVERMORE NATIONAL LAB
ATTN: L-125 J KELLER
ATTN: L-262 J KNOX
ATTN: L-8 P CHRZANOWSKI

LOS ALAMOS NATIONAL LABORATORY
ATTN: E548 R S DINGUS
ATTN: T T SCOLMAN
ATTN: R S THURSTON
ATTN: R W SELDEN

SANDIA NATIONAL LABORATORIES
ATTN: EDUC AND TECH LIB DIV
ATTN: H NORRIS

SANDIA NATIONAL LABORATORIES
ATTN: M B COWAN
ATTN: ORG 7112 A CHABAI

OTHER GOVERNMENT

CENTRAL INTELLIGENCE AGENCY
ATTN: OSWR/NED

DEPARTMENT OF DEFENSE CONTRACTORS

ACUREX CORP
ATTN: C NARDO

AEROJET GENERAL CORP
ATTN: A COLLINS

AEROSPACE CORP
ATTN: M2-250

ANALYTIC SERVICES, INC (ANSER)
ATTN: J SELIG

APTEK, INC
ATTN: T MEAGHER

BOEING CO
ATTN: R L DYRDHAL
ATTN: A DACOSTA

BOEING MILITARY AIRPLANE CO
ATTN: D SAWDY

BOEING TECH & MGMT SVCS, INC
ATTN: E YORK

CALIFORNIA RSCH & TECHNOLOGY, INC
ATTN: K KREYENHAGEN

CALSPAN CORP
ATTN: M DUNN
ATTN: M HOLDEN

CARPENTER RESEARCH CORP
ATTN: H J CARPENTER

G B LABORATORY, INC
ATTN: G BURGHART

GENERAL ELECTRIC CO
ATTN: A GARBER
ATTN: B MAGUIRE

HERCULES, INC
ATTN: P MCALLISTER

INSTITUTE FOR DEFENSE ANALYSES
ATTN: CLASSIFIED LIBRARY

KAMAN SCIENCES CORP
2 CYS ATTN: A PORTARE
2 CYS ATTN: J KEITH

KAMAN SCIENCES CORP
ATTN: L MENTE
ATTN: R RUETENIK
ATTN: W LEE

KAMAN SCIENCES CORP
ATTN: F SHELTON
ATTN: J HOFFMAN
ATTN: J KEITH

KAMAN TEMPO
ATTN: DASIAC

KAMAN TEMPO
ATTN: DASIAC

LOCKHEED MISSILES & SPACE CO, INC
ATTN: F BORGARDT

LOCKHEED MISSILES & SPACE CO, INC
ATTN: R WALZ

DEPT OF DEFENSE CONTRACTORS (CONTINUED)

MARTIN MARIETTA DENVER AEROSPACE
ATTN: E STRAUSS

MCDONNELL DOUGLAS CORP
ATTN: L COHEN

MCDONNELL DOUGLAS CORP
ATTN: M POTTER

MORTON THIOKOL, INC
ATTN: K HESS

PACIFIC-SIERRA RESEARCH CORP
ATTN: H BRODE, CHAIRMAN SAGE

PHYSICS INTERNATIONAL CO
ATTN: J SHEA

R & D ASSOCIATES
ATTN: F A FIELD
ATTN: P RAUSCH

RAND CORP
ATTN: P DAVIS

RAND CORP
ATTN: B BENNETT

S-CUBED
ATTN: G GURTMAN
ATTN: R DUFF

SCIENCE APPLICATIONS INTL CORP
ATTN: W PLOWS
ATTN: W YENGST

SCIENCE APPLICATIONS INTL CORP
ATTN: J COCKAYNE
ATTN: W LAYSON

SCIENCE APPLICATIONS INTL CORP
ATTN: A MARTELLUCCI

SCIENCE APPLICATIONS INTL CORP
ATTN: J MANSHIP

SOUTHERN RESEARCH INSTITUTE
ATTN: C PEARS

SRI INTERNATIONAL
ATTN: D CURRAN

TECHNOLOGY DEVELOPMENT ASSOCIATES
ATTN: N DISPENSIERE

TOYON RESEARCH CORP
ATTN: B GRAGG
ATTN: J CUNNINGHAM

TRW ELECTRONICS & DEFENSE SECTOR
ATTN: A ZIMMERMAN
ATTN: D BAER
ATTN: M SEIZEW
ATTN: N LIPNER
ATTN: P BRANDT
ATTN: R BACHARACH
ATTN: R PLEBUCH
ATTN: W WOOD

TRW ELECTRONICS & DEFENSE SECTOR
ATTN: D KENNEDY
ATTN: E ALLEN
ATTN: E WONG
ATTN: L BERGER
ATTN: N GUILES
ATTN: P DAI
ATTN: V BLANKINSHIP
ATTN: W POLICH